University of Alberta

Optimal Materials for Direct Oxidizing SOFC Anode

by

Masaki Itome

A thesis submitted to the Faculty of Graduate Studies and Research in partial fulfillment of the

requirements for the degree of *Master of Science*

in

Chemical Engineering

Department of *Chemical and Materials Engineering*

Edmonton, Alberta

Fall 2004

Your file Votre référence
ISBN: 0-612-95776-4
Our file Notre référence
ISBN: 0-612-95776-4

Acknowledgements

I would like to thank my supervisor Dr. Alan Nelson for his technical and financial support of this research. I would also like to thank the Department of Chemical and Materials Engineering at University of Alberta for providing the opportunity to enroll in this project. I appreciate other staff in the same department, as well, for technical support for the equipment used in these experiments.

Table of Contents

Figures

Tables

Equations

Chapter 1

Introduction

1.1 Global Warming and Fuel Cells

Global warming, caused by excessive emission of so-called greenhouse gases, has become a serious worldwide problem. Accumulation of carbon dioxide (CO_2) in the atmosphere is the main cause of global warming [1]. Environment Canada reports that the world average temperature has risen by 0.3 to 0.6 °C in the past 100 years and the average global sea level has risen by 10 to 25 cm [1]. Further global warming will result in more severe and frequent natural disasters, such as hurricanes, droughts, and floods in all areas in the world. Table1-1 lists the expected disasters resulted from climate change [2].

In Canada, the water level in the Great Lakes is expected to decline due to the droughts. In the past, Canada has experienced a $35 million loss for shipping and hydropower. In the Prairies, the decreasing snow and rising temperature will result in drier soil and higher frequency of droughts and floods. For example in 1988, the Prairies faced a 31 % decrease in crops and a $4 billion loss [1].

Examples of climate variability and extreme climate events and their impacts.	
Projected Change	**Projected Impacts**
Higher maximum temperatures, more hot days and heat waves over nearly all land areas.	Incidence of death and serious illness in older people and urban poor
	Heat stress in livestock and wildlife
	Risk of damage to a number of crops
	Electric cooling demand
	Energy supply reliability
Higher minimum temperatures, and fewer cold days, frost days, and cold waves over nearly all land areas.	Cold-related human morbidity and mortality Risk of damage to a number of crops
	Range and activity of some pests and disease vectors
	Heating energy demand
	Flood, landslide and avalanche damage
More intense precipitation events	Soil erosion
	Flood run off could increase recharge of some flood plain aquifers
	Pressure on government and private flood insurance systems and
	disaster relief

Table 1-1. Extreme climates and their impacts. Source: The IPCC 2001. Third Assesment Report

About half of the global CO_2 emissions are from the developed nations, namely United States (24.7%), Russia (6.5%), Japan (5.0%), Germany (3.7%), UK (2.5%), Canada (2.5%), Italy (2.0%) and France (1.8%). About 90 % of the CO_2 emissions by the developed nations comes from the combustion of fossil fuels [3]. In 1997, delegates from 160 nations met in Kyoto, Japan and launched the Kyoto Protocol. In this protocol, all Annex I nations have their own targets to which they reduce their CO_2 emissions. Canada ratified this Protocol on December 17th 2002, which obligates Canada to reduce CO_2 emissions by 6% of its 1990 level between 2008 and 2012 [1, 2].

To meet the Kyoto targets, new technologies must be developed to improve the world's energy efficiency. Fuel cells, as well as solar cells, wind power and hydropower generation, are promising candidates for CO_2 reduction.

1.2 Classification of Fuel Cells

Fuel cells are typically classified in various categories depending on their materials, structures, and operating temperatures. As seen from Table 1-2, the structures, materials, and operating environment are significantly different for the various fuel cells. In this section, details about the representative types of the cells are reviewed.

	PAFC	MCFC	SOFC	PEFC (PEM)	AFC
Electrolyte	Phosphoric acid	Molten carbonate Salt	Sollid Oxide	Polymer Electrolyte	Alkaline Solution
	H_3PO_4	K_2CO_3, Na_2CO_3	YSZ	Nafion®	
Anode	Platinum	Ni-Cr/Ni-Al alloy	Nickel	Platinum	Nickel
Cathode	Platinum	Nickel oxide	Strontium-doped lanthanum manganite (LSM)	Platinum	Nickel
Anode Reaction	$H_2 \rightarrow 2H^+ + 2e^-$	*see eqn (i) below*	*see eqn (iii) below*	$H_2 \rightarrow 2H^+ + 2e^-$	$H_2 + 2OH^- \rightarrow 2H_2O + 2e^-$
Cathode Reaction	$\frac{1}{2}O_2 + 2e^- + 2H^+ \rightarrow 2H_2O$	$\frac{1}{2}O_2 + CO_2 + 2e^- \rightarrow CO_3^{2-}$	$\frac{1}{2}O_2 + 2e^- + H_2O \rightarrow 2OH^-$	$\frac{1}{2}O_2 + 2e^- + 2H^+ \rightarrow 2H_2O$	$\frac{1}{2}O_2 + 2e^- + H_2O \rightarrow 2OH^-$
Overall Reaction	$H_2 + \frac{1}{2}O_2 \rightarrow H_2O$	*see eqn (ii) below*	see eqn (iv) below	$H_2 + \frac{1}{2}O_2 \rightarrow H_2O$	$H_2 + \frac{1}{2}O_2 \rightarrow H_2O$
Operating Temperature (°C)	150-200	600-700	650-1000	70-80	80 -230
Fuels	H_2 and Natural gases, etc	H_2, CO	H_2, CO	H_2	H_2
Efficiency (HHV%)	40-45	45-55	50-60	40-50	40-70
Realised Power	50kW - 11MW	100 kW - 2MW	100 - 250 kW	5 - 250 kW	5 - 150 kW
Charge Carrier in the Electrolyte	H^+	CO_3^{2-}	O^{2-}	H^+	OH^-
Applications	Stationary			Transportation, Space, Millitary, Energy storage systems	

$H_2 + CO_3^{2-} \rightarrow H_2O + CO_2 + 2e^-$ $CO + CO_3^{2-} \rightarrow 2CO_2 + 4e^-$	eqn (i)	$H_2 + O^{2-} \rightarrow H_2O + 2e^-$ $CO + O^{2-} \rightarrow CO_2 + 2e^-$	eqn (iii)
$H_2 + \frac{1}{2}O_2 \rightarrow H_2O$ $CO + \frac{1}{2}O_2 \rightarrow CO_2$	eqn (ii)	$H_2 + \frac{1}{2}O_2 \rightarrow H_2O$ $CO + \frac{1}{2}O_2 \rightarrow CO_2$	eqn (iv)

Table 1-2. Summary of representative fuel cell types [5].

1.2.1 PAFC

The PAFC (Phosphoric Acid Fuel Cell) was the first type of cell to be introduced in the market by International Fuel Cells Corporation, currently UTC Fuel Cells [4, 5]. PAFCs deliver power over a wide range, typically 50 kW – 11 MW, and are mostly used as stationary power generators. The advantages of the PAFC are its simple construction, chemical and thermal stability, and the low volatility of the electrolyte at its operating temperature (150 – 200 °C). The disadvantages of the PAFC are its high cost of construction and poisoning of the catalyst due to CO [6]. PAFCs use platinum in the both electrodes, which also raises its cost. A platinum anode is also sensitive to CO poisoning [6, 7]; therefore, it requires very pure hydrogen as fuel. Using purer hydrogen will result in higher cost; therefore, the materials for the electrodes should be modified to be more tolerant to CO poisoning.

1.2.2 MCFC

The MCFC (Molten Carbonate Fuel Cell) is one of the high operating temperature fuel cells, operating as high as 600 °C [4, 5]. Due to its high operating temperature, it does not require high precious metal loading, and therefore is lower in cost. Not only is it less expensive because less precious metals are used, it also avoids the possibility of CO

poisoning on the electrodes. The high temperature is also beneficial when cogeneration is combined with the cell. The disadvantage of MCFC is its corrosiveness at the anode due to the high temperatures and the dissolution of NiO at the cathode [6].

1.2.3 PEM

PEM (Proton Exchange Membrane) cells are probably the most well-known type of fuel cells since they were the first to be used in space [4, 5, 8]. It was the basis for the 1 kW fuel cell stack in the Gemini program. It is also well-known for automotive use, with one example being the stacks developed by Ballard Power Systems for major automobile companies in the world, such as Daimler Chrysler, Ford Motor Co., Honda Motors, Nissan, and Hyundai. General Motors and Toyota have also developed their own PEM stacks, some of which have already been released for limited sale [9].

The key characteristic of PEM fuel cells are their low operating temperature. The low operating temperature allows the use of proton conducting polymers, typically Nafion® (Dupont). This low operating temperature also allows for fast-start up, which is necessary for automotive applications. The power densities achieved by PEM fuel cells are very high which is advantageous in the space limited conditions in automobiles. The primary disadvantage is that the fuel is limited to pure hydrogen.

1.2.4 DMFC

DMFCs (Direct Methanol Fuel Cells) enable the direct use of methanol without any reforming. The DMFC is essentially the same as the PEM fuel cell in its structure except that the DMFC anode contains ruthenium. Methanol is easier to store and transport than hydrogen; therefore, DMFCs may be the ideal cell for automotive applications. The limitation for DMFCs in automobiles is its low power output, which is less than 10 kW. Therefore, the DMFC is primarily used for electronics, such as laptop computers and cell phones [10].

1.2.5 AFC

AFCs (Alkaline Fuel Cells) are also known for their use in space missions, specifically the Apollo program. AFCs typically use potassium hydroxide (KOH) as the electrolyte [4, 5]. AFCs have the highest efficiency among all the fuel cells and are also inexpensive with respect to the anode material, which is usually nickel and does not require the use of precious metals. AFCs appear to be economical in construction; however, they cost more to operate. AFCs operate only with highly pure feed gases, in which case air is not acceptable in place of oxygen at the cathode [11].

1.2.6 SOFC

SOFCs (Solid Oxide Fuel Cells) are unique with their high operating temperatures, within the range of 650 – 1000 °C, and an oxygen conducting ceramic, typically 8 mol% yttria-stabilized-zirconia (8YSZ) as the electrolyte. This allows conduction of oxygen ions, instead of protons as in other types, through the electrolyte to the anode. Therefore, any combustible fuels can be used; the fuel is not limited to pure hydrogen [12]. Indeed, the use of H_2S has been reported [13, 14]. One disadvantage of SOFCs is the rapid deactivation caused by carbon deposition [15]. The elimination of this problem is the main focus of this research, and will be discussed in more detail in later chapters.

1.3 The Need for the Development of Direct Oxidizing SOFC

Although many companies have been striving to introduce fuel cell powered products to consumers, they have been relatively unsuccessful to date. For stationary applications, International Fuel Cells Corporation, currently UTC Fuel Cells, has been providing a commercial PAFC for over a decade [4]. In the automotive industry, Toyota, Honda, Nissan, Ballard Power Systems, and General Motors have introduced PEM-based vehicles into the market since the end of 2002 [16-20]. However, these fuel cells require reconstruction of the current fueling infrastructure to a hydrogen-based one. Hydrogen is

also very difficult to store due to its high diffusion coefficient, the primary cause of leakage, and it carries high risk of handling due to its high flammability [21]. In addition to these disadvantages, CO_2 emissions are still generated during traditional hydrogen production; therefore, the fuel cell is not "zero emission". Because the fuel cells are not "zero emission", energy efficiency needs to be considered. Poorly designed fuel cells can actually have lower efficiency than internal combustion engines [22, 23]. Indeed, overall efficiency (well-to-wheel efficiency) of hydrogen fuel cell vehicles, even with the hybrid system, is about the same as the gasoline powered hybrid vehicles that are currently available to consumers worldwide [24]. Therefore, overall energy efficiency could be even worse by the introduction of hydrogen powered fuel cells, and only offer an advantage if the hydrogen is produced without CO_2 emissions.

A vast amount of energy is lost during the hydrogen production and transportation steps [22]. Figure 1-1 indicates that transporting crude oil or even refined hydrocarbons have less energy loss than producing and transporting hydrogen. Therefore, the development of fuel cells that operate by the direct consumption of hydrocarbons significantly improves the overall efficiency and eliminates the need for developing a hydrogen transportation and fueling infrastructure. This also avoids the handling risks associated with hydrogen.

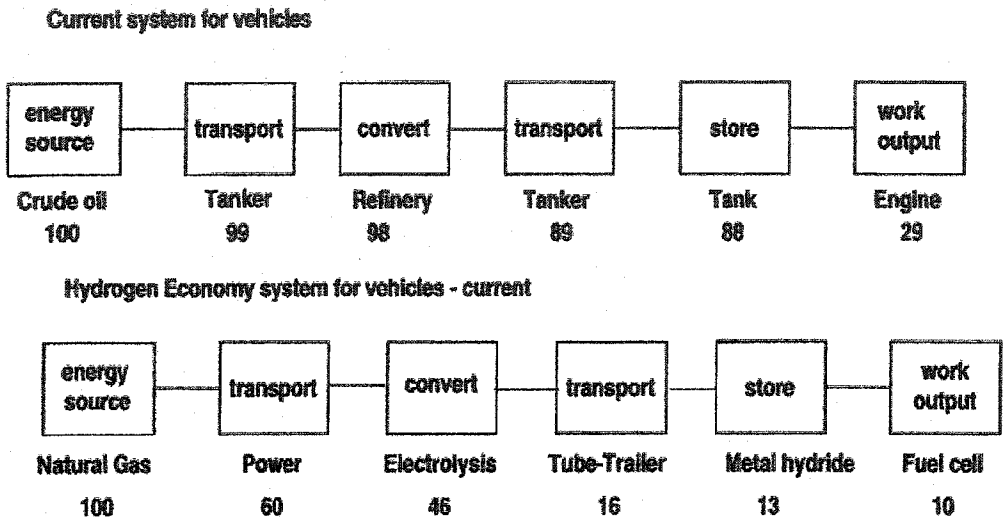

Figure 1-1. Drain of energy [22].

In contrast with PEM or other types of fuel cells, SOFCs do not limit the fuel to hydrogen [4]. Therefore, SOFCs are able to directly operate with any combustible fuel. Because of its ability for direct operation with hydrocarbons, the SOFC is regarded as the most promising candidate to improve the world's energy efficiency, and thus may be the most effective method for preventing global warming.

1.4 Research Objectives

The primary objectives of this research are to investigate the properties of nickel, copper, cobalt, and silver based catalysts for the direct oxidation of hydrocarbons, and determine which catalyst is the best for the direct oxidizing SOFC anode. The research

focus includes understanding the reactivity of these potential anode catalysts towards methane oxidation and resistance to carbon deposition. The effect of doping CeO_2 into the catalyst support and the low temperature operation of each catalyst are also studied.

References

[1] Proceedings of a Binational Symposium, Environment Canada, May 13-15, 1997

[2] *Caring for climate,* UNFCCC (2003) Bonn, Germany

[3] *CO_2 emissions data for 1998 from Energy Information Administration,* US Department of Energy: 1990-1999

[4] *Fuel Cell Handbook,* 5th Edition, U.S. Department of Energy, Office of Fossil Energy, National Energy, Technology Laboratory

[5] L. Carrette, K. A. Friedrich, U. Stimming, *Fuel Cells,* Vol. 1, 2001, 5

[6] H. Nagamoto, *Fuel Cells: Electrochemical Reactions,* Encyclopedia of Materials: Science and Technology

[7] J. Grunes, J. Zhu, M. Yang, G. A. Somorjai, *Catalysis Letters,* Vol 86, 2003, 157

[8] P. V. Wright, *Electrochimica Ac*ta, Vol 43, 1998, 1137

[9] Automotive Design & Production. 115, Vol 12, 2003, 34

[10] T. Schultz, S. Zhou, K. Sundmache, *Chemical Engineering & Technology*, Vol 24, 2001, 1223

[11] D. Booth, *Home Power,* Vol.35, 1993

[12] K. Eguchi, *Handbook of Fuel Cells,* Vol 4, Chapter 75, 2003, John Wiley & Sons,

[13] N. U. Pujare, K. W. Semkow, A. F. Sammells, *Journal of the Electrochemical Society,*

Vol 134, 1987, 2639

[14] M. Liu, P. He, J. L. Luo, A. R. Sanger, K. T. Chuang, *Journal of Power Sources*, Vol 94, 2001, 20

[15] P. Holtappels, U. Stimming, *Handbook of Fuel Cells,* Vol 1, Chapter 20, 2003 John Wiley & Sons.

[16] *Automotive Engineering International.* 111, Vol 3, 2003, 54

[17] M. Cropper, *Fuel Cell Today*, 9th February 2004, 753

[18] S. Geiger, *Fuel Cell Today*, 22nd March 2004, 789

[19] D. Jollie, *Fuel Cell Today*, 18th December 2002, 540

[20] S. Geiger, *Fuel Cell Today*, 29th December 2003, 735

[21] F. Igot, *Montgomery College Student Journal of Science & Mathematics*, Vol 1, September 2002, 15

[22] K. W. A. Guy, *Trans IChemE*, Part B, Vol 78, July 2000, 321

[23] *Hydrogen Basics*, U.S. Department of Energy, May 2003,

[24] M. Inoue, *A guide to Hybrid Synergy Drive*, Toyota Motors Corporation, December 2003

Chapter 2

Literature Review

2.1 Technical Overview and Thermodynamics of Fuel Cells

Fuel cells are devices that convert the chemical energy of the fuel to electrical energy. The most well known reaction that takes place in most of the fuel cells is the oxidation of hydrogen [1, 2]. Figure 2-1 shows a schematic for typical PEM fuel cell operation. Fuel cells consist of an anode (negative electrode), cathode (positive electrode), and electrolyte. The hydrogen undergoes catalytic reaction on the anode to split into protons and electrons. The electrons are conducted through the external circuit to the cathode. Oxygen is fed to the cathode and becomes oxygen ions by receiving these electrons. The protons at the anode migrate through the electrolyte to the cathode where they react with oxygen ions to produce water. The only by-product from this process is frequently claimed to be water and heat; therefore, fuel cells are often called "zero emission". As stated in the previous chapter, this zero emission designation is only correct if the hydrogen fuel is produced without CO_2 emissions. Therefore, the overall energy efficiency is still important even for fuel cells.

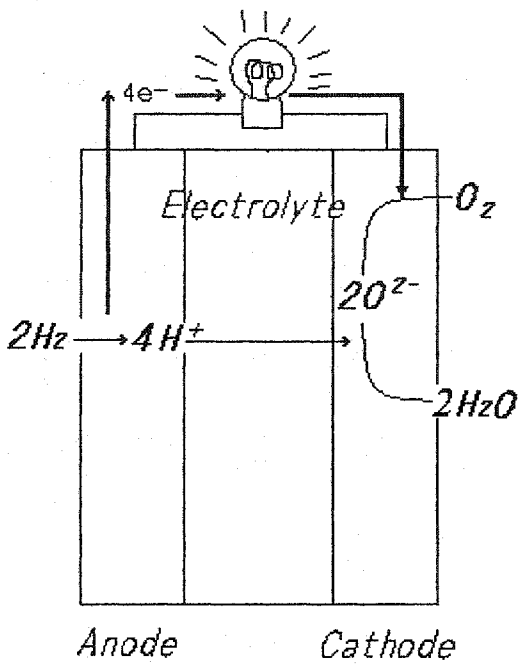

Figure 2-1. Schematic of the PEM operation [1, 2].

The maximum energy that can be derived from the chemical reactions is equal to the Gibbs free energy of the reaction, represented as ΔG [1, 2, 3]. The maximum electrical energy output is the product of the number of electrons involved in the electrochemical reaction (n), the Faraday constant (F = 96,485 C /mol), and the electromotive force (emf). Emf is the voltage of the cell in the absence of current flow, which is determined from the Nernst equation expressed as:

$$E = E^{o} - \frac{RT}{nF} \ln \prod (a_i)^{vi} \qquad (2\text{-}1)$$

where a_i represents the activity and ν_i represents the stoichiometric coefficients of the *i*th specie in the chemical reaction. ν_i is negative for the reactants and positive for the products. E and E^o are the actual emf at temperature T and at standard state at temperature T, respectively.

One of the most important criteria to evaluate the performance of fuel cells is the efficiency. This value allows the comparison of the performance of fuel cells with other energy generating systems. The more efficiently the cells operate, the less CO_2 emissions they produce, which contributes towards the prevention of global warming. Fuel cells are often compared with internal combustion operations, such as turbines. The efficiency is defined as the work output divided by the enthalpy of the reactions. All internal combustion efficiencies are compared with Carnot cycle efficiency, which is expressed as equation (2-2) [1, 2]. On the other hand, the ideal efficiency for fuel cells is determined by equation (2-3). For both internal combustion and fuel cells, the actual efficiencies are determined by (2-4).

$$\eta_{carnot} = \frac{W_r}{-\Delta H} = \frac{T_h - T_l}{T_h} \tag{2-2}$$

$$\eta_{r,cells} = \frac{W_r}{-\Delta H} = \frac{nFE}{-\Delta H} = \frac{\Delta G}{-\Delta H} \tag{2-3}$$

$$\eta = \frac{useful\ energy}{-\Delta H} \tag{2-4}$$

There are two different types of efficiencies; the Lower Heating Value (LHV) and Higher Heating Value (HHV). The former is based on the reaction with water vapor as the product, and the latter liquid water [1, 2]. For the example of hydrogen oxidation, the two possible reactions are;

$$H_2(g) + \tfrac{1}{2}O_2(g) \rightarrow H_2O(v) \qquad \Delta H = -241.83\ \text{kJ/mol (LHV)} \tag{2-5}$$

$$H_2(g) + \tfrac{1}{2}O_2(g) \rightarrow H_2O(l) \qquad \Delta H = -285.84\ \text{kJ/mol (HHV)} \tag{2-6}$$

Equation (2-5) shows the reaction of hydrogen and oxygen to water vapor and equation (2-6) the same reaction with the product being liquid water. The enthalpy of reaction for the former is the LHV and for the latter the HHV for the oxidation of hydrogen. The difference in HHV and LHV is the enthalpy of vaporization of the water. Unless stated, the efficiency is often the LHV. Fuel cells have significantly higher efficiency than internal combusting devices achieving about 40%, and even 80% is possible with co-generation [4].

As introduced in the previous chapter, there are many hurdles for a hydrogen-based

infrastructure due to its low availability, high handling risks, and storing and transportation difficulties. Even if these issues can be adequately addressed, the total energy efficiency is not appreciably high. In vehicular applications in which cogeneration is difficult, the low tank-to-wheel efficiency will even result in lower overall efficiency than conventional internal combustion powered hybrid vehicles.

The direct use of hydrocarbons, such as natural gases, in fuel cells is one of the most effective methods to improve the total energy efficiency of a fuel cell based energy infrastructure, and SOFCs are the most promising candidate. As indicated in Figure 2-2, SOFCs allow oxygen ion conduction from the cathode to anode instead of the proton from the anode to cathode. Therefore, it enables direct oxidation of the hydrocarbon at the anode. However, deactivation caused by coking on the SOFC anode is a primary problem that needs to be eliminated [5]. The typical approach to avoid carbon deposition is to co-feed excess steam, or even carbon dioxide, with the hydrocarbons which then undergo internal reforming to hydrogen before the fuel is oxidized. Attempts are also made to prevent coking without steam reforming, which is known as "direct oxidation". This is done by modifying the materials and structures of the anode of the cells. In this chapter, previous work on both approaches is reviewed.

2.2 Steam Reforming of Hydrocarbons in SOFCs

Currently, steam reforming is the most common technique to use hydrocarbons in SOFCs [6], and is often accompanied with the water gas shift reaction (2-7 and 2-8, respectively). Depending on the cell type, this reforming is done either externally or internally. Internal reforming is further classified in two categories; direct and indirect internal reforming. Schematics for these processes are shown in Figure 2-3.

$$CH_4(g) + H_2O(v) \rightarrow CO(g) + 3H_2(g) \qquad (2\text{-}7)$$

$$CO(g) + H_2O(v) \rightarrow CO_2(g) + H_2(g) \qquad (2\text{-}8)$$

External and indirect internal reforming requires an independent reformer outside of the fuel cell stack, while direct internal reforming is performed directly on the cell anodes. Obviously, direct internal reforming is preferred for its simpler construction, which results in lower costs and a smaller space requirement. Steam reforming is a highly endothermic reaction and, therefore, requires high temperatures to undertake direct internal reforming. A temperature between 750 and 850 °C is favorable [6, 7].

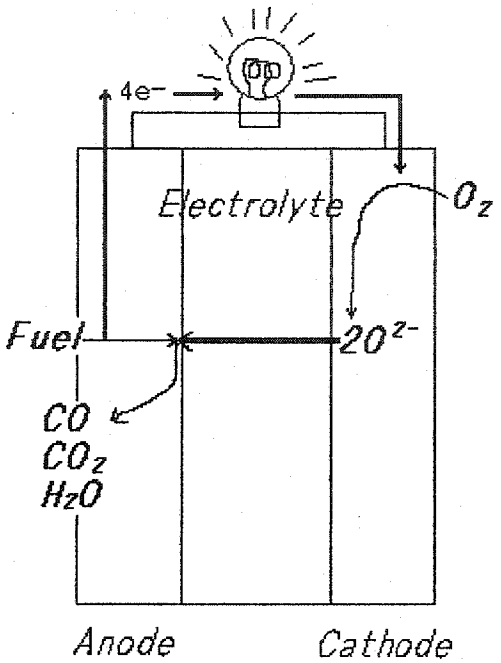

Figure 2-2. The schematic of the SOFC operation.

In an SOFC, the oxygen ion is conducting through the electrolyte instead of protons. Therefore, the fuel is not limited to hydrogen. CO and CO_2 are produced at the anode when a hydrocarbon is fed to the anode. The schematic was prepared based on references [1, 2].

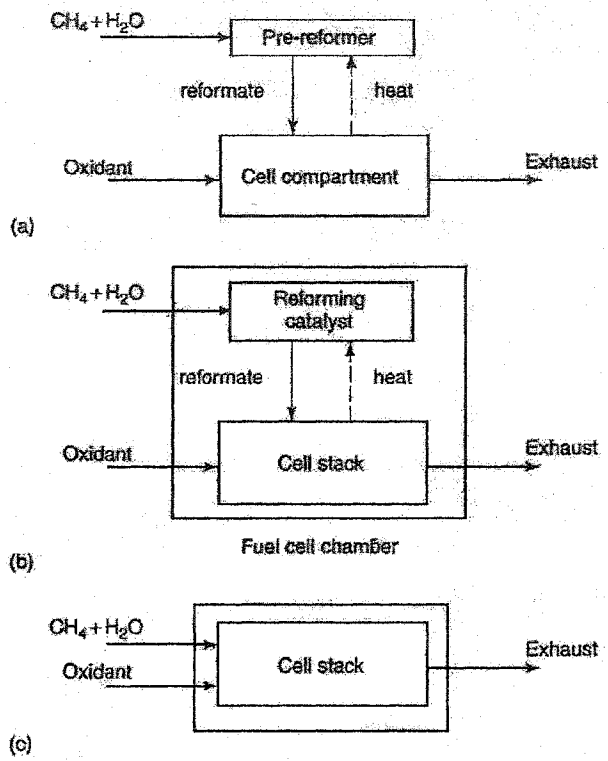

Figure 2-3. Schematics for different types of steam reformings [6].

(a) External, (b) Indirect internal, (c) Direct internal.

The enthalpy of reaction expressed by (2-7) at 727 °C is +225.67 kJ/mol (this calculation is based on the data provided by [3]) Because of the highest heat transfer, direct internal reforming has an advantage over other methods. On the other hand, this technique has the highest probability of carbon deposition [8]. Moreover, this endothermicity creates a temperature gradient within the anode, in which case the thermal

expansivity, α, expressed by equation (2-9), is another limitation for the choice of anode material and structure [3, 9].

$$\alpha = \frac{1}{V}\left(\frac{\partial V}{\partial T}\right)_P \tag{2-9}$$

Pure nickel, the typical material for steam reforming and anode catalysts for SOFCs, has high thermal expansivity compared with 8YSZ (8 mol% yttria-stabilized-zirconia), the most commonly used SOFC electrolyte. Nickel is usually diluted with 8YSZ to reduce its thermal expansivity neat to that of 8YSZ. Typically, 30 – 50 wt% nickel in 8YSZ is considered to be optimal [9].

To avoid coking, the steam-to-methane ratio of the feed gas has to be greater than 2. However, this ratio should be as low as possible since a higher ratio will result in lower energy efficiency. Sauvet and Fouletier [9] studied the catalytic properties of ruthenium- and vanadium-doped LSC (lanthanum-strontium-chromite) for steam reforming and coking at a steam-methane ratio between 0.07 – 0.7. Both ruthenium and vanadium increased the resistance to carbon formation on the LSC. While they reported no carbon deposition, the reactivities of steam reforming were different. The higher ruthenium concentration led to higher reactivity; however, vanadium did not alter reactivity

significantly. Catalysts without ruthenium showed a decrease in reactivity with an increasing steam-methane ratio. The same investigation was performed on copper, molybdenum, praseodymium and gadolinium by the same authors showing that carbon deposition was the most severe on molybdenum. Gadolinium was shown to be sensitive to steam-methane ratios. Copper and praseodymium were also free from carbon deposition like ruthenium; however, these catalysts showed very low activity.

Andersen et al. [10] focused on the surface structure of the catalyst and studied its effect on steam reforming and carbon deposition. In their work, Ni/Al_2O_3 and $Ni/MgAl_2O_4$ were poisoned by hydrogen sulfide. The sulfur poisoned the steam reforming process; however, it poisoned more severely the carbon formation process. As a result, sulfur poisoning increased the selectivity of steam reforming over carbon formation.

Similar work was done by Besenbacher et al. [11]. In their study, gold was alloyed on the first surface layer of nickel to increase its resistance to carbon formation. The gold and nickel are miscible and, therefore, gold atoms that are deposited on the nickel surface change the electronic structure (Figure 2-4). Specifically, the deposition of gold atoms on the nickel surface slightly increased the activation energy to extract the first hydrogen from methane, which is the limiting step for steam reforming. Therefore, gold slightly

decreased the reactivity of catalysts for steam reforming. Similar to previous work [10], depositing gold atoms on the nickel surface had strongly suppressed the carbon formation process. The tendency towards carbon deposition is proportional to the stability of carbon adsorption on the nickel surface. Theoretically, depositing gold atoms on a nickel surface destabilizes carbon adsorption, thus adsorbed carbon atoms are more active to undergo further reaction with adsorbed oxygen molecules (Figure 2-5). This was demonstrated by their experiment in which $Ni/MgAl_2O_4$ (16.5 wt% nickel) and the same catalyst with 0.3 wt% of gold were compared for the activity of steam reforming of n-butane.

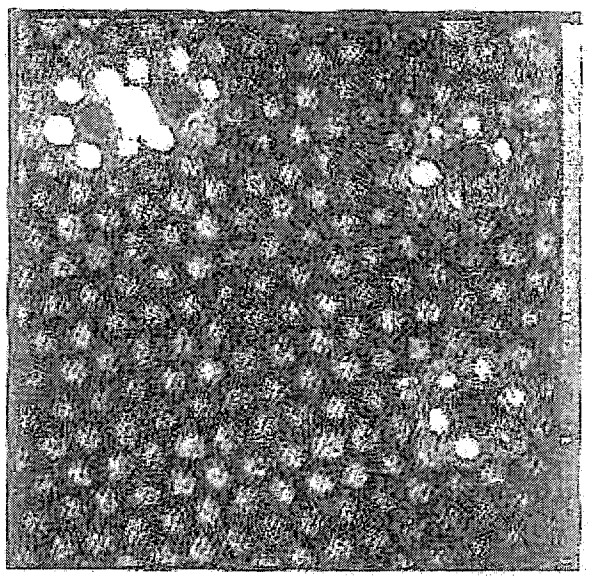

Figure 2-4. STM image of gold particles deposited on the surface of nickel [11]. The gold particle appears in black and white ones are neighboring nickel atoms.

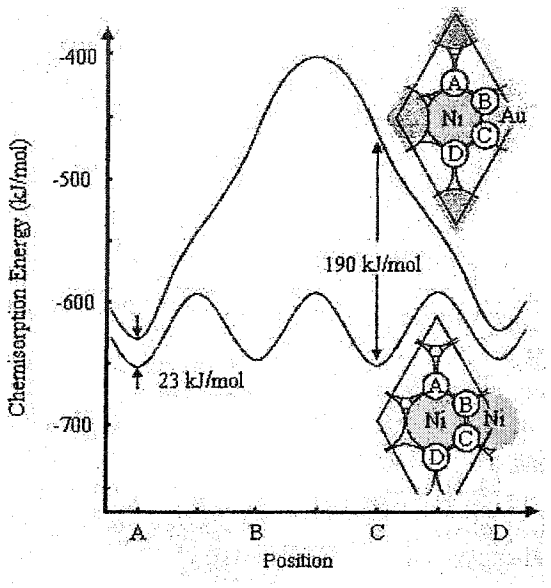

Figure 2-5. Calculated adsorption energy of C atom on nickel [11].

Figure 2-4 and 2-5 were reproduced with the permission by J. K. Norskov.

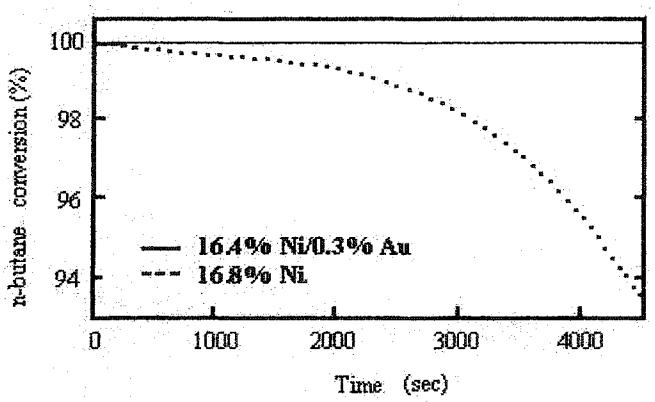

Figure 2-6. Conversion of n-butane as a function of time during steam reforming [11].

Reproduced with the permission by J. K. Norskov.

As can be seen in Figure 2-6, the former was quickly deactivated by carbon deposition while the latter was not. The most important conclusion from their work is that only a slight amount of gold is needed to change the catalytic property of nickel; therefore, it does not require a high fabrication cost.

2.3 CO_2 Reforming

Another reforming technique that has been receiving considerable attention is CO_2 reforming [8, 12-14], represented by equation (2-10). The enthalpy of this reaction is similar to steam reforming, which is about +260.42 kJ/mol at 727 °C [3].

$$CH_4 + CO_2 \rightarrow 2CO + 2H_2 \qquad (2\text{-}10)$$

This is an interesting method for not only producing useful fuel for the cells but also consuming CO_2, the primary greenhouse gas. In addition, CO_2 reforming gives higher conversion of methane than steam reforming [12]. This technique can be another method for the direct use of hydrocarbons on SOFCs; however, this technique also suffers from carbon deposition.

The most common catalysts used for CO_2 reforming are nickel-based. Lercher et al.

[13] noted severe coking caused by too high nickel loading on their catalyst, while Li et al. [14] were successful in carbon-free operation with high nickel content catalysts. Li et al. investigated the effect of lanthanum, cerium and manganese oxide on the catalyst support. Doping cerium and manganese oxide on the zirconia support greatly reduced carbon formation; however, the catalyst had low activity. Lanthanum increased the activity but showed the highest rate of coking. They also investigated the effect of doping alkaline earth metals, namely magnesium, calcium and barium, with nickel. Doping magnesium increased the activity of the catalyst, and calcium and magnesium enhanced the thermal stability of the catalyst.

Hu and Ruckenstein [15] studied the catalytic properties of NiO/MgO, and showed NiO/MgO had high CO yield, excellent stability, and carbon-free operation. Additionally, they investigated the effect of sample calcination time on catalytic performance. Figure 2-7 gives a comparison of the reactivity with catalyst preparation method. This shows that longer calcination times on mechanically mixed catalysts significantly increases their reactivity (a, b, c), and samples prepared by wet impregnation show higher reactivity (d). However, as shown in Figure 2-8 calcination time for catalysts prepared by wet impregnation does not affect performance. These results imply that it is easier for NiO to diffuse into MgO after wet impregnation than the two forming a solid solution during

calcination without prior wet impregnation. Curve c in Figure 2-7 shows significant deactivation, and it was suggested this resulted from insufficient time for the mixing of the metal oxides. Thus, some nickel particles were not affected by magnesium oxide. It should be noted CO_2 reforming has a key advantage over steam reforming in specific cases, such as utilizing biomass gas, in which vast amounts of CO_2 coexist with methane [16].

2.4 Direct Oxidation of Dry Hydrocarbons in SOFCs

Many reforming techniques have low hydrocarbon to hydrogen conversion, typically in the range of 20 – 50% [17]. Even with 100% conversion, as noted in previous work [11], steam and CO_2 reforming requires an external heat supply since both reactions are highly endothermic. Furthermore, additional energy is required to heat up either water or CO_2 from room temperature to high operating temperatures. This not only results in lower efficiency, but also higher capital costs due to increased complexity. Direct oxidation of dry hydrocarbons is a promising alternative to eliminate the drawbacks associated with reforming. Unfortunately, direct oxidation of dry hydrocarbons also suffers from carbon formation [18-22].

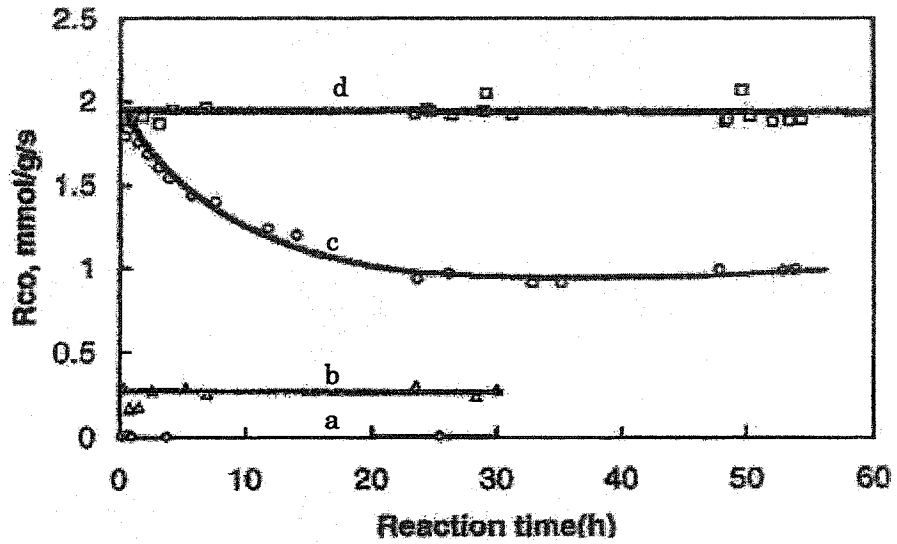

Figure 2-7. Relationship between the rate of formation of CO and the reaction time over NiO/MgO catalysts.

(a) catalyst obtained by mechanical mixing NiO and MgO powders, (b) catalyst obtained by mechanical mixing of NiO and MgO followed by calcination in air at 800 °C for 1.5 h. (c) catalyst obtained by mechanical mixing of NiO and MgO followed by calcination in air at 800 °C for 14 h. (d) catalyst obtained by wet impregnation followed by calcination in air at 800 °C for 1.5 h.

Source: Ref [15]. Reproduced with the permission of E. Ruckenstein

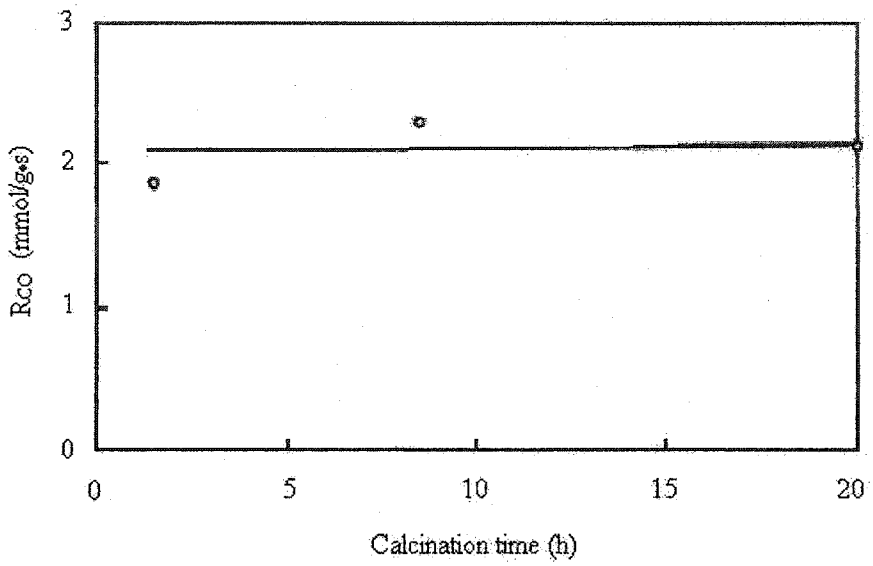

Figure 2-8. CO formation and calcination time.

Source: Ref [15]. Reproduced with the permission of E. Ruckenstein

One of the earliest attempts at direct oxidation was reported in 1995, in which a samaria-doped-ceria (SDC) anode catalyst with and without rhodium doping was studied with methane fuel [18]. In this study, four different cells were tested (labeled as cells a, b, c, and d in Figure 2-9); 10 mg and 100 mg of SDC were used on the anodes of cells a and b, respectively; cells c and d had 10 mg and 100 mg of SDC, respectively, with 0.14 mg of Rh deposited. Figure 2-9 shows the potential of each catalyst for the electrochemical oxidation of methane. These figures indicate that both SDC and rhodium have a very important role in oxidation catalysis. Specifically, the incorporation of Rh improves the

cell power density up to the level achieved by hydrogen as the fuel instead of methane.

Murray et al. [19] modified conventional anodes, namely nickel supported 8YSZ, by introducing YDC (i.e., $(CeO_2)_{0.85}(Y_2O_3)_{0.15}$) between the electrolyte and anode layers. This was shown to significantly reduce the impedance. They also reported that their catalysts did not experience any carbon deposition below 700 °C, and the amount of adsorbed carbon increased as the temperature increased. Additionally, catalysts with ceria had significantly less carbon than ones without.

The most successful SOFC work to date was done by Vohs et al. [20-22], in which they replaced nickel with copper at the anode. They demonstrated that copper is highly resistant to carbon formation. In Figure 2-10, it can be seen that nickel is severely damaged by carbon formation while Figure 2-11 shows that copper rarely shows any effect upon exposure to methane or toluene [20]. Although Cu/8YSZ is resistant to carbon formation, the power density is very low, especially at high currents. This was greatly improved by doping ceria into the catalyst support [21]. Figure 2-12 shows voltage vs. current density of the cell, which indicates a significant increase in the voltage, thus increasing power densities at high current densities.

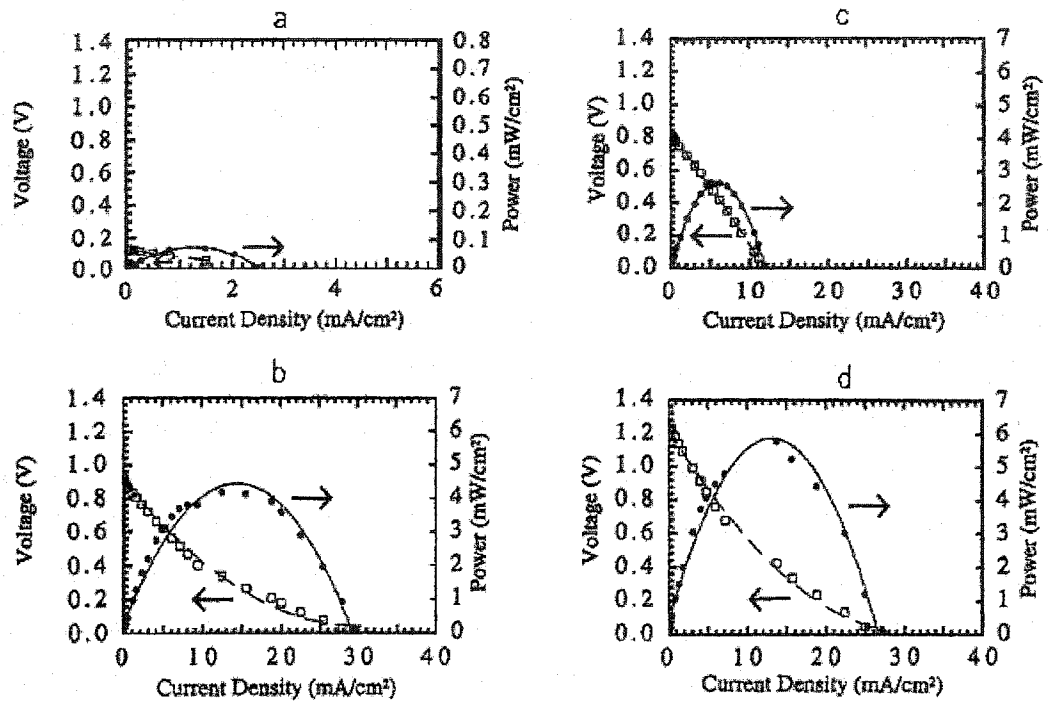

Figure 2-9. Power densities and cell voltage vs. current densities for four different types of cells with methane [18]. (a) 10 mg SDC, (b) 100 mg SDC (c) 10 mg SDC with 0.14 mg Rh and (d)100 mg SDC with 0.14 mg of Rh.

Reproduced with the permission of J. M. Vohs.

Ceria doping as $Cu/CeO_2/8YSZ$ was also tested for various hydrocarbons and produced similar results with each fuel tested. The catalysts were stable for three hours operation without any degradation (Figure 2-13). Further prevention of carbon formation was achieved by doping samarium oxide with ceria in the catalyst support [21]. The power density decreases to zero in a toluene environment with a $Cu/CeO_2/8YSZ$; however, this degradation was reduced with Cu/Sm_2O_3-$CeO_2/8YSZ$ (Figure 2-13).

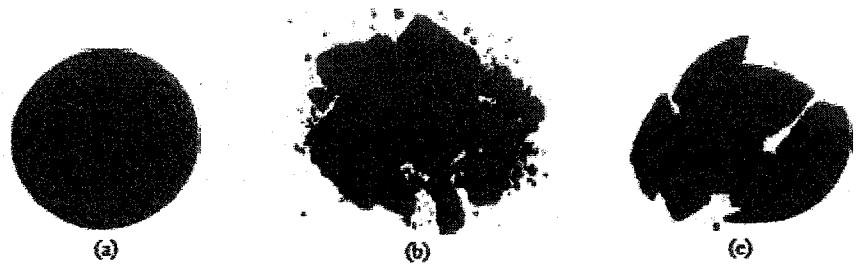

Figure 2-10. Photographs of a Ni/8YSZ cermet exposed to hydrocarbons and hydrogen. (a) after heating in H_2 at 800 °C, (b) after heating in 100% CH4 at 800 °C for 1.5h, and (c) after heating in 40% toluene at 700 °C for 1.5 h [20].

Reproduced with the permission of J. M. Vohs.

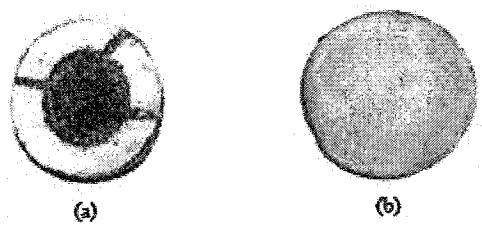

Figure 2-11. Photographs of a Cu/8YSZ cermet exposed to hydrocarbons.

(a) after heating in CH_4 at 800 °C for 1.5 h and (b) after heating in 40% toluene at 700 °C for 1.5 h [20].

Reproduced with the permission of J. M. Vohs.

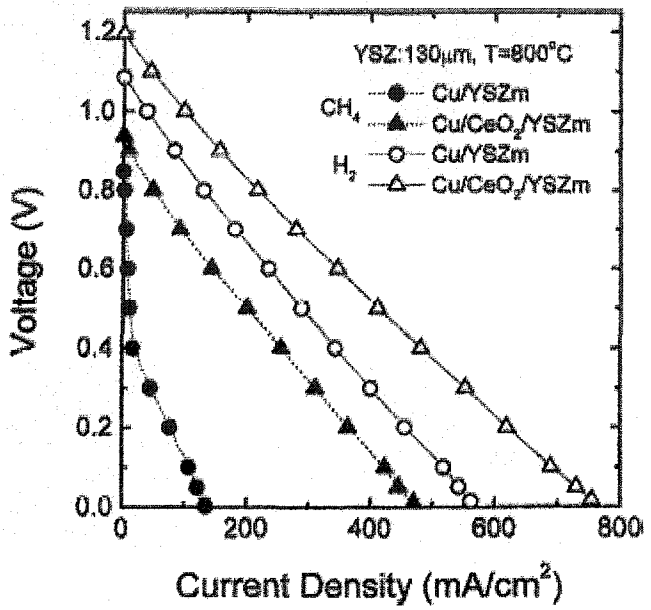

Figure 2-12. Voltage vs. current density for SOFCs with Cu/8YSZ and $Cu/CeO_2/8YSZ$ anodes [21].

Reproduced with the permission of J. M. Vohs.

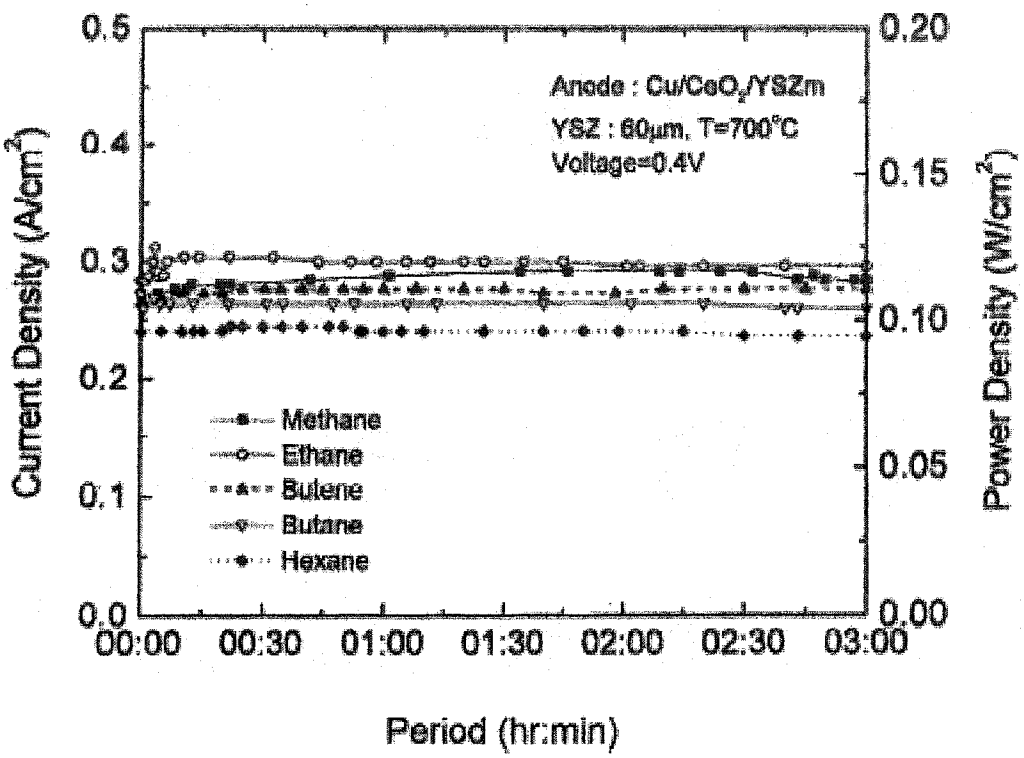

Figure 2-13. Current density vs. Time for SOFC with a $Cu/CeO_2/8YSZ$ anode operating with various hydrocarbons [21].

Reproduced with the permission of J. M. Vohs.

The relation between degree of carbon formation and the alloy composition of nickel and copper was also studied [23], showing that a higher concentrations of copper contributes to reducing the degree of carbon formation. The direct oxidation test with copper-ceria cermet was studied using ethane, n-butane and toluene at 800 °C [24]. In this work, the authors succeeded in the suppression of coking using ethane and n-butane and

reported 48 hours of stable operation. Severe deactivation was confirmed after an hour when toluene was used as the fuel; however, the power output was completely recovered by switching the fuel from toluene to n-butane. It should be noted the power density was far lower than the nickel-ceria cermet [24, 25]. To have practical operation, this low power density needs to be improved.

While considerable research has provided gains towards the development of SOFCs, there are several limitations preventing the commercialization of direct oxidizing SOFCs. Therefore, the objective of this research is to examine other transition metals, namely cobalt and silver, for their activity and carbon deactivation using dry hydrocarbons as fuels for SOFC operation. Studying the properties and catalytic activity of other materials may yield more possibilities in alloying combinations to optimize anode performance. Cobalt and silver are neighboring elements to either copper or nickel, and studying their properties in regards to the direct oxidation of hydrocarbons may give insight as to trends in the reactivity or resistance to carbon formation across the periodic table.

References

[1] L. Carrette, K. A. Friedrich, U. Stimming, *Fuel Cells,* Vol. 1, 2001, 5

[2] *Fuel Cell Handbook,* 5th Edition, U.S. Department of Energy, Office of Fossil Energy, National Energy, Technology Laboratory, Morgantown, West Virginia

[3] *Physical Chemistry;* sixth edition, Gordon M. Barrow, McGraw Hill

[4] F. Igot, *Montgomery College Student Journal of Science & Mathematics*, Vol. 1, September 2002

[5] P. Holtappels, U. Stimming, *Handbook of Fuel Cells,* Vol 1, Chapter 20, 2003 John Wiley & Sons

[6] K. Eguchi, *Handbook of Fuel Cells,* Vol 4, Chapter 75, 2003 John Wiley & Sons

[7] S. Katikaneni, C. Yuh, S. Abens, M. Farooque, *Catalysis Today,* Vol. 77, 2002, 99

[8] J. T. S. Irvine, A. Sauvet, *Fuel Cells,* Vol. 1, 2001, 205

[9] A. L. Sauvet, J. Fouletier, *Journal of the Power Sources*, Vol. 101, 2001, 259

[10] N. T. Andersen, F. TopsPe, I. Alstrup, J. Rostrup-Nielsen, *Journal of Catalysis*, Vol. 85, 1984, 31

[11] F. Besenbacher, I. Chorkendorff, B. S. Clausen, B. Hammer, A. M. Nolenbroek, J. K. Norskov, I. Stensgaard, *Science*, Vol. 279, 1913

[12] T. Inui, *Applied Organometallic Chemistry,* Vol. 15, 2001, 87

[13] Lercher JA, Bitter JH, Hally W, Niessen W, Seshan K. *Studies in Surface Science and Catalysis,* Vol. 101, 1996, 463

[14] X. Li, J. Chang, M. Tian, S. Park, *Applied Organometallic Chemistry*. Vol. 15, 2001, 109

[15] Y. H. Hu, E. Ruckenstein, *Catalysis Letters*, Vol. 43, 1997, 71

[16] J. Staniforth, R. M. Ormerod, *Catalysis Letters,* Vol. 81, 2002, 19

[17] P. Vernoux, J. Guindet, M. Kleintz, *Journal of the Electrochemical Society,* Vol. 145, 1998, 3487

[18] E. S. Putna, J. Stubenraunch, J. M. Vohs, R. J. Gorte, *Langmuir* Vol. 11, 1995, 4832.

[19] E. P. Murray, T. Tsai, S. A. Barnett, *Nature,* Vol. 400, 1999, 649

[20] R. J. Gorte, J. M. Vohs, *Journal of Catalysis*, Vol. 216, 2003, 477

[21] S. Park, R. J. Gorte, J. M. Vohs, *Applied Catalysis A: General*, Vol. 200, 2000, 55

[22] R. J. Gorte, S. Park, J. M. Vohs, C. Wang, *Advanced Materials,* Vol. 19, 2000, 1465

[23] H. Kim, C. Lu, W. L. Worrell, J. M. Vohs, R. J. Gorte, *Journal of The Electrochemical Society*, Vol. 149, 2002, A247

[24] S. Park, J. M. Vohs, R. J. Gorte, *Nature*, Vol. 404, 2000, 265

[25] S. Park, R. Craciun, J. M. Vohs, R. J. Gorte, *Journal of The Electrochemical Society*, Vol. 146, 1999, 3603

Chapter 3

Experimental

3.1 Objective

As discussed in the previous chapters, the objective of this research is to investigate the properties of nickel-, copper-, cobalt-, and silver-based catalysts for the direct oxidation of hydrocarbons for SOFC applications. The main focus is their reactivity towards methane oxidation and resistance to carbon deposition. The effect of doping CeO_2 into the catalyst support is also studied. Consequently, a variety of techniques are required to characterize the catalysts and their subsequent reactivity.

3.2 Catalyst Preparation

Eight different catalysts were prepared for these experiments, specifically M/8YSZ and M/CeO_2/8YSZ in which M is Ni, Cu, Co or Ag. All of the catalysts were prepared by wet impregnation techniques with pure water. The commercial 8YSZ powder (8 mol% yttria-stabilized-zirconia, Tosoh) was physically mixed with each metal nitrate powder (all purchased from Aldrich) to achieve a final metal loading of approximately 10 mol%. The nitrates used in this step are listed in Table 3-1 and 3-2. Excess water (4 – 10 mL)

was added to the mixture of nitrates and 8YSZ, and the mixture was stirred. The nitrates were well dissolved in the water, and the mixture was dried in an oven at 100 °C overnight to completely evaporate off the water and subsequently calcined in an atmospheric furnace at 950 °C. The samples were calcined for 2 hr, and the heating and cooling rates during calcination were 3 and 5 °C/min, respectively. During the drying and calcination steps, the sample was in an air (O_2/N_2) environment. Following calcination, the catalysts were ground into a fine powder using a mortar and pestle. The composition of each component in the mixtures is listed in Table 3-1. Additionally, CeO_2/8YSZ was prepared to produce M/CeO_2/8YSZ catalysts. CeO_2/8YSZ powder was mixed with each nitrate and excess water, followed by drying and calcination using the same method previously described for M/8YSZ catalysts. The mixed amount of CeO_2/8YSZ and each metal nitrate are shown in Table 3-2. These quantities were chosen such that the final metal loadings are at 20 mol%, and CeO_2 and 10 mol% metal.

Catalyst name	Formulae of nitrate compounds	Mass of mixed nitrate compounds (g)	Mass of mixed 8YSZ (g)
Ni/8YSZ	$Ni(NO_3)_2 \cdot 6H_2O$	5.56	10.09
Cu/8YSZ	$Cu(NO_3)_2 \cdot 2.5H_2O$	4.43	10.04
Co/8YSZ	$Co(NO_3)_2 \cdot 6H_2O$	5.53	10.14
Ag/8YSZ	$AgNO_3$	3.21	10.14
CeO_2/8YSZ	$Ce(NO_3)_3 \cdot 6H_2O$	18.80	40.00

Table 3-1. Amounts of nitrates and 8YSZ mixed in the catalyst preparation step.

Eccess water (about 4 mL) was added to each mixture and was stirred to mix well. The mixture was dried in the oven at 100 °C overnight and calcined at 950 °C.

Catalyst name	Formulae of nitrate compounds	Mass of mixed nitrate compounds (g)	Mass of mixed CeO_2/8YSZ (g)
Ni/CeO_2/8YSZ	$Ni(NO_3)_2 \cdot 6H_2O$	5.07	9.51
Cu/CeO_2/8YSZ	$Cu(NO_3)_2 \cdot 2.5H_2O$	4.06	9.51
Co/CeO_2/8YSZ	$Co(NO_3)_2 \cdot 6H_2O$	5.07	9.51
Ag/CeO_2/8YSZ	$AgNO_3$	2.97	9.52

Table 3-2. Amounts of nitrates and CeO_2/8YSZ mixed in the catalyst preparation.

3.3 Characterization by BET Surface Area Measurement

BET surface area measurements were performed on each catalyst using Autochem II 2920 (Micromeritics) chemisorption/physisorption analyzer. A quartz test tube was attached to the instrument and the sample catalyst was held in place by quartz fiber in the tube as shown in Figure 3-1. This test tube was firmly attached to the Autochem 2920 II such that the analysis and carrier gases flow through the catalysts.

Before each measurement, the catalysts were first outgassed in a helium environment at 250 °C for 1 hour. The catalysts were then allowed to cool to room temperature. After the catalyst sample reached thermal equilibrium with the surroundings, as confirmed by the sample temperature stability, the furnace was replaced with a cryogenic bath of liquid nitrogen in which the catalyst was cooled down to approximately -187 °C. This temperature is adequate to perform surface area measurements, although the sample did not reach the temperature of liquid nitrogen (-196 °C). At the same time, a mixture of 30% nitrogen in helium (Praxair) was fed through the sample to facilitate nitrogen adsorption on the surface of the catalyst. After the catalyst surface was saturated with nitrogen, the sample was heated to room temperature by immersing it in a bath of room temperature de-ionized water. During this process, the adsorbed nitrogen is desorbed and consequently the desorption changes the outlet composition of the nitrogen/helium

mixture. This composition change is detected by the thermal conductivity detector (TCD). Figure 3-2 shows a representative TCD plot versus time for Ni/8YSZ. The surface area was automatically calculated based on the desorption curve and equations (3-1), (3-2) and (3-3) [1].

$$SA = \frac{V_m}{22414} \times (6.023 \times 10^{23}) \times A_{N_2} \tag{3-1}$$

$$V_m = V_{STP}\left(1 - \frac{P}{P_0}\right) \tag{3-2}$$

$$V_{STP} = \frac{V_a}{SW} \times \left(\frac{273.15K}{273.15K + T_a}\right) \times \left(\frac{P_a}{760mmHg}\right) \tag{3-3}$$

where SA is the surface area in m^2/g, V_m is the volume of the monolayer in mL, A_{N_2} is the surface area of the N_2 molecule in m^2/molecule, V_{STP} is the volume adsorbed at STP in mL/g, and SW is the sample weight in g, and P, P_0, and P_a are absolute pressure, saturation pressure and ambient pressure of N_2 in mm Hg, respectively

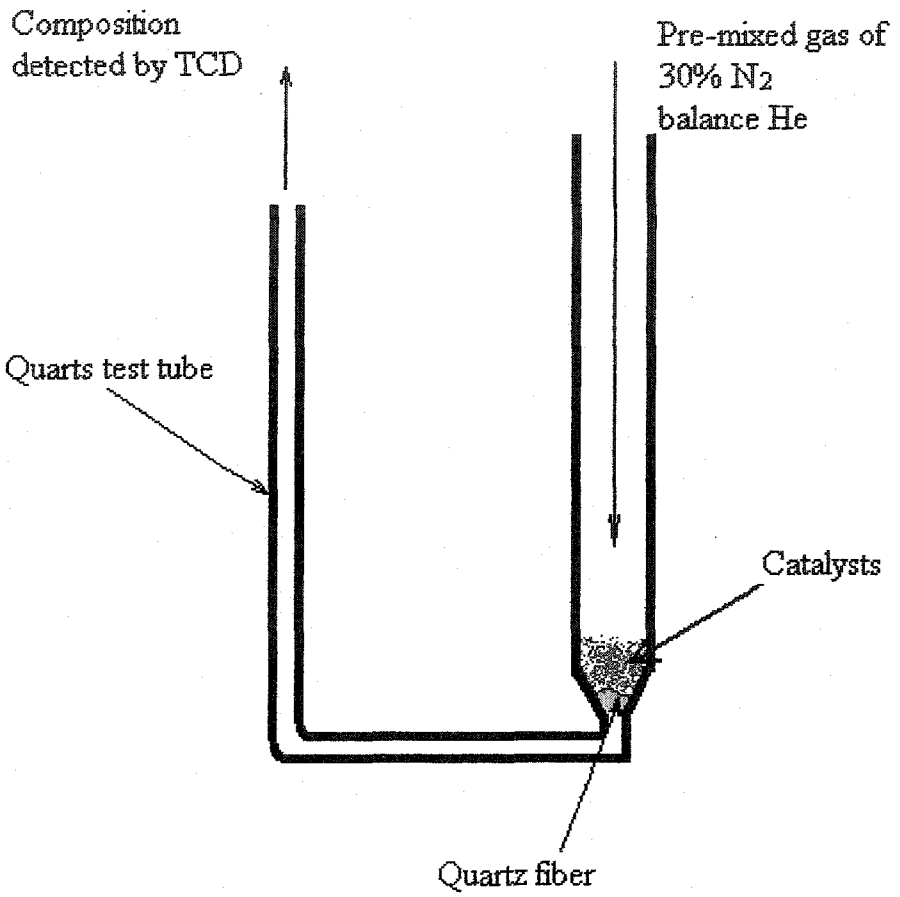

Figure 3-1. Schematic of the catalyst in the quartz test tube.

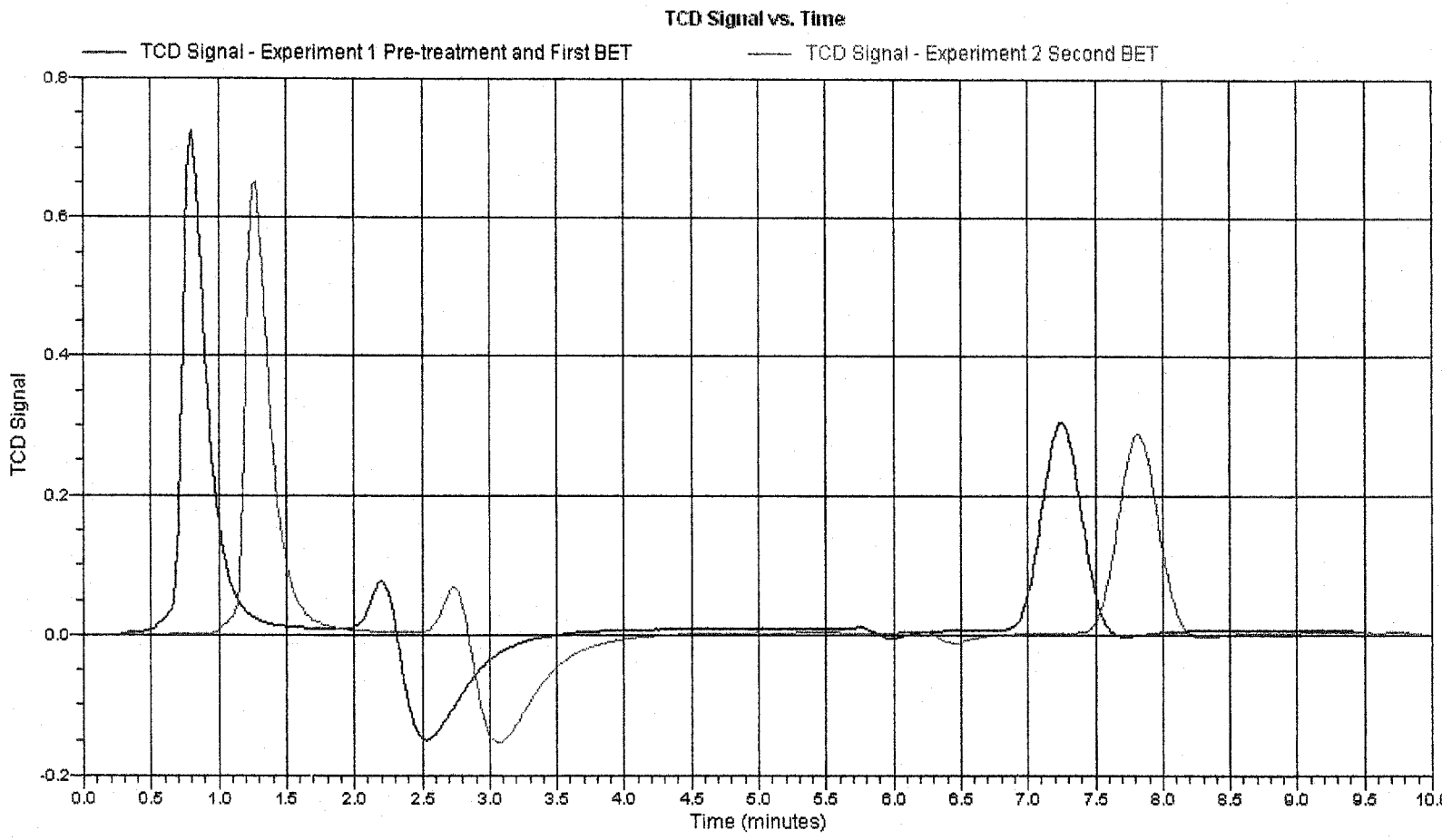

Figure 3-2. TCD signal vs. time for BET surface measurement on Ni/8YSZ

Since the surface area of 8YSZ is relatively low (14 m^2/g, provided by Tosoh), a sample loading of 0.3 – 0.5g was chosen to have a clear desorption curve. A lower sample loading was avoided because the noise resulting from experimental uncertainty becomes significant resulting in lower accuracy.

Considerable attention was needed on the choice of analysis gas and carrier gas for accurate calibration. The TCD detects thermal conductivity, and the composition of the binary mixture is determined from the thermal conductivities of the mixture and each component in the pure state. Therefore, the thermal conductivities of the analysis and carrier gas have to be significantly different to give accurate results. Table 3-3 shows the relative thermal conductivities of the representative gases. In our case, helium was chosen as the carrier since its relative thermal conductivity is 5.84 and that of nitrogen is 1.00, and this difference is far greater than other combinations of noble gases and nitrogen.

Name	Chemical Formula	Conductivity (Relative to Air)
Air		1.00
Ammonia	NH_3	0.92
Argon	Ar	0.68
Butane	C_4H_{10}	0.60
Carbon Dioxide	CO_2	0.62
Carbon Monoxide	CO	0.97
Ethane	C_2H_6	0.79
Helium	He	5.84
Hydrogen	H_2	7.07
Krypton	Kr	0.37
Methane	CH_4	1.29
Neon	Ne	1.87
Nitric Oxide	NO	0.99
Nitrogen	N_2	1.00
Nitrogen Dioxide	NO_2 or N_2O_4	1.51
Nitrous Oxide	N_2O	0.65
Oxygen	O_2	1.02
Sulfur Dioxide	SO_2	0.38
Water Vapor	H_2O	0.67

Table 3-3. Relative thermal conductivities of representative gases based on air being 1 [1].

3.4 Characterization by XPS

X-ray photoelectron spectroscopy (XPS, AXIS 165 Kratos Analytical) was used to determine the metal and ceria loadings on each catalyst.

During XPS, photons are projected onto the surface of the atoms of the sample. The sample atom receives energy ($h\nu$). This energy overcomes the binding energy and the work function of the electrons and the nucleus, $E_{binding}$ and ϕ, respectively. The electron

is then expelled with kinetic energy, $E_{kinetic}$. By measuring the kinetic energy and combining it with an energy balance, the binding energy can be determined from by following relation:

$$h\nu = E_{binding} + E_{kinetics} + \phi \qquad (3\text{-}4)$$

The electrons in all the orbitals of atoms have unique binding energies. Therefore, the atom can be identified from the detected binding energy [2, 3]. XPS data are plotted as peak intensity versus binding energy. The integrated peak area of the intensity is proportional to the amount of the element. The binding energy of interest is representative of oxidation states. Using this technique, the surface concentration of each metal in the catalyst was measured. A representative plot is shown in Figure 3-3, which is the calibration for $Ni/CeO_2/8YSZ$.

For XPS analysis, all of the catalysts were pressed into pellet form (1 cm dia.) under a pressure of 82.7 MPa for 5 minutes. The surface of the catalysts was not cleaned in situ (annealed, sputtered) prior to the experiment; therefore, adsorbed carbon monoxide and carbon dioxide dioxide from air was detected.

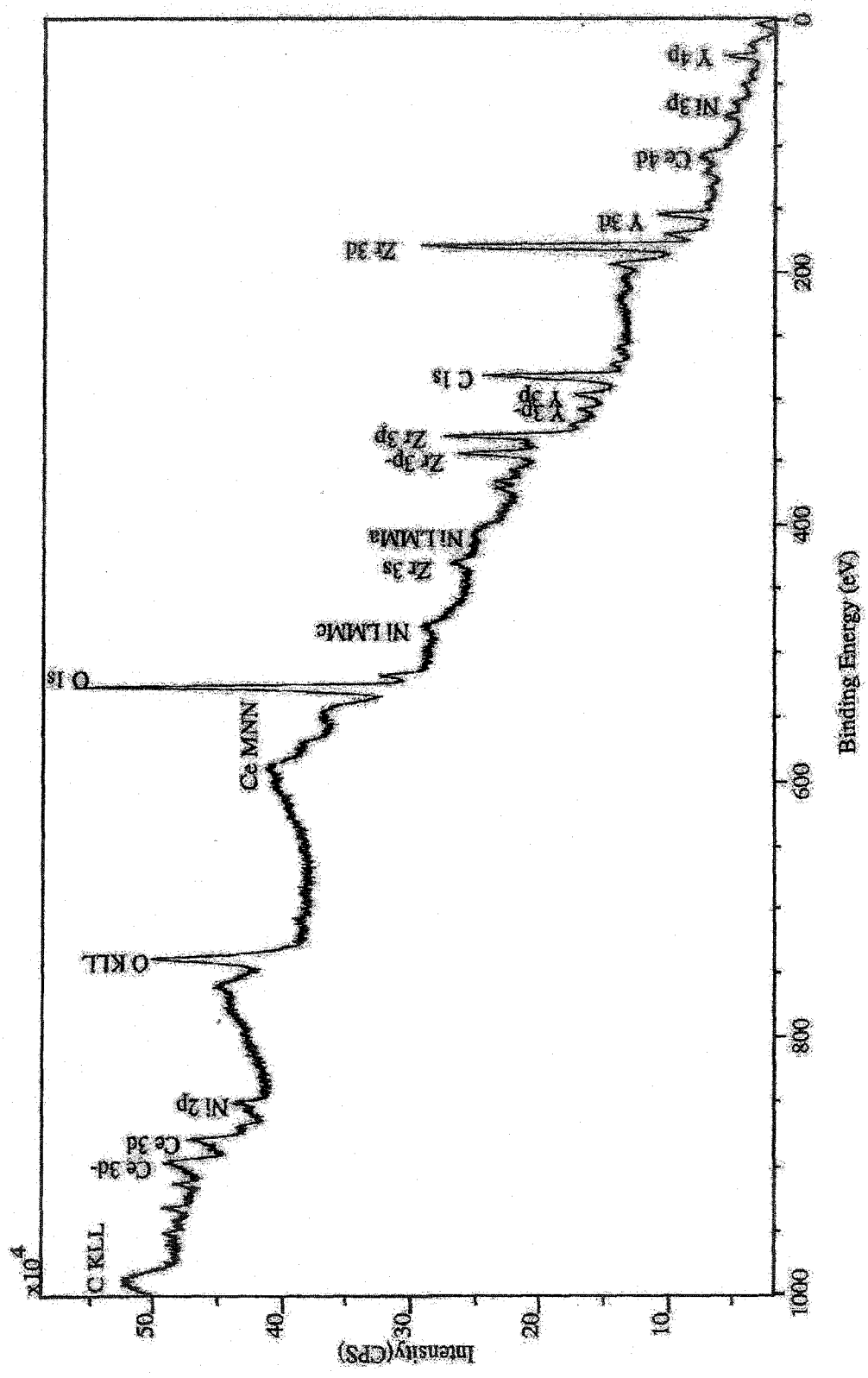

Figure 3-3. Peak intensity of XPS calibration vs. binding energy of each element. This plot is on $Ni/CeO_2/8YSZ$.

3.5 Reaction Tests on the Catalysts

To test the reactivity and resistance to carbon deposition of each catalyst, the combustion of methane was performed using the Autochem II 2920 and a mass spectrometer (Dycor, M200ED). The former equipment was used as a differential flow reactor and the latter as a monitoring device for exhaust gas composition. The mass spectrometer calibrates and calculates the partial pressures of each component in the vacuum chamber. The pressure in the vacuum chamber was approximately at 1×10^{-6} Torr. The mass spectrometry data was collected and recorded by an external computer with a program prepared by the computer support group in the department. The recorded data were exported to Microsoft Excel and was manually organized and plotted.

Before each experiment, the catalysts were reduced in a hydrogen environment for 20 minutes at 800 °C. After reduction of the catalysts, 25 mol% methane and 10 mol% oxygen gas both in helium (Praxair) were fed to the catalysts. The flow rates of the methane and oxygen were manually changed every 20 minutes while maintaining a constant total flow rate to avoid the effect of pressure change. A schematic of the experiment is shown in Figure 3-4. The order of the methane and oxygen compositions is listed in Table 3-4. For the first 20 minutes of the test (period A), the stoichiometric amount of oxygen for complete methane combustion was supplied as seen on the

following equation:

$$CH_4 + 2O_2 \rightarrow CO_2 + 2H_2O \qquad (3\text{-}5)$$

The oxygen concentration was decreased every 20 minutes for the first hour (periods A, B, and C) and increased back to the initial concentration in the last 40 minutes (periods D and E). The hypothesis of this research is carbon formation on an SOFC anode is occurring due to an insufficient oxygen supply. Oxygen supply at the SOFC anode is strongly dependent on oxygen transport by the electrolyte [4, 5]. By examining the reactivity of the catalyst at different oxygen levels, this approach provides insight into the relation between oxygen concentration and carbon formation.

The oxidation of methane was performed at 800, 700, 600, and 500 °C for 8 catalysts; therefore, a total of 32 data was obtained. A temperature of 800 °C is a typical SOFC operating temperature, while the low temperatures were examined to study the activity and carbon deposition at additional reaction conditions. Indeed, Murray et al. [6] previously indicated that low operating temperature is another factor to suppress carbon formation.

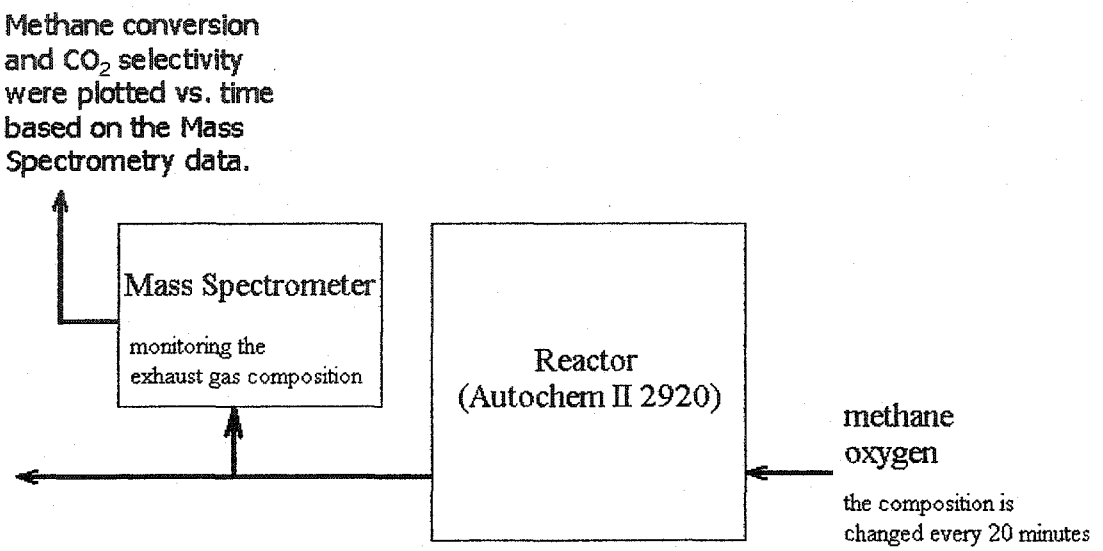

Figure 3-4. Schematic of the experiment for the reaction test of each catalyst.

Time (min)	Flow rate of 25% CH_4 (ml/min)	Flow rate of 10% O_2 (ml/min)	Composition of CH_4 : O_2 in the stream (molar ratio)	Lable
0-20	10	50	1 : 2	A
20-40	30	30	5 : 2	B
40-60	50	10	25 : 2	C
60-80	30	30	5 : 2	D
80-100	10	50	1 : 2	E

Table 3-4. Flow rates and the composition of inlet gases of the reactor.

The M200ED mass spectrometer yields mass spectrometry data in terms of partial pressures (inside the analysis vacuum chamber) versus the mass-to-charge ratio of each component (Figure 3-5). The peak-height-ratios between parent molecules and their fragments were experimentally determined by analyzing each gas without any reactions. These ratios are listed in Table 3-5. For convoluted peaks, the intensity of the various fragments were subtracted from the total peak intensity. For example, CO_2 (parent molecules appear as CO_2^+ in the mass spectrometer) has a principle mass-to-charge ratio of 44, and has fragments at 28, 16, and 12. The peak-height-ratios of those fragments relative to their parent molecules are 0.10, 0.10, and 0.09, respectively. At a mass-to-charge ratio of 16, there is an overlap between the CH_4 parent molecule and the CO_2 fragment. Thus, the product of the peak for the parent molecule of CO_2 and the corresponding peak-height ratio was subtracted from the peak height of the CH_4 parent molecule. The fragments of CO were not investigated since its fragment shows a negligibly small peak [7] and the effect on the calculation is expected to be very small.

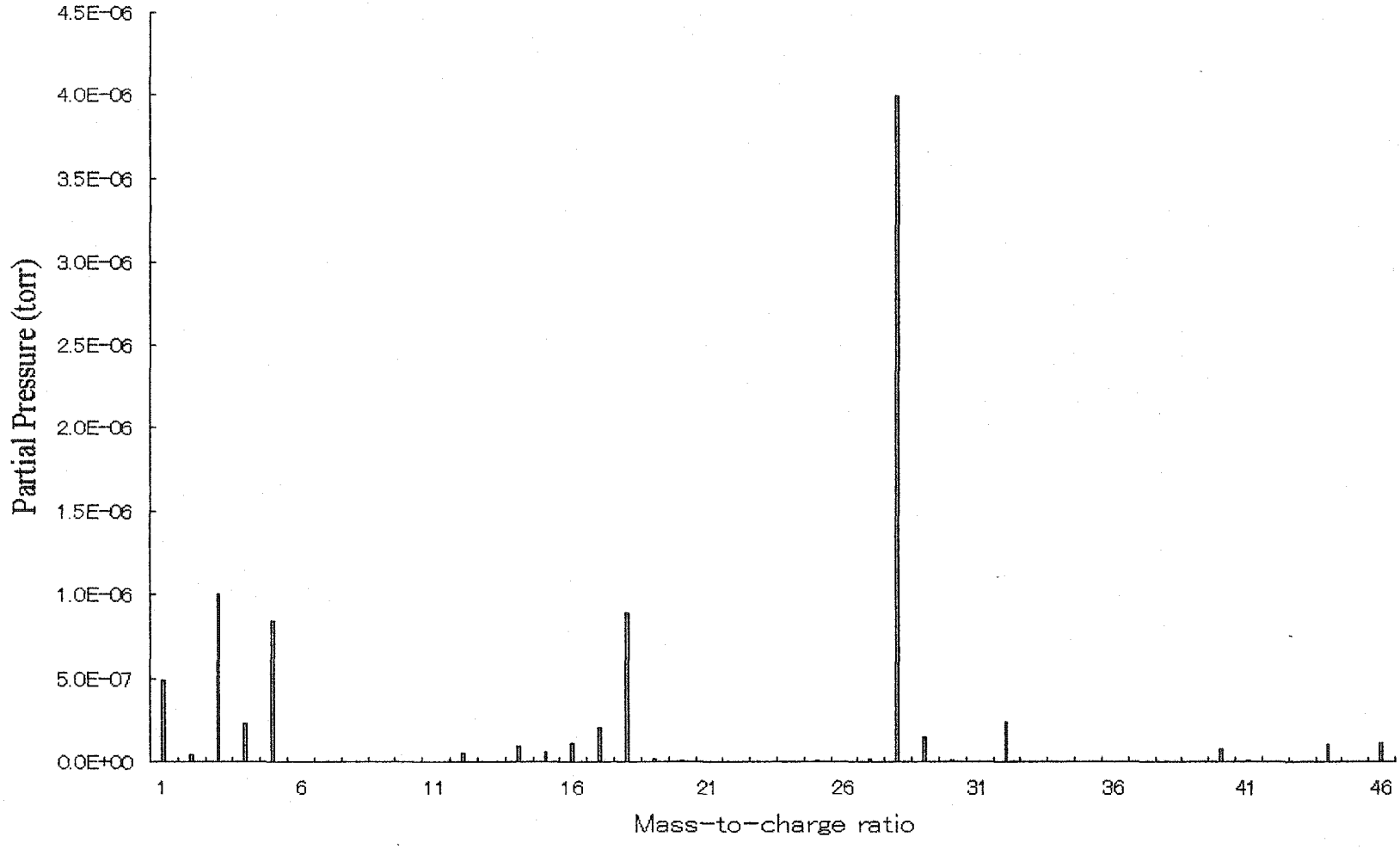

Figure 3-5. Sample spectrum obtained from M200ED

Based on the collected mass spectrometry data, the conversion of methane and the selectivity of CO_2 production were calculated by equations (3-6) through (3-10).

$$X_{CH_4} = \frac{[CH_4]_{inlet} - [CH_4]_{outlet}}{[CH_4]_{inlet}} \tag{3-6}$$

$$[CH_4]_{inlet} - [CH_4]_{outlet} \approx ([CO_2] + [CO])_{outlet} \tag{3-7}$$

$$[CH_4]_{inlet} \approx ([CH_4] + [CO_2] + [CO])_{outlet} \tag{3-8}$$

$$\therefore X_{CH_4} \approx \left(\frac{[CO_2] + [CO]}{[CH_4] + [CO_2] + [CO]} \right)_{outlet} = \left(\frac{P_{CO_2} + P_{CO}}{P_{CH_4} + P_{CO_2} + P_{CO}} \right)_{outlet} \tag{3-9}$$

$$Y_{CO_2} = \left(\frac{[CO_2]}{[CO_2] + [CO]} \right)_{outlet} = \left(\frac{P_{CO_2}}{P_{CO_2} + P_{CO}} \right)_{outlet} \tag{3-10}$$

where X, Y and P_i represent methane conversion, CO_2 selectivity and partial pressure of component i, respectively. Methane conversion was determined with equation (3-9), and CO_2 selectivity was calculated based on equation (3-10). As indicated by equation (3-8), the net amount of inlet methane should be approximately equal to the summed amount of outlet methane, carbon dioxide and carbon monoxide. Similarly, the amount of

reacted methane is equal to the amount of carbon monoxide and carbon dioxide at the outlet, as indicated by equation (3-7). Substituting (3-7) and (3-8) into equation (3-6) gives equation (3-9). In this calculation, it was assumed that the only outlet components with carbon were carbon dioxide, carbon monoxide, and methane. It was also assumed that the amount of carbon deposited on the catalyst is negligible. The latter is not necessarily a good assumption since a significant amount of carbon deposition is possible at this stage. Therefore, the methane conversions at unsteady state may not be very accurate. However, at steady state, the rate of carbon deposition may be neglected, and thus this calculation becomes more accurate. To analyze the transient state more accurately, the real time carbon deposition rate should be monitored. This was not done in the present study due to equipment limitations.

Component Formulae	Mass-to-charge ratio of parent molecule	Mass-to-charge ratio of primary fragments	Peak-height ratio (fragment/parent)
O_2	32	16	0.08
CH_4	16	15, 14, 13, 12	0.81, 0.08, 0.04, 0.01 respectively
CO_2	44	28, 16, 12	0.10, 0.10, 0.09 respectively

Table 3-5. Calibrated fragments and their peak height ratios.

3.6 Rate of Reaction and Equilibrium Constants

For each catalyst, the average methane conversion in each period was calculated and the data were fit using a power law and Arrhenius relation as follows:

$$(-r_{CH_4}) = kC_{CH_4}^{\alpha} C_{O_2}^{\beta} = \left[A\exp\left(-\frac{E_a}{RT}\right)\right] C_{CH_4,ave}^{\alpha} C_{O_2,ave}^{\beta} \qquad (3\text{-}11)$$

where $(-r_{CH4})$ is the rate of disappearance of methane during the experiment. k is rate constant of the reaction, C_i represent the average concentration of the component i at the inlet and the outlet, and A and E_a are the pre-exponential factor and activation energy, respectively. The concentrations used are the average of the inlet and outlet concentration. The rate of methane disappearance $(-r_{CH4})$ is determined from the following equation:

$$(-r_{CH_4}) = \frac{F_{CH_4 0} X_{CH_4,out}}{N_{metal}} \qquad (3\text{-}12)$$

where F_{CH4} is the inlet molar flowrate of methane and N_{metal} is the experimentally metal loading (molar) of metals present on each catalyst. The four parameters, A, E_a, α, and β were determined by Polymath (version 5) developed by Shacham, Cutlip and Elly [8].

This approach enables the visualization of the dependence of $-r_{CH4}$ on methane and oxygen concentration, and further allows the determination of the activation energy, E_a, of each catalytic reaction.

The equilibrium constant K was also calculated for the reactions (3-13) and (3-14) using HSC Chemistry 4.0 provided by Outokumpu [9]. The calculated temperature interval was between 25 and 1000 °C. The equilibrium constant K is determined by equation (3-15).

$$CH_4 + 2O_2 \leftrightarrow CO_2 + 2H_2O \quad (3\text{-}13)$$

$$CH_4 + \tfrac{3}{2}O_2 \leftrightarrow CO + 2H_2O \quad (3\text{-}14)$$

$$K = \prod (P_i)^{v_i} \quad (3\text{-}15)$$

This equilibrium constant, K, allows one to determine whether the observed conversion is thermodynamically of kinetically limited. If the reaction is not reaching equilibrium, then improvements in the catalysts or reaction conditions are possible.

References

[1] Operation Manual of Autochem II 2920 provided by Micromeritics.

[2] *Physical Chemistry;* Sixth edition, Gordon M. Barrow, McGraw Hill

[3] http://www.lasurface.com/ (viewed on July 12 2004)

[4] T. Horita, K. Yamaji, N. Sakai, Y. Xiong,T. Kato, H. Yokokawa, T. Kawada, *Journal of Power Sources,* Vol. 106, 2002, 224.

[5] C. A. J. Fisher and H. Matsubara, *Journal of the European Ceramic Society,* Vol. 19, 1999, 703.

[6] E. P. Murray, T. Tsai, S. A. Barnett, *Nature*, Vol. 400, 1999, 649.

[7] http://webbook.nist.gov/chemistry/ (viewed on July 13 2004)

[8] http://www.polymath-software.com (viewed on July 13 2004)

[9] http://www.outokumpu.com/pages/Page____8109.aspx (viewed on July 13 2004)

Chapter 4

Experimental Results

4.1 BET Surface Area Measurement

Table 4-1 shows the results for the BET surface area measurement of each catalyst. As stated in the previous chapter, two experiments were run for each catalyst to confirm repeatability. All errors fall within ± 5%.

The Cu/8YSZ, Co/8YSZ, Cu/CeO_2/8YSZ, Co/CeO_2/8YSZ, and Ag/8YSZ have very small surface areas, while Ni/8YSZ, Ni/CeO_2/8YSZ, and Ag/CeO_2/8YSZ have large surface areas. Ag/CeO_2/8YSZ has about the double surface area compared to Ag/8YSZ; however, this increase of surface area is not seen in other catalysts. It should be noted that silver has double the molecular weight than the other metals. Therefore, it is expected that silver may increase the mass of the catalyst more significantly compared with other metals. This leads to the lower surface area per unit mass. However, the result was quite different; silver had a higher surface area than copper or silver catalysts.

	Experiment 1 (m^2/g)	Experiment 2 (m^2/g)	% error of Experiment 2	Average (m^2/g)
8YSZ	14.10	14.46	2.6%	14.28
Ni/8YSZ	6.92	6.92	-0.1%	6.92
Cu/8YSZ	2.96	2.88	-2.6%	2.92
Co/8YSZ	3.51	3.44	-1.9%	3.47
Ag/8YSZ	4.03	4.14	2.6%	4.09
Ni/CeO_2/8YSZ	8.39	8.00	-4.6%	8.20
Cu/CeO_2/8YSZ	2.55	2.47	-3.3%	2.51
Co/CeO_2/8YSZ	4.39	4.32	-1.9%	4.35
Ag/CeO_2/8YSZ	7.89	7.79	-1.3%	7.84

Table 4-1. Results for BET surface area measurement for each catalyst.

4.2 Metal Loadings Determined by XPS

The concentrations of each metal and CeO_2 in each catalyst were determined by x-ray photoelectron spectroscopy (XPS), and the results are summarized in Table 4-2. All of the samples, with the exception of Ni/8YSZ and Cu/8YSZ, had significantly lower loadings than the target loadings (20 mol% metal, 10 mol% CeO_2). Co/8YSZ, Co/CeO_2/8YSZ and Ag/CeO_2/8YSZ have less than half of the targeted metal loading. In contrast with other

metals, the loadings of cerium were all greater than the targeted values except for $Cu/CeO_2/8YSZ$. $Ag/CeO_2/8YSZ$ had 31.8 mol % loading of cerium in the catalyst where the target is only 10 mol %. Theoretically, all of the catalysts were prepared from identical $CeO_2/8YSZ$; therefore, the maximum theoretical mol% of CeO_2 on $M/CeO_2/8YSZ$ must be equal to the observed CeO_2 loading on $CeO_2/8YSZ$ which is 20.6 mol%. However, on $Ag/CeO_2/8YSZ$, the loading of CeO_2 had exceeded that maximum theoretical value.

4.3 Reaction Tests on the Catalysts

4.3.1 Methane Conversions

For eight different catalysts at four different temperatures, the reaction of methane and oxygen was performed at various compositions, which are labeled as periods A – E. The operating temperatures were 800, 700, 600, and 500 °C. The conversion of methane at steady state was focused on in this study. Figure 4-1 shows a result for Cu/8YSZ at 800 °C as an example. Average conversion values for each period were collected and are shown on Figures 4-2, 4-3, and 4-4. The conversion values are also listed for all periods in Table A-1 in Appendix A.

	Loadings of M on M/8YSZ or M/CeO_2/8YSZ	Target loadings of M on M/8YSZ (mol %)	Loadings of CeO_2 on M/CeO_2/8YSZ (mol%)	Target Loadings of CeO_2 on M/CeO_2/8YSZ
Ni/8YSZ	19.1	20.0	N/A	N/A
Cu/8YSZ	18.4	20.0	N/A	N/A
Co/8YSZ	7.6	20.0	N/A	N/A
Ag/8YSZ	13.4	20.0	N/A	N/A
CeO_2/8YSZ	20.6	12.5	N/A	N/A
Ni/CeO_2/8YSZ	13.1	20.0	23.0	10.0
Cu/CeO_2/8YSZ	16.7	20.0	10.4	10.0
Co/CeO_2/8YSZ	9.8	20.0	16.6	10.0
Ag/CeO_2/8YSZ	6.1	20.0	31.8	10.0

Table 4-2. Loadings of M and CeO_2 determined by the XPS technique.

It is clear from these figures that in an oxygen rich environment (period A), all of the catalysts demonstrated as high as about 90% methane conversion. About 40% conversion is achieved even at 500 °C for all catalysts. With decreasing oxygen concentration to about 30% (period B), several of the catalysts at several temperatures had significantly lower methane conversions. Indeed, copper- and silver- based catalysts demonstrated methane conversion of about 50%. Nickel- and cobalt-based catalysts maintained their high reactivity regardless of the decreasing oxygen supply. Co/8YSZ had also shown a significant conversion drop at 700 °C; however, this was recovered by doping with CeO_2. Co/8YSZ at 800 °C had the highest conversion increase by ceria-doping.

As seen in Figure 4-4 (period C), where the oxygen concentration is below 10 %, copper and silver based catalysts showed a very poor performance in which the conversion is approximately 35% at 800 °C and below 20% at 500 °C. Nickel based catalysts still show very high activities even at 600 °C, which demonstrated 45 to 65 % methane conversion. Co/8YSZ showed a significant decrease in conversion at all temperatures, while $Co/CeO_2/8YSZ$ maintained conversions above 80 % for 700 and 800 °C.

The CeO_2-doping effect is different from catalyst to catalyst. Figure 4-5 shows the methane conversion increase for each metal. It is apparent that cobalt has the largest impact while silver is only slightly affected. Copper and nickel are also significantly

affected by ceria-doping; however, copper is affected only at 700 °C and ceria had no effect at other temperatures.

Summarizing the conversions, nickel- and cobalt-based catalysts at high temperatures (700 – 800 °C) have optimal reactivity. Highly reactive catalysts produce high enthalpies of reactions and large portions of these are obtained as electrical power from an SOFC. Therefore nickel- and cobalt-based catalysts may be the optimal catalysts for an SOFC anode. However, as pointed out in the previous chapters, deactivation is the main concern on the SOFC anode and the tolerance of these catalysts against carbon formation needs to be examined. This is discussed in the following sections.

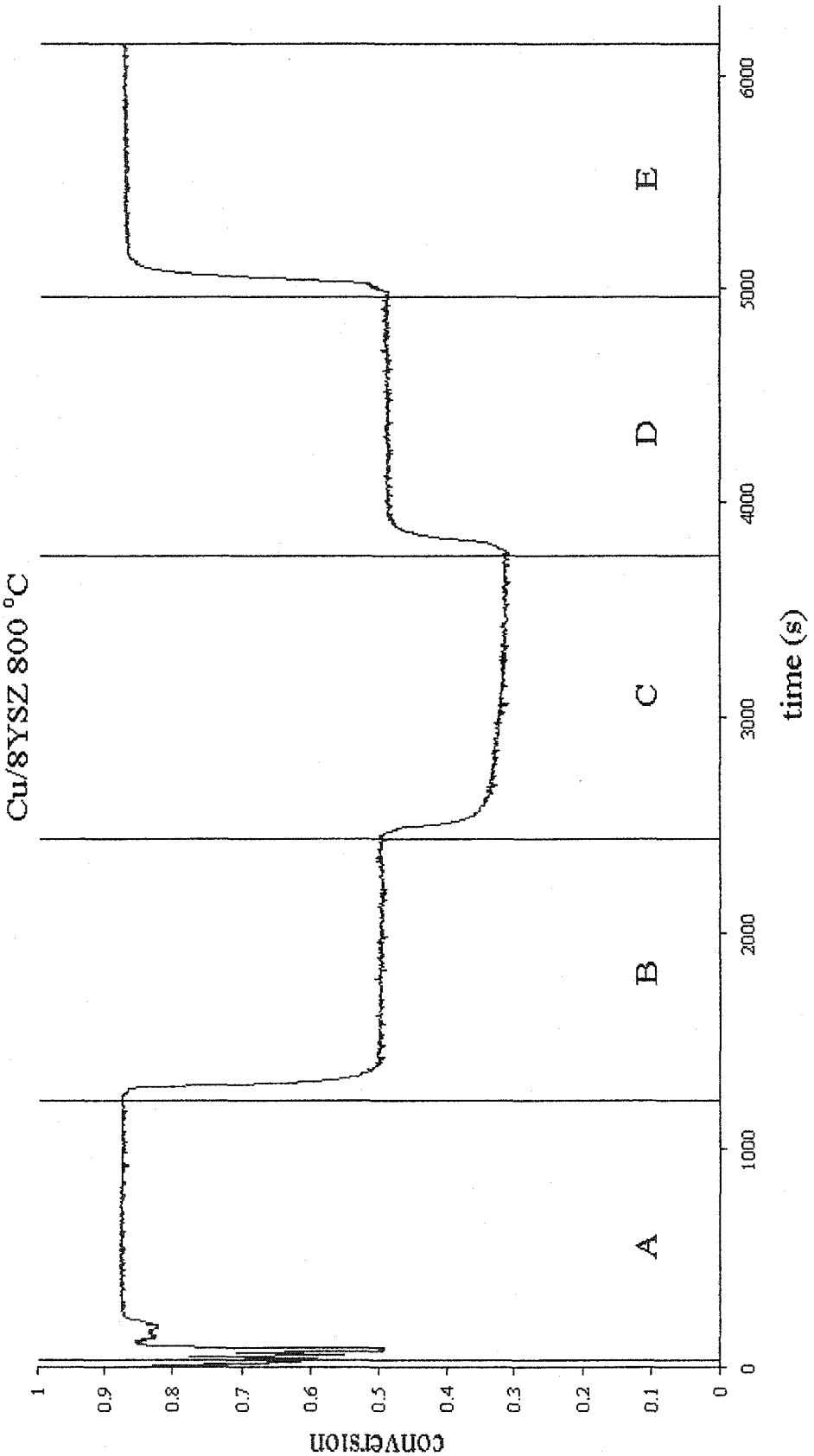

Figure 4-1. Methane conversion plot vs. time for Cu/8YSZ at 800 °C.

Periods A through E are defined in Table 3- 4.

Figure 4-2. Methane conversion in period A.

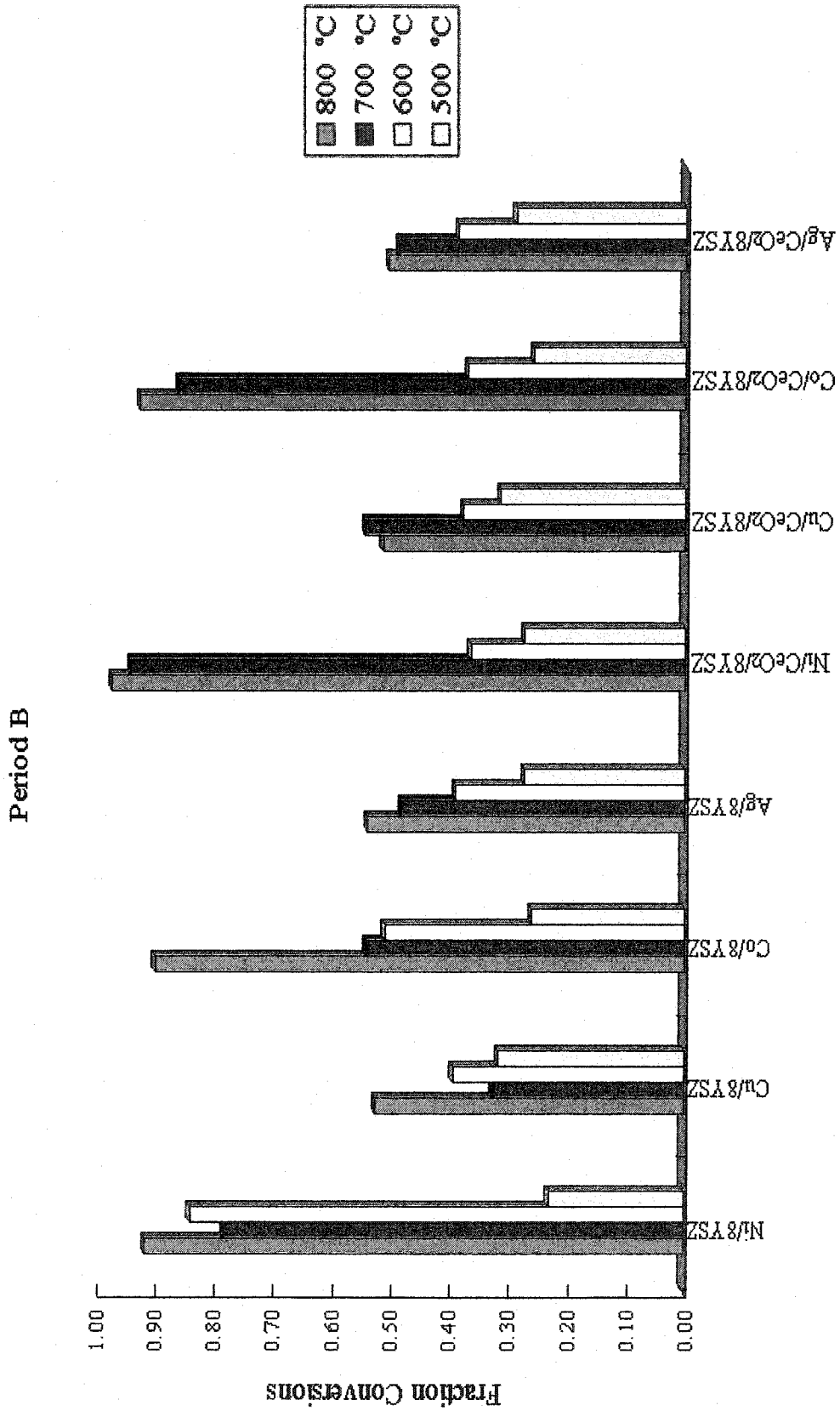

Figure 4-3. Methane conversion in period B.

Figure 4-4. Methane conversion in period C

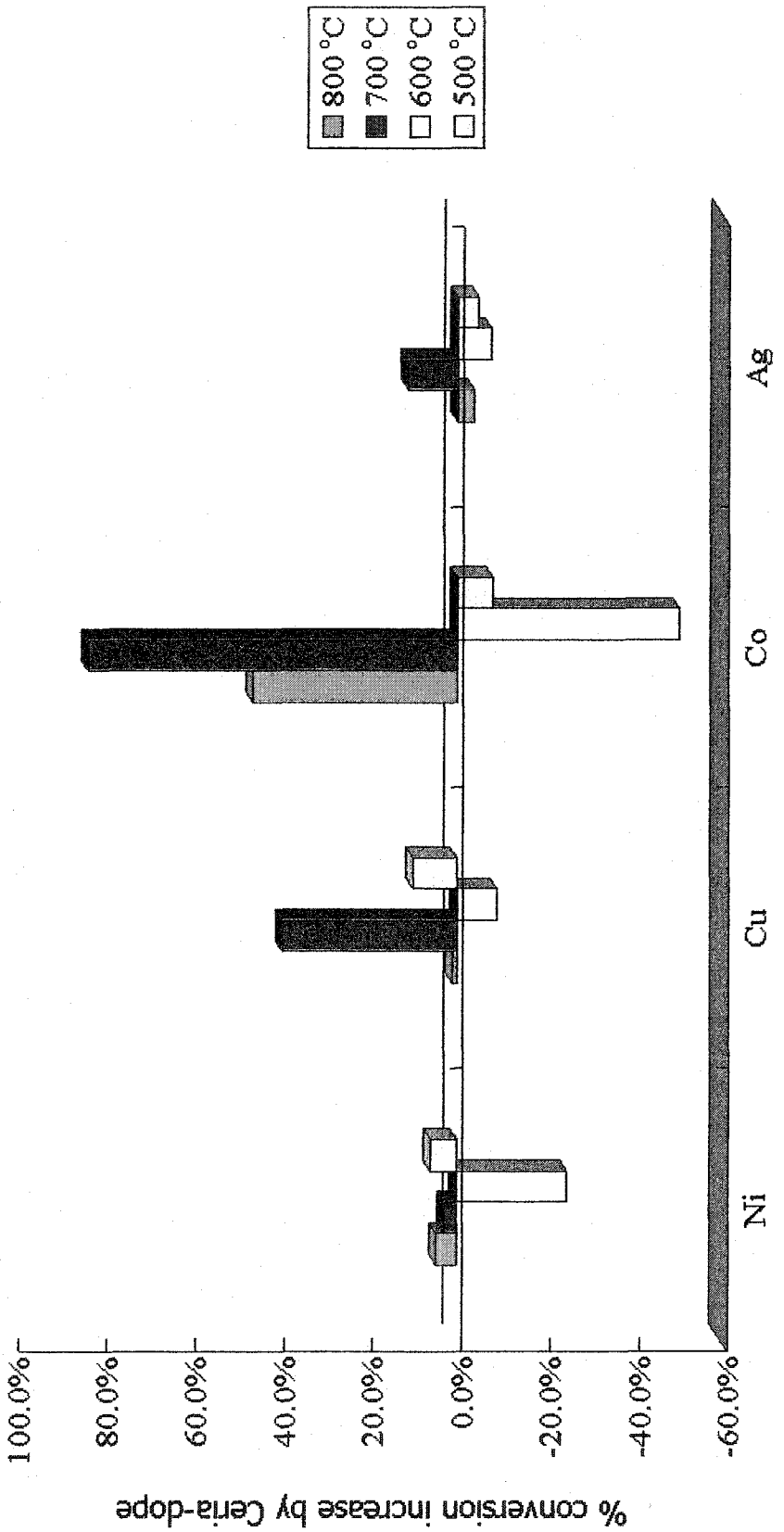

Figure 4-5. The percent methane conversion increase for each metal.

4.3.2 CO_2 Selectivity

CO_2 selectivity was determined by equation (3-8) and the values for each catalyst at different temperatures and inlet oxygen concentrations are summarized in Figures 4-6, 4-7 and 4-8. In period A, in which oxygen is sufficiently supplied, Cu/8YSZ tends to produce the highest CO_2 selectivity at 700, 600 and 500 °C. At 600 and 500 °C, Ag/8YSZ also demonstrated high CO_2 selectivity, and Ni/8YSZ has very high CO_2 selectivity at 700 °C. All of the metals showed high selectivity at 700 °C with CeO_2. In periods B and C, Ni/8YSZ and Ni/CeO_2/8YSZ at high temperatures showed a large decrease in selectivity. This trend is also seen on Co/8YSZ and Co/CeO_2/8YSZ at high temperatures; however, these two catalysts maintain high CO_2 selectivities at low temperatures. For all cases, copper- and silver-based catalysts are very stable even in an oxygen deficit environment and tend to complete the combustion.

CO is more unstable than CO_2, thus producing more CO than CO_2 may result in a higher chance of further surface reactions (reaction C-9, Appendix C). Therefore, CO_2 selectivity can be one of the measures for carbon formation. According to Figure 4-8, nickel-based catalysts at high temperatures do not produce CO_2 (or very little), while copper-based catalysts produced more CO_2 than nickel. This is consistent with the comparison of nickel and copper reported by Vohs et al. [2-7].

Figure 4-6. CO_2 selectivities of each catalysts at period A.

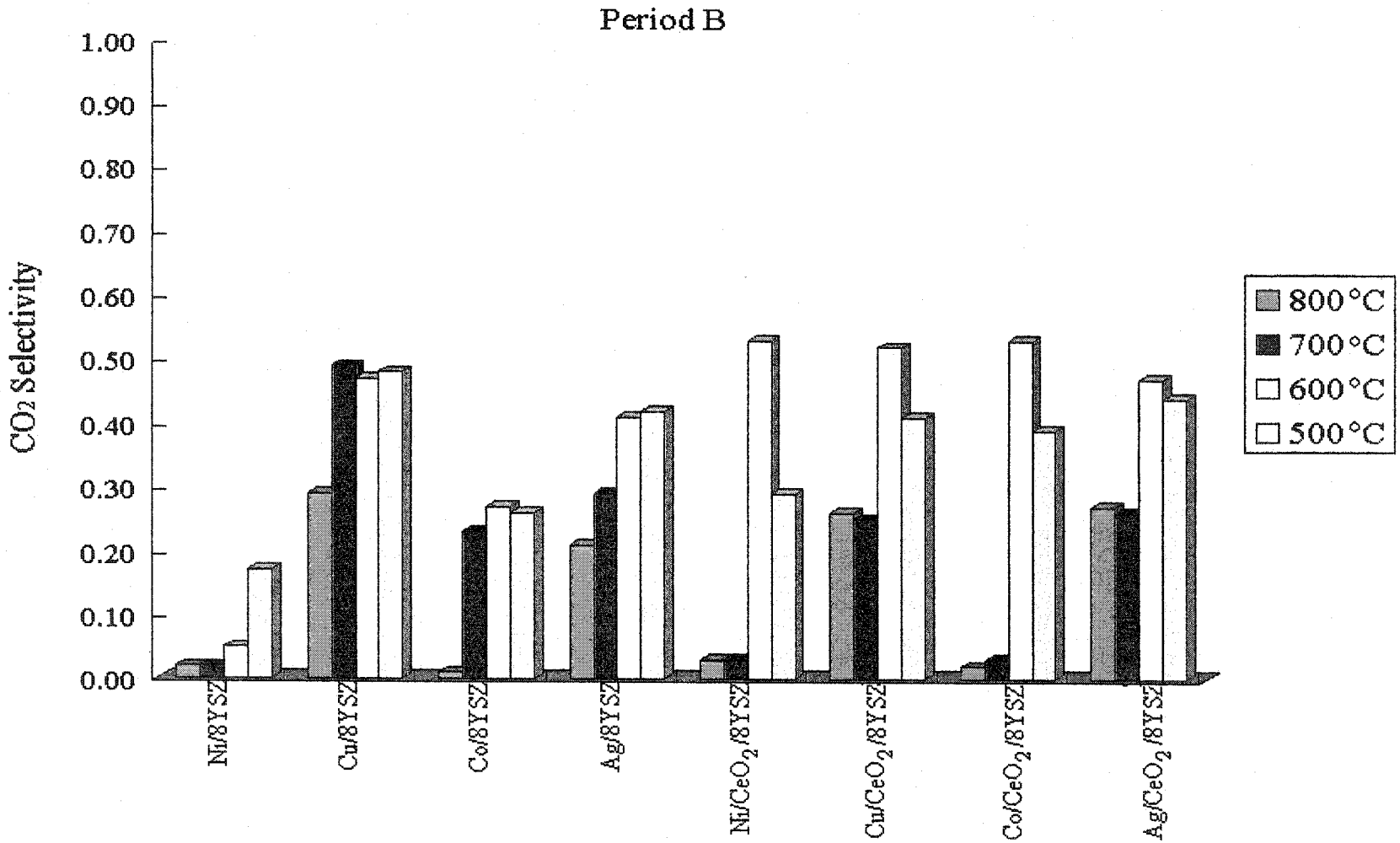

Figure 4-7. CO_2 selectivities of each catalysts at period B.

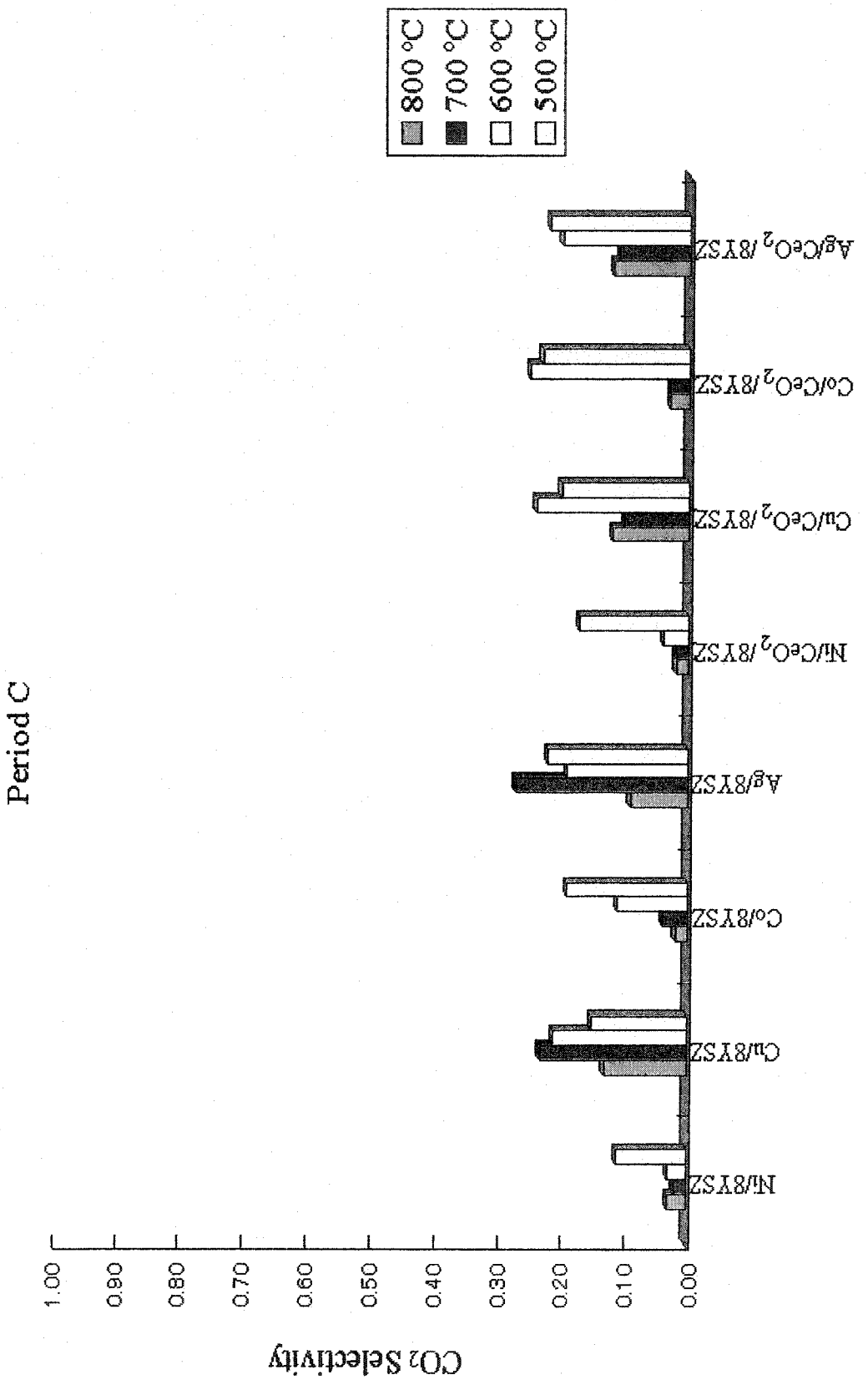

Figure 4-8. CO_2 selectivities of each catalyst at period C.

4.3.3 CO_2 selectivity change

Another parameter that has been studied in this research was the *CO_2 selectivity change*, as defined by equation (4-1).

$$Z = \frac{Y_E - Y_A}{Y_A} \tag{4-1}$$

If the catalysts have identical structures and surface compositions in periods A and E, the selectivity should be exactly the same. However, some catalysts showed a dramatic CO_2 selectivity decrease. Consequently, there must have been some change to the catalyst during period A – C, such that the CO_2 production is inhibited. As already discussed in the previous section, more CO production may have a higher chance of carbon formation; therefore, this dramatic CO_2 selectivity decrease is an indirect indication as to whether the catalyst is being deactivated.

Another point to note is the slight increase or decrease of CO_2 selectivity when the inlet oxygen concentration is changed, which is circled in Figures 4-9 and 4-10. On most of the catalysts, the CO_2 selectivity slightly jumps or drops for about 30 seconds when the oxygen inlet concentration is dropped. Several of the catalysts, for example Cu/8YSZ (Figure 4-9), had shown nearly equal values of CO_2 selectivity for periods A and E (i.e.

Z=0) while others like Ni/8YSZ (Figure 4-10) had shown a dramatic decrease in CO_2 selectivity. Z values were collected for all catalysts at each temperature and are summarized in Figure 4-11. According to Figure 4-11, Ni/8YSZ and Ni/CeO_2/8YSZ showed the largest Y (CO_2 selectivity) decrease over the widest temperature range (600 to 800 °C), while Cu/8YSZ, Cu/CeO_2/8YSZ, Ag/8YSZ and Ag/CeO_2/8YSZ had recovered nearly back to the initial Y value (i.e. Z=0). Co/8YSZ and Co/CeO_2/8YSZ have intermediate values in which the large Y decrease was seen at high temperatures while it was not seen below 600 to 700 °C. It should be pointed out that Co/CeO_2/8YSZ had shown a large CO_2 selectivity decrease at 700 °C, in contrast with Co/8YSZ which did not show any such tendency. It can be concluded that cobalt had experienced more severe deactivation by doping with ceria at this temperature. Copper- and silver-based catalysts are good candidates for the replacement with nickel-based catalysts on SOFC anodes, particularly when carbon deactivation is a concern. However, considering the poor reactivity of these catalysts (Figure 4-2 through 4-4 and Appendix A), they cannot be used and require modification to improve methane conversion. This is further discussed in Chapter 5.

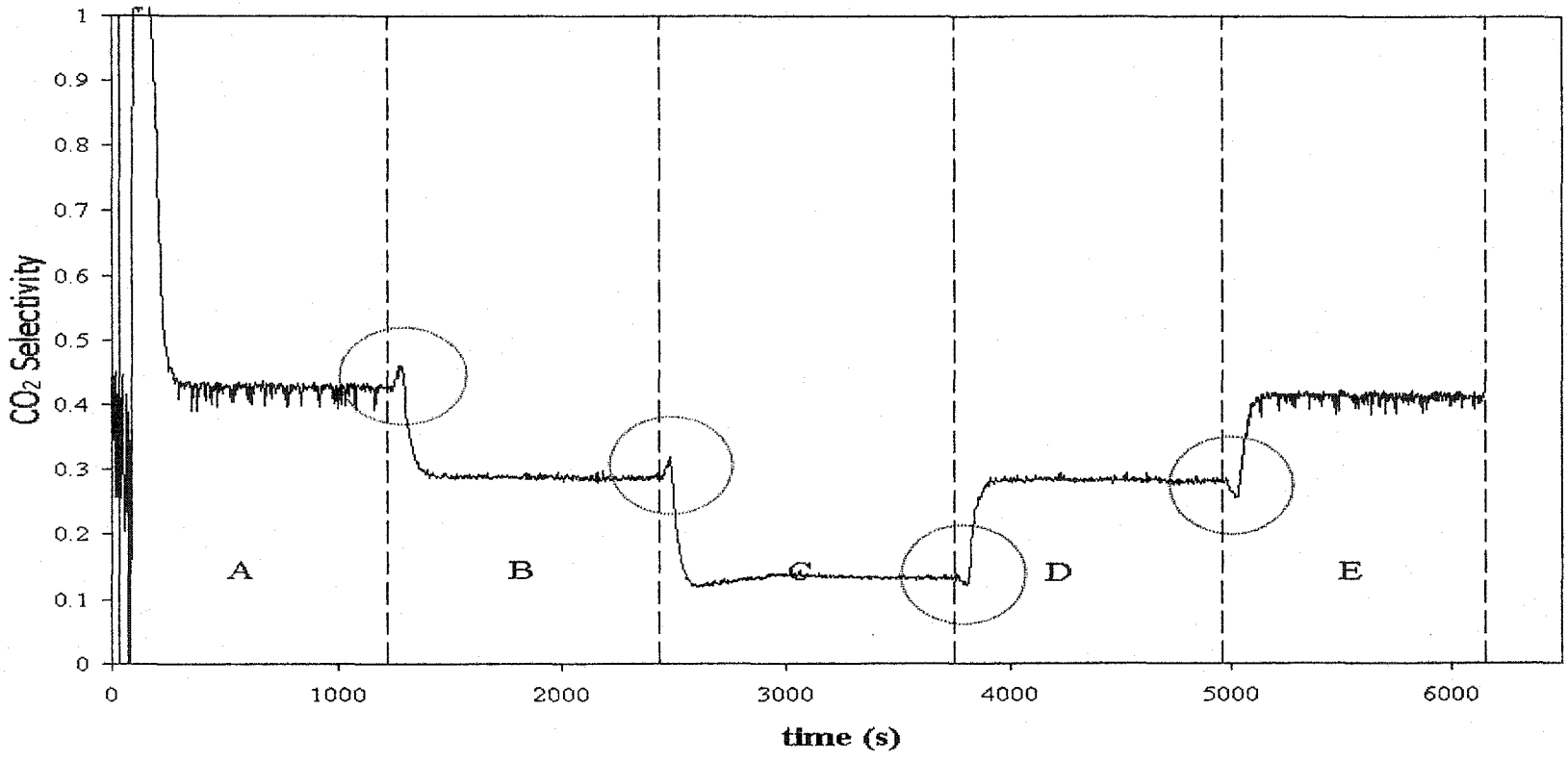

Figure 4-9. CO_2 selectivity vs. time on Cu/8YSZ at 800 °C. The light blue line represents the mole fraction of oxygen at the inlet. The slight increases and decreases in CO_2 selectivity are observed at every step change of O_2 concentration. The change is indicated by the circle on the Figure. Periods A through E are defined in Table 3- 4.

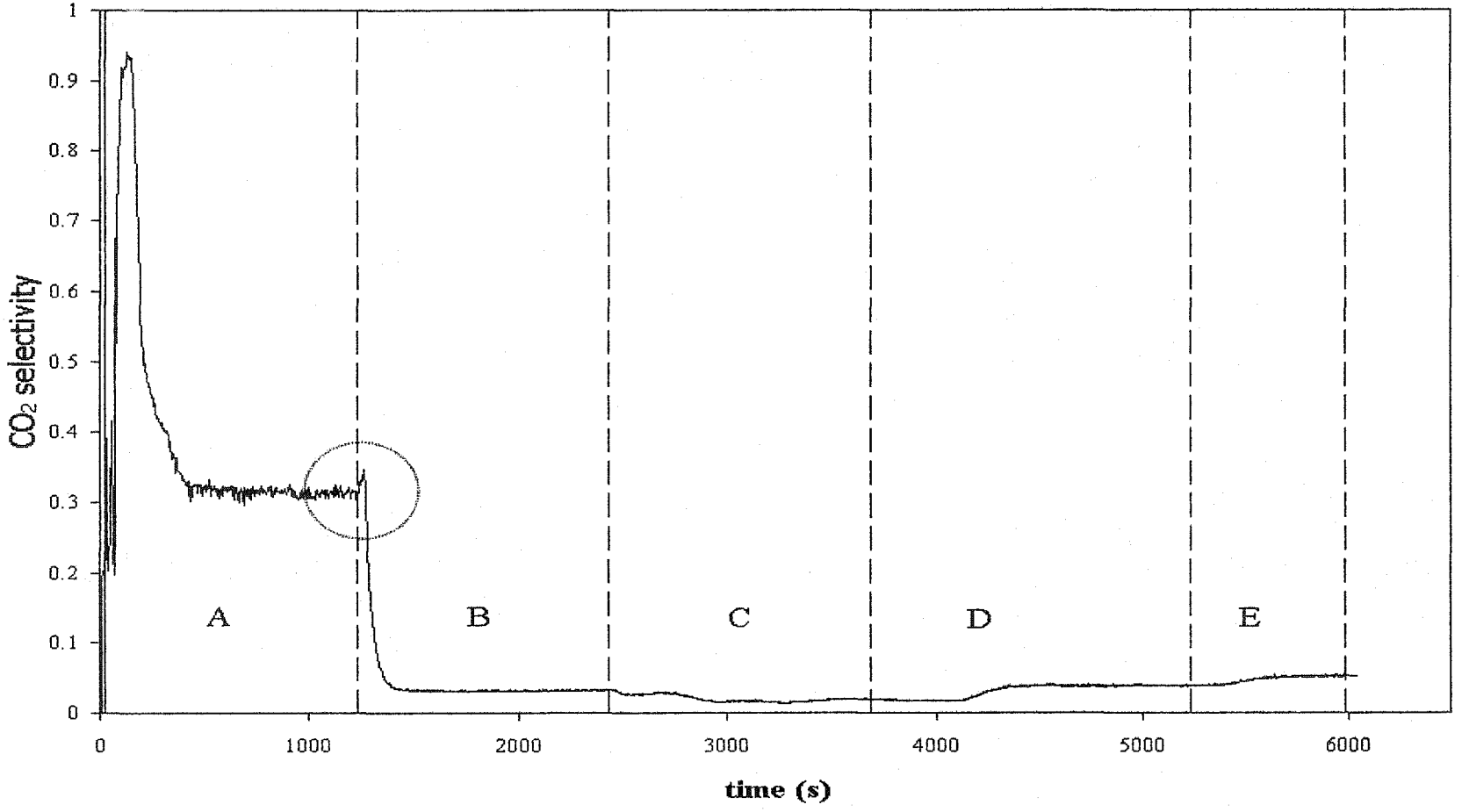

Figure 4-10. CO_2 selectivity vs. time on $Ni/CeO_2/8YSZ$ at 700 °C

Periods A through E are defined in Table 3- 4.

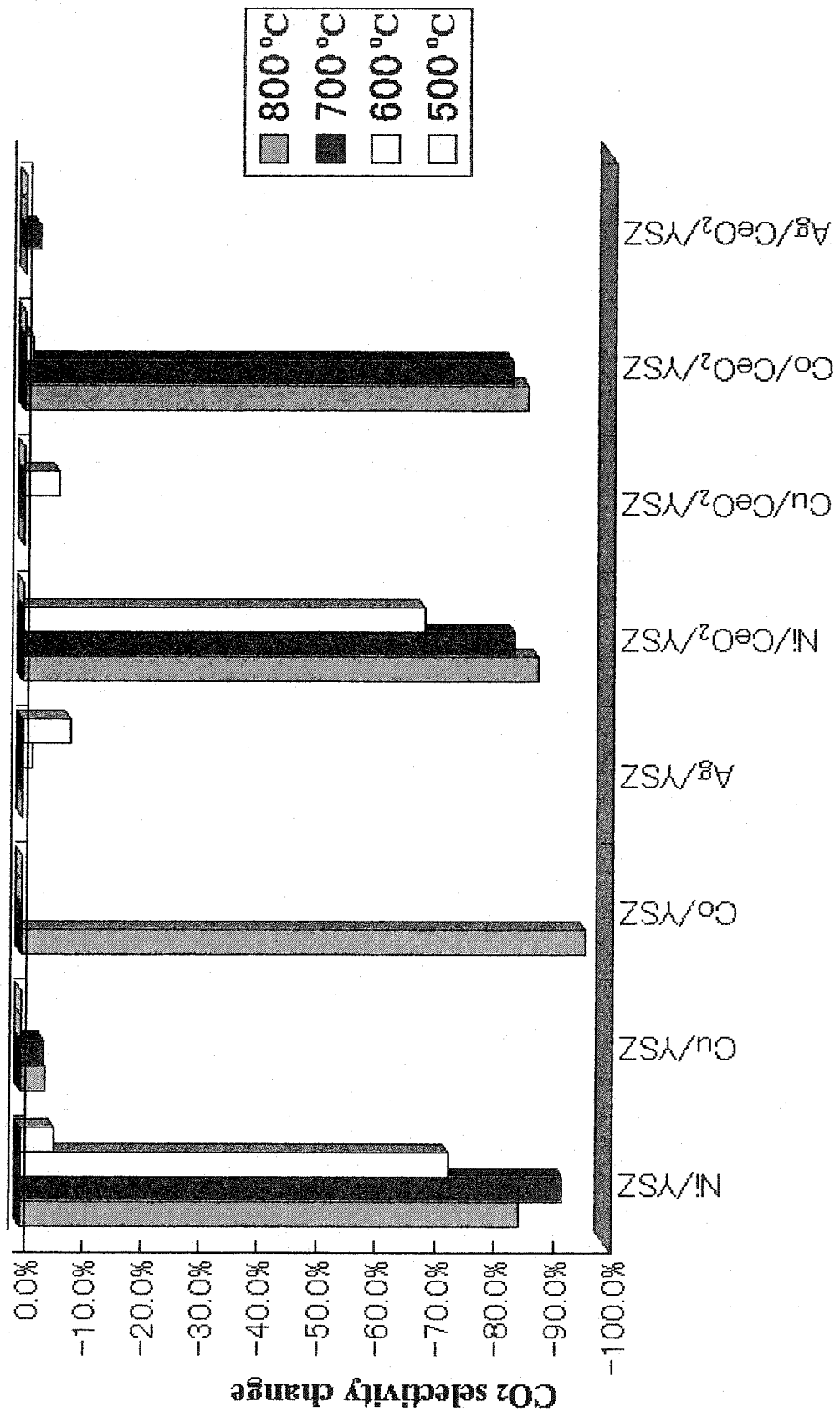

Figure 4-11. CO2 selectivity change values, Z, for each catalyst and temperature.

4.3.4 Partial Pressure Change

The mass spectrometer used in these experiments detects the partial pressures of each component in the exhaust gas mixture from the reactor. However, these partial pressures are characterizing the system in the vacuum chamber of the mass spectrometer; therefore, it is not possible to directly detect the pressure in the outlet stream of the reactor. The partial pressures in the vacuum chamber are proportional to the outlet partial pressures; thus, it is beneficial to consider the partial pressure difference of each component among all the catalysts. For instance, having an extremely low O_2 partial pressure on a certain catalyst implies that there was more oxygen uptake by the catalyst.

Figures 4-12 and 4-13 represent the average partial pressures of methane and oxygen in period C, respectively. The average partial pressures are determined by equation (4-2) and numerical integration.

$$\overline{P}_i = \frac{\int_1^2 P_i dt}{t_2 - t_1} \qquad (4\text{-}2)$$

From these figures, it is clear that Ni/8YSZ and Ni/CeO_2/8YSZ at both 800 and 700 °C have the largest methane uptake. Ni/8YSZ and NiCeO_2/8YSZ at 600 °C, Co/8YSZ and

$Co/CeO_2/8YSZ$ at 800 °C and $Co/CeO_2/8YSZ$ at 700 °C have intermediate methane uptakes. Different catalysts at other temperatures have very high outlet pressures. On the other hand, most of the catalysts had high oxygen uptake with the exception of Ni/8YSZ, $Ni/CeO_2/8YSZ$ and $Co/CeO_2/8YSZ$ at 800 °C and $Ni/CeO_2/8YSZ$ and $Co/CeO_2/8YSZ$ at 700 °C. Catalysts with ceria in the support have the highest or nearly the highest partial pressures at 700 °C.

4.4 Rate of Reaction

Data obtained for methane conversions and inlet gas concentrations were fit into equation (3-11). Table 4-3 lists the parameters determined. The high reactivity of nickel-based catalysts results from the high pre-exponential constant A, and α. Specifically, the value of A for $Ni/CeO_2/8YSZ$ is 500 to 1000 times higher than non-nickel catalysts. The activation energy is quite high for the nickel- and cobalt-based catalysts. This explains why conventional SOFCs have to operate at high temperatures. Additionally, nickel catalysts had negative β, implying that increasing oxygen supply decreases the reaction rate. This β is about double for $Co/CeO_2/8YSZ$ compared with Co/8YSZ implying that ceria doping has enhanced the dependency of cobalt on oxygen concentration.

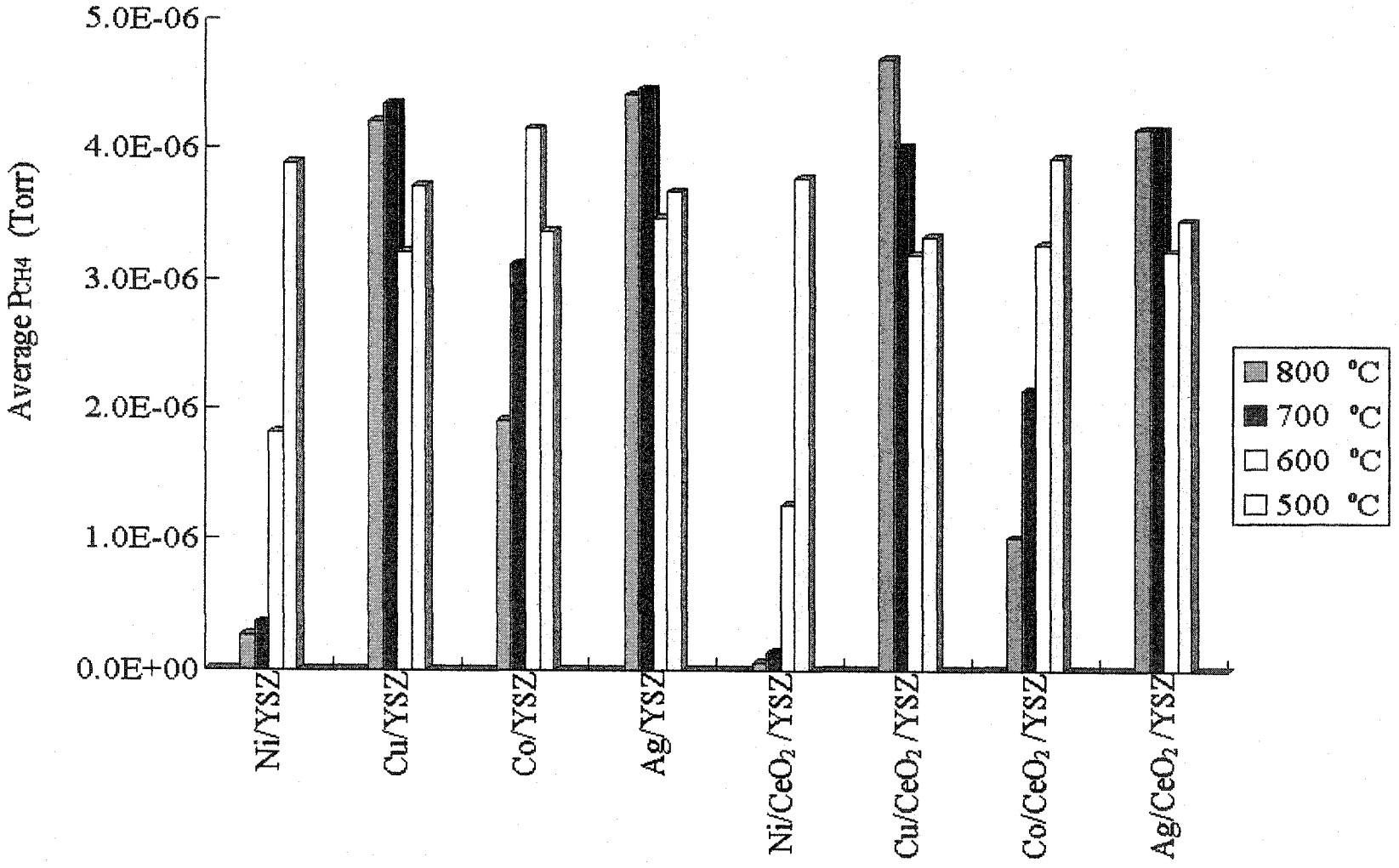

Figure 4-12. The average partial pressure of methane in period C determined by equation (4-3).

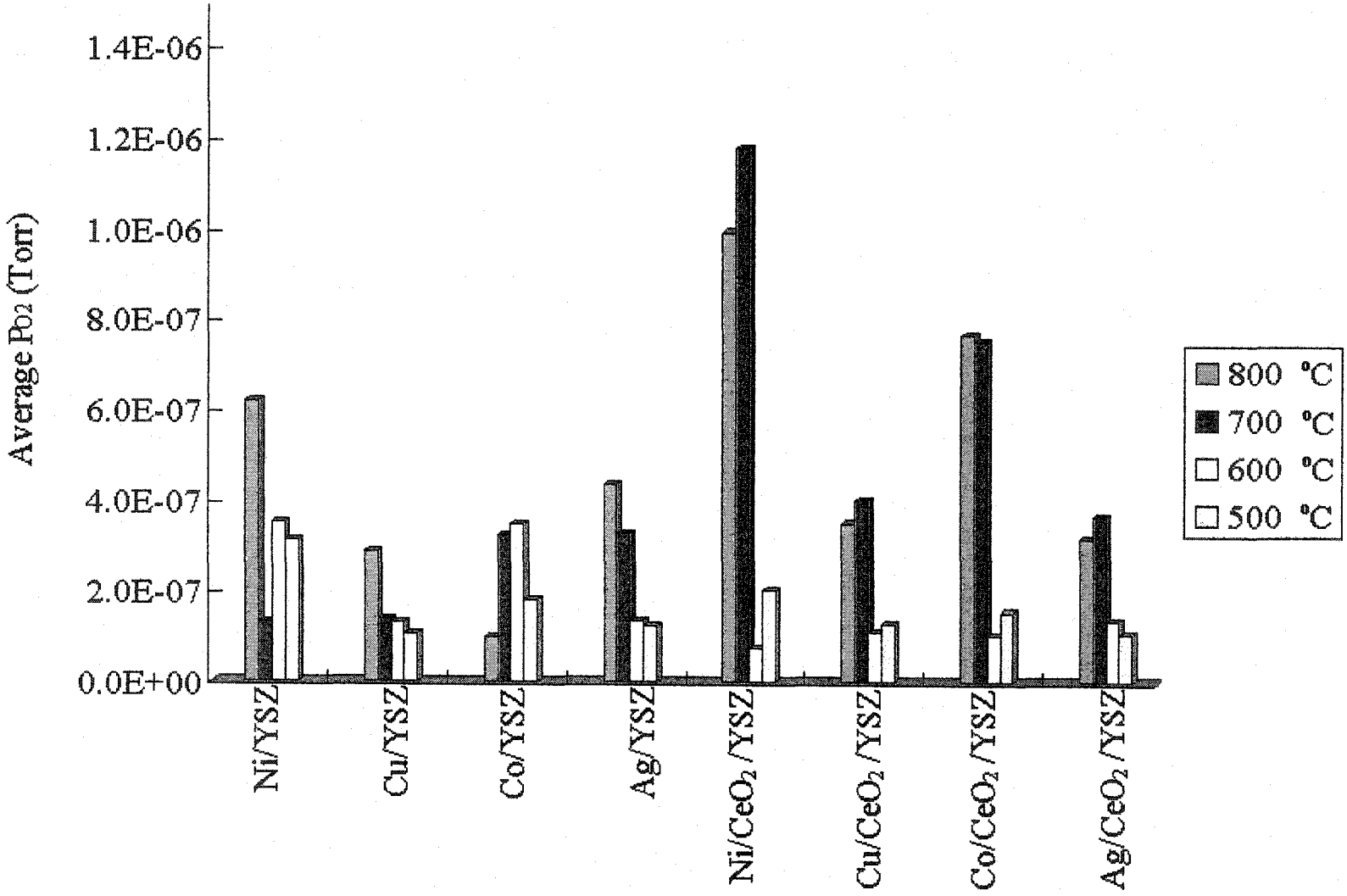

Figure 4-13. The average partial pressure of oxygen in period C determined by equation (4-3).

This trend is not seen on other catalysts. All catalysts, with the exception of silver, increased the dependence on methane concentration by doping with ceria. This is discussed further in Chapter 5. The plots of rate constant k vs. temperature for each catalyst are shown in Appendix A.

	Ea (kJ/mol CH_4)	A	α	β
Ni/YSZ	34.5	11.1	0.729	-0.263
Cu/YSZ	14.0	0.4	0.552	0.458
Co/YSZ	31.4	4.4	0.809	0.482
Ag/YSZ	18.8	1.0	0.518	0.334
Ni/CeO_2/YSZ	58.2	203.0	0.912	-0.324
Cu/CeO_2/YSZ	14.9	0.5	0.618	0.487
Co/CeO_2/YSZ	44.7	16.7	1.197	0.980
Ag/CeO_2/YSZ	16.5	0.8	0.518	0.323

Table 4-3. Parameters determined for equation (3-11). The negative β value is seen on nickel-based catalysts only. The β is dramatically higher for cobalt with ceria than without it. This β increase is not observed for other catalysts.

4.5 Equilibrium Constants

For each reaction, equations (3-13) and (3-14), the equilibrium constant was infinitely large in the calculated temperature interval. This implies that the reaction is irreversible and proceeds until the limiting reactant, methane or oxygen, is completely consumed. Therefore, it can be concluded that the reactions seen in this study are not reaching equilibrium although some catalysts like Ni/8YSZ and Ni/CeO_2/8YSZ were nearly at equilibrium. The plots of log$K$ versus temperature for the reactions, equation (3-13) and (3-14), are shown in Appendix B.

References

[1] C. Chen, W. Tuan, *Journal of the American Ceramic Society*; Vol. 83, 2000, 1693

[2] R. J. Gorte, J. M. Vohs, *Journal of Catalysis*, Vol. 216, 2003, 477

[3] S. Park, R. J. Gorte, J. M. Vohs, *Applied Catalysis A: General*, Vol. 200, 2000, 55

[4] R. J. Gorte, S. Park, J. M. Vohs, C. Wang, *Advanced Materials,* Vol. 19, 2000, 1465

[5] H. Kim, C. Lu, W. L. Worrell, J. M. Vohs, R. J. Gorte, *Journal of The Electrochemical Society*, Vol. 149, 2002, A247

[6] S. Park, J. M. Vohs, R. J. Gorte, *Nature*, Vol. 404, 2000, 265

[7] S. Park, R. Craciun, J. M. Vohs, R. J. Gorte, *Journal of The Electrochemical Society,* Vol. 146, 1999, 3603

Chapter 5

Discussion

5.1 CO_2, CO Production and Carbon Formation Rates

As discussed in the previous chapter, CO_2 selectivity and its dramatic decrease in an oxygen deficit environment are the signs of deactivation, possibly by carbon formation. There is no doubt that some type of change occurred on the catalysts that resulted in a decrease of CO_2 selectivity. However, comparing the methane conversion, i.e., the summed amounts of CO_2 and CO concentrations between periods A and E, or B and D (Appendix A), nickel and cobalt have shown significant increases for several temperatures. This suggests that CO_2 production is at least a two step reaction. More specifically, the two steps may be a CO production from CH_4 and subsequently CO_2 production from CO. The former is expressed by equations C-1, C-3, C-10 and C-12 and the latter by equations C-5, C-6, C-14 and C-15 in Appendix C. Under this assumption, it is possible that CO production is more dependent on methane concentration than oxygen concentration for nickel and cobalt, while copper and silver have less dependence on methane concentration. This results in higher α for nickel and cobalt in equation (3-11) and this is confirmed in Table 4-3. In contrast, CO_2 production is strongly dependent on

the oxygen concentration for all catalysts. This would explain why CO_2 production decreases more severely on nickel and cobalt than copper and silver (leading to CO_2 selectivity decrease) relative to the reacted methane.

Furthermore, oxygen adsorption (reaction C-2) reaches equilibrium much faster than methane adsorption (reaction C-1) on nickel- and cobalt based catalysts; therefore, methane adsorption is the rate limiting step. This would have stronger dependence on the methane concentration, whereas CO_2 production is much faster than oxygen adsorption and the rate determining step for this reaction is oxygen adsorption. For other catalysts, the rate of oxygen adsorption is similar; therefore, the rate of reaction strongly depends on both oxygen and methane concentration. It should be noted that "faster oxygen adsorption" does not necessarily mean "larger occupation of oxygen" than methane. If the desorption of the oxygen is also fast, it may reach equilibrium quickly; however, the occupation by oxygen could be small.

The reason why the CO_2 selectivity is not recovered for nickel and cobalt may be due to the fact that the number of C-M or CO-M bonds has dramatically increased with increasing methane concentration. This accelerates carbon formation on nickel and cobalt, as expressed by equations C-8, C-9, C-17, and C-18. As the occupation of sites by graphite grows, it deprives the catalyst of oxygen-adsorbing sites leading to an oxygen

deficit environment which strongly inhibits the CO_2 production step. When this graphite grows even further, the oxygen adsorbing sites decrease even more which inhibits CO production. Indeed, methane conversion is lower in period E than A at some temperatures even for nickel and cobalt. The reason for CO_2 production recovery on copper- and silver-based catalysts is that copper and silver have a far slower rate of graphite formation than nickel and cobalt. Adsorbed carbon and CO stays adsorbed without forming graphite and are desorbed when the oxygen supply is recovered. This is consistent with previous nickel and copper studies performed by Vohs et al. [1-6], in which both copper and nickel are coked when exposed to pure hydrocarbons, and copper is regenerated after it is exposed to air while nickel is not.

The slight increase and decrease of CO_2 selectivity at every step change (Figures 4-9 and 4-10) is another key fact that supports the two step reaction assumption. From period A through C, the methane concentration increases suddenly and CO production starts to increase. For the first 30 minutes after the step change of methane concentration, the catalyst has enough adsorbed oxygen to produce CO_2. However, the amount of CO is much larger than oxygen and, therefore, oxygen is quickly depleted and CO_2 production starts to decline. Indeed, this step change is not seen on the methane conversion plot (Figure 4-1).

5.2 Effect of CeO_2 Doping

As seen on Figure 4-5, the contribution of CeO_2 doping in the catalyst is different from catalyst to catalyst and temperature to temperature. In this work, it was found that CeO_2 had the largest contribution to Co/8YSZ, especially at 700 °C. The hypothesis is that this difference resulted from the different oxygen exchange potential, or the redox interactions between metal and CeO_2. Ceria provides oxygen to the surface of the metal by the following reversible reaction [7].

$$Ce_2O_3 + 0.5O_2 \leftrightarrow 2CeO_2 \qquad (5\text{-}1)$$

The active metal particles readily oxidize the carbon and hydrogen present on the catalyst surface; therefore, the metal particle itself is often in an electron abundant state. This electron is extracted by the ceria and the oxygen is extracted by the metal particle as a result. Therefore, the metal particle is oxidized back and repeats the oxidation of the carbon and hydrogen on the surface.

Another point to note is the reactivity of CeO_2 itself affects its interaction with hydrocarbons [7-9]. Ceria is a mixture of Ce^{IV} and Ce^{III}, which creates unsaturated oxygen at some sites (see Figure 5-1).

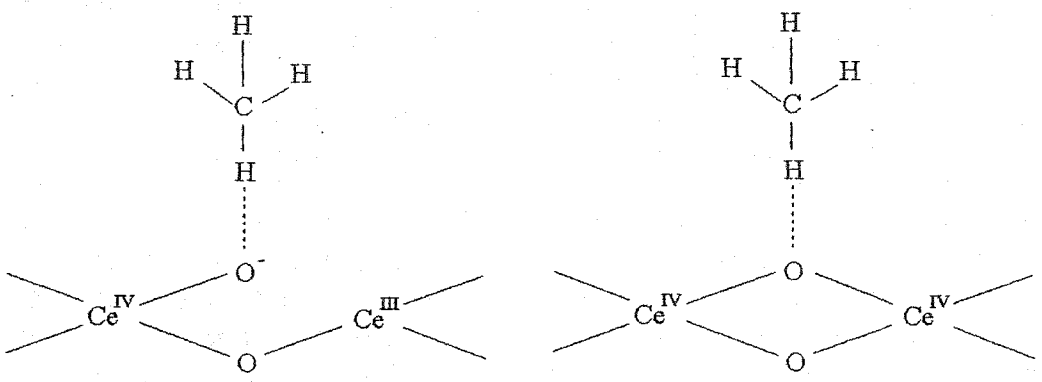

Figure 5-1. Schematics of unsaturated (a) and saturated (b) oxygen on cerium oxide. The figure was prepared based on reference [8].

This unsaturated oxygen is more active than saturated oxygen [8]; therefore, it accelerates methane adsorption and activation. Indeed, methane uptake is higher (lower partial pressures of methane) for most of the catalysts that had improved the conversion with ceria than ones that did not (Figure 4-12).

The redox interactions between the metal particles and ceria are possibly being reversed, depending on temperature. When this reverse interaction occurs, ceria extracts the oxygen and ceria itself becomes less active because of its saturated state. In addition, the metal

particle is deprived of oxygen on the surface, thus reducing the oxidation of carbon and hydrogen on the surface. This may be the reason why ceria results in lower conversion for some temperatures. The problem with copper and silver is that these metals have poor potentials for redox reactions. More specifically, silver is more inert than copper [10]. Therefore, these metals have less electronic interaction with ceria. That may be the reason why the impact of ceria doping is smaller than other two (Figure 4-5).

5.3 Calibrated and Target Metal Loadings

As stated in the previous chapters (Table 4-2), the calibrated metal loadings by XPS on some of the catalysts were significantly different from the targeted values. Most metals, especially silver and cobalt, were found to have smaller loadings than the target. Therefore, it is possible that some portion of the metal evaporated during calcinations. Indeed, the calcination temperature in this research was 950 °C which is approximately the melting point of silver (960 °C). At the melting point, the vapor pressure of silver dramatically increases (Figure 5-2) and a significant amount of silver possibly evaporated [11, 12]. Although the programmed calcination temperature was slightly below the melting point of the silver, it was possible that the furnace temperature was fluctuating within about ±10-15 °C from the programmed target temperature. In fact such behavior

was often seen for the furnace that was used. Therefore, it may seem that the low calibrated metal loadings by XPS are due to the metal evaporation.

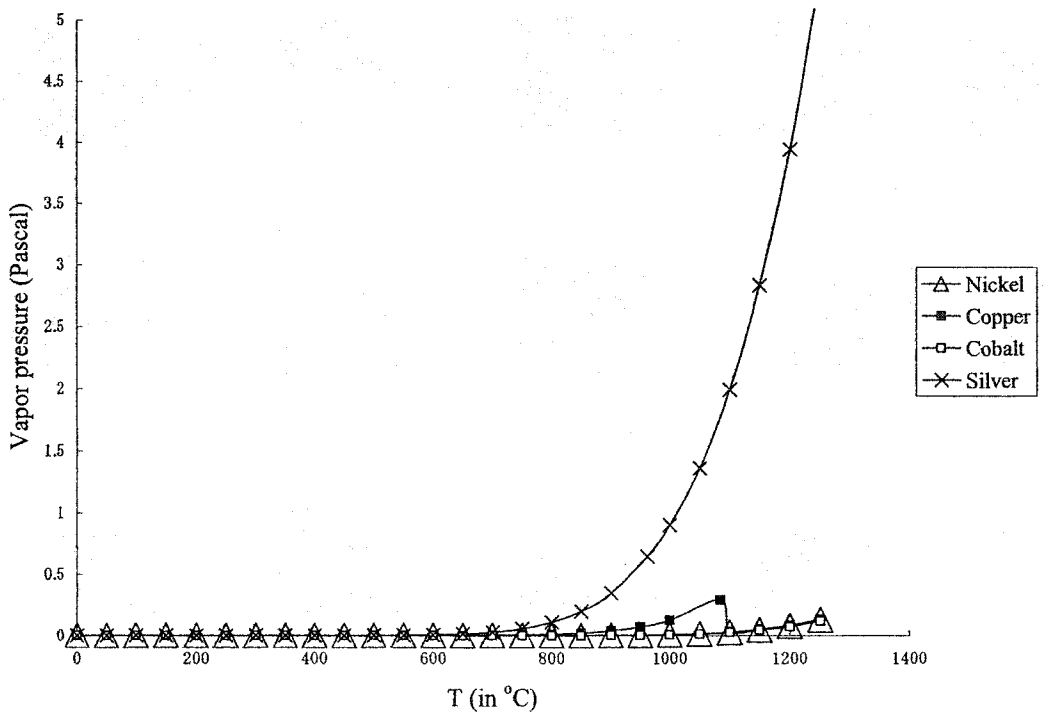

Figure 5-2. Vapor pressure vs. temperature.

The figure was prepared based on reference [11].

However, the vapor pressures of other metals are low above 1000 °C unlike silver (Figure 5-2). Copper shows a slight increase in vapor pressure and its calibrated metal loadings were also slightly smaller than the target; therefore, it could be assumed copper may have also evaporated during calcination. However, this contradicts the fact that

cobalt, which has far lower vapor pressure at the calcination temperature than silver, has a metal loading similarly small. Another question with the metal evaporation assumption is that the metal loadings for M/8YSZ and M/CeO_2/8YSZ are different for all metals. Under the metal evaporation assumption, the vapor pressures of the metal particles would be different between M/8YSZ and M/CeO_2/8YSZ which seems to be unlikely. The largest contradiction is that CeO_2 in CeO_2/8YSZ had significantly higher metal loadings than the target.

The possible reason for the different metal loadings detected by XPS may be related to the XPS surface sensitivity. The kinetic energy of photoelectrons from the atoms in the "bulk" is smaller than those at the "surface" because of energy loss due to its collision with other atoms [13]. Therefore, the kinetic energy detected by XPS is not accurately proportional to the number of the metal particles unless the metal is thin and well dispersed on the surface of the catalyst. In other words, some of the metal particles might be larger than others, perhaps because of sintering, and the total kinetic energy detected by XPS will be smaller than the case in which the metal particles form a thin layer on the support. Therefore, the number of metal atoms appearing on an XPS result is smaller than the actual number for metals that form large particles.

This is also consistent with cerium loading. The CeO_2 may have been thinly and widely

dispersed on the surface of the "large bulk" of 8YSZ (See Figure 5-3). With this assumption, the photoelectrons from CeO_2 can maintain kinetic energy because the particles are near the surface such that the electrons have little chance of collision with other molecules. Therefore, XPS can detect accurate kinetic energy from the cerium particles. In contrast, the photoelectrons from yttrium and zirconium atoms deep in the large bulk of 8YSZ must have experienced many more collision than ones that are near the surface. As a result the kinetic energy detected for 8YSZ becomes smaller; therefore, the atomic percent of CeO_2 appears greater than it actually is.

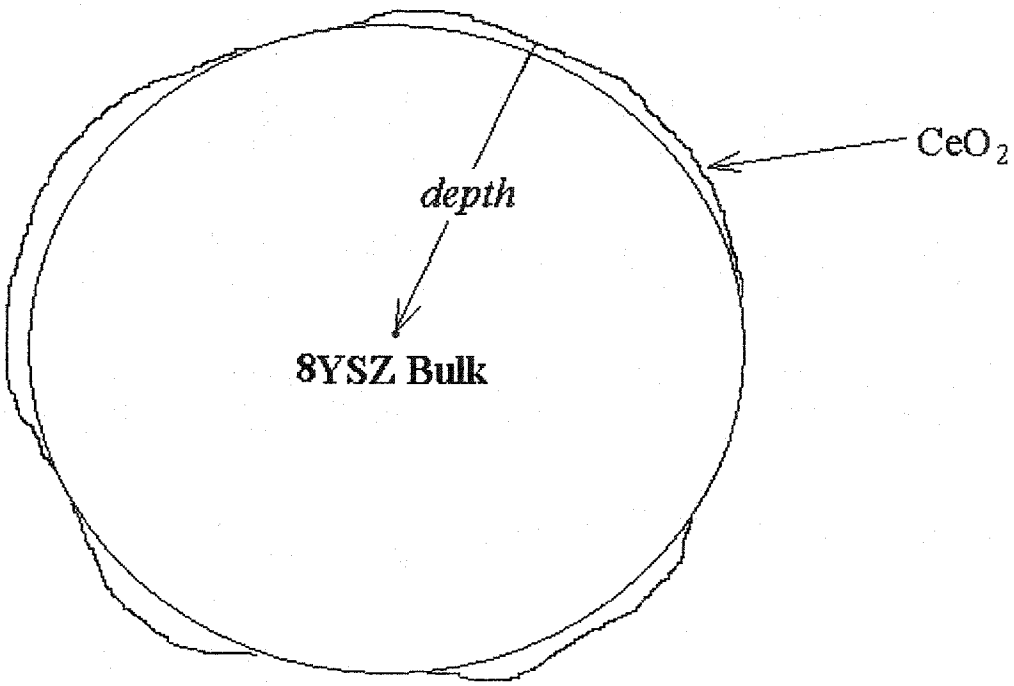

Figure 5-3. Possible schematic of CeO_2/8YSZ. CeO_2 form a thinly and widely dispersed layer on the "large bulk" of 8YSZ.

The BET surface area results are another key factor to be considered. As already stated in the previous chapter, well dispersed metals give a higher surface area than ones forming a large bulk on the catalyst support. The high surface area of nickel suggests its high dispersion on the support, and this is consistent with the XPS analysis. Cobalt is also consistent, as it had low surface area and low metal loading as determined by XPS. Therefore, it can be concluded that the bulk of metal particles were large. Silver had low metal loading by XPS and high surface area. This supports the conclusion that some

portion of silver evaporated. Copper had high metal loading by XPS and low surface area. Low surface area suggests that copper forms a large bulk, and the high metal loading determined by XPS suggests thinly dispersed metal on the support. This may be due to a number of "thin" Cu/8YSZ layers that are sintered together (See Figure 5-4). The sintered layers are still thin, such that all particles are near enough to the surface; therefore, XPS gives accurate atomic percent of each component. However, the Cu particles that had sintered two 8YSZ layers together are not open to the surrounding gases and thus are not detected by BET surface area measurement. This results in low surface area.

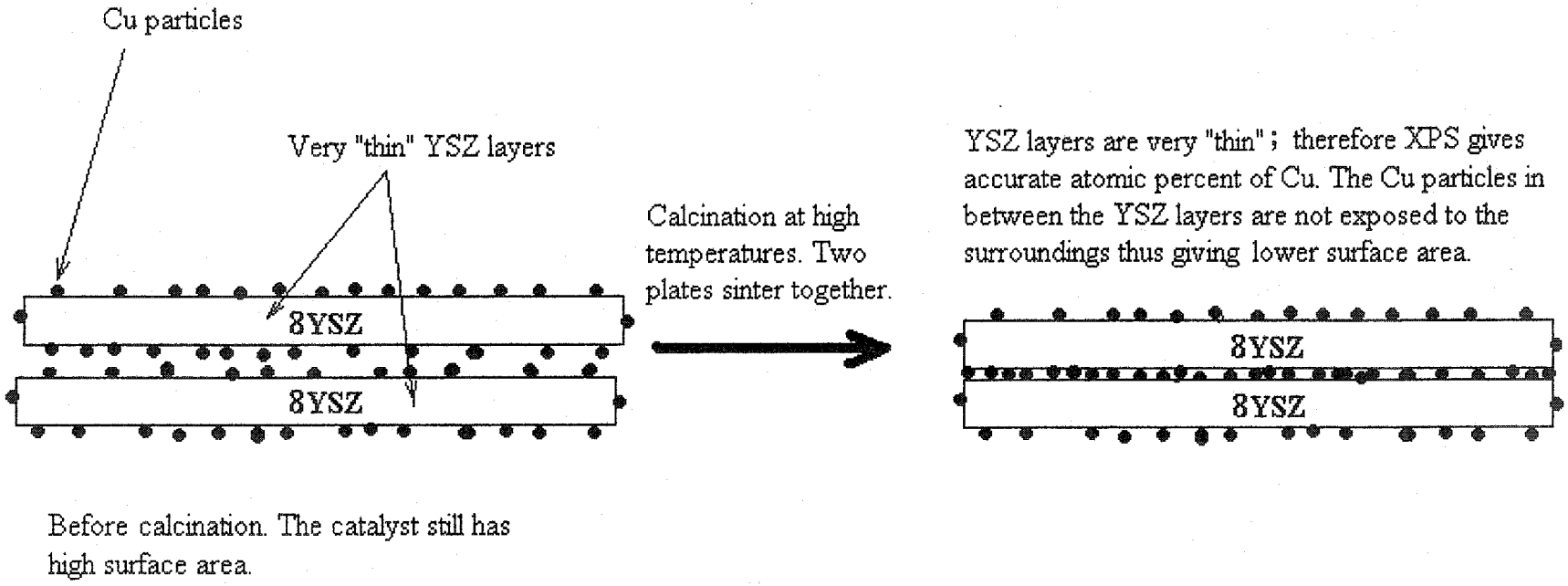

Figure 5-4. Schematic of sintered copper on 8YSZ.

References

[1] S. Park, R. Craciun, J. M. Vohs, R. J. Gorte, *Journal of The Electrochemical Society,* Vol. 146, 1999, 3603

[2] R. J. Gorte, J. M. Vohs, *Journal of Catalysis*, Vol. 216, 2003, 477

[3] S. Park, R. J. Gorte, J. M. Vohs, *Applied Catalysis A: General,* Vol. 200, 2000, 55

[4] R. J. Gorte, S. Park, J. M. Vohs, C. Wang, *Advanced Materials,* Vol. 19, 2000, 1465

[5] H. Kim, C. Lu, W. L. Worrell, J. M. Vohs, R. J. Gorte, *Journal of The Electrochemical Society*, Vol. 149, 2002, A247

[6] S. Park, J. M. Vohs, R. J. Gorte, *Nature*, Vol. 404, 2000, 265

[7] A. Trovarelli, *Catalysis Reviews Science and Engineering,* Vol. 38, 1996, 253

[8] C. Li, Q. Xin, X. Guo, *Catalysis Letter*, Vol. 12, 1992, 297,

[9] E. S. Putna, J. Stubenraunch, J. M. Vohs, R. J. Gorte, *Langmuir,* Vol. 11,1995, 4832

[10] D. F. Shriver, P. Atkins, C. H. Langford, *Inorganic Chemistry,* 2nd edition. W. H. Freeman and Company.

[11] CRC Handbook of Chemistry and Physics, 84th Edition, 2003-2004

[12] C. Chen W. Tuan, *Journal of the American Ceramic Society*; Vol. 83, 2000, 1693

[13] C. R. Brundle, C. A. Evans, Jr., S. Wilson, *Encyclopedia of Materials Characterization*, Boston: Butterworth-Heinemann; Greenwich, CT: Manning, 1992.

Chapter 6

Conclusions

As the kinetic model suggests, the rate of reaction is not improved by increasing the oxygen supply for the nickel catalysts. In addition, the activation energy is high for nickel; therefore, high temperature operation is required. On the other hand, other catalysts had higher dependence of reaction rate on the oxygen concentration, especially $Co/CeO_2/8YSZ$. Therefore, $Co/CeO_2/8YSZ$ can improve the rate of reaction the most. However, the high activation energy on $Co/CeO_2/8YSZ$ also necessitates high temperature operation. The ideal catalyst may be either copper or silver. Both of them give significantly high dependence of reaction rate on oxygen concentration and the activation energy is low. This suggests that replacing the nickel catalyst on the conventional SOFC anode with copper or silver enables low temperature operation of the SOFC which contributes to the further elimination of carbon formation. This also suggests that a higher oxygen supply to the SOFC anode with copper or silver will greatly improve its rate of reaction.

Although, copper and silver seem to perform similarly and both appear to be good candidates for the replacement of nickel on the SOFC anode, introduction of the copper

anode is more favorable than silver. The first reason is its lower cost since silver is one of the precious metals. The second one is that silver is not affected appreciably by CeO_2, which suggests that copper results in greater freedom to adjust the rate of reaction.

Although it is concluded that copper is a better SOCR anode candidate, it needs to be significantly improved for practical application. For example, the surface area should be increased to yield more active sites available for the reaction. As mentioned previously, copper experienced sintering because of its high calcination temperature. Therefore, the copper catalysts need to be prepared at lower calcination temperatures, as low as the expected operating temperature of the SOFC.

Chapter 7

Recommendations

While this work has provided valuable insight on the reactivity of model SOFC anode catalysts, it has also generated several additional questions. The significant metal loading difference of M between M/8YSZ and M/CeO_2/8YSZ is one example. Another example is excessively high CeO_2 atomic percent in Ag/CeO_2/8YSZ. The atomic percent of CeO_2 in CeO_2/8YSZ was far less than that in Ag/CeO_2/8YSZ. The largest question is why 8YSZ particles are "large bulk" for CeO_2/8YSZ and "thin layer" for copper. In addition, it is not even clear if metal evaporation had really occurred. To clarify all these remaining questions, different experiments and their comparison with the existing data are required. For example, repeating some experiments with the catalyst prepared at a lower calcination temperature and time. This should enable significant sintering to be eliminated. Thermogravimetric analysis [1] allows monitoring the mass change during calcination and enables one to judge if the metal particles evaporated. Differential scanning calorimetry (DSC) is another useful technique to evaluate evaporation [2]. Also, one could directly investigate the shape of the metal particles by scanning electron microscopy (SEM) [3]

In the reaction test for each catalyst in this research, the real rate of carbon deposition could not be detected due to technical limitations. Therefore, the amount of carbon deposition had to be neglected for the determination of methane conversion. The value becomes more accurate as the reaction reaches steady state; however, the error is very large in highly non-steady state conditions.

In addition to the amount of carbon deposition, the absolute amount of each component at the outlet of the reactor could not be determined since the mass spectrometer only measures part of the exhaust gas for the analysis. To perform improved analysis, for example, gas chromatography with mass flow dependent detectors in which the actual mass flow of each component can be measured [4] is recommended to be used in place of the mass spectrometry technique.

Another aspect that needs to be improved is the reaction time for each period in the reaction tests. In this research, the reaction time was 20 minutes. As can be seen from the work done by Vohs et al. [5], it takes about half an hour before carbon deposition occurs to significantly deactivate the catalyst. Therefore, the reaction time for each period should be extended to about an hour to determine the resistance against carbon deposition. In addition, to further investigate the stability of a non-deactivating catalyst, each catalyst should be exposed to a lean oxygen environment for about a day.

This investigation was only performed with methane; however, catalytic optimization needs to be done with other hydrocarbons with higher carbon content such as ethane, propane and butane. It would be ideal if the SOFC could operate with readily available hydrocarbon fuels such as gasoline or natural gases so that fuel cells do not have to suffer from insufficient fueling facilities.

References

[1] D. Clément, *Inorganic thermogravimetric analysis*. Translated from the French manuscript by Ralph E. Oesper, 2d and rev. ed, Amsterdam; New York: Elsevier Pub. Co., 1963

[2] V. Majidi, R. G. Smith, N. Xu, M. W. McMahon, R Bossio, *Spectrochimica Acta Part B: Atomic Spectroscopy*, Vol. 55, 2000, 1787

[3] S. Gunther, B. Kaulich, L. Gregoratti, M. Kiskinova, *Progress in Surface Science* Vol. 70, 2002, 187

[4] H. J. A. Philipsen, Journal of Chromatography A, Vol. 1037, 2004, 329

[5] S. Park, R. J. Gorte, J. M. Vohs, *Applied Catalysis A: General*, Vol. 200, 2000, 55

Nomenclature

A	Pre-exponential factor in the Arrhenius equation.
A_{N_2}	Surface area of the N_2 molecule, m^2/molecule
a_i	Activity of component i
C_i	Concentration of component i.
E	Emf at temperature T.
E^o	Emf at standard state
E_a	Activation energy.
$E_{binding}$	Binding energy of the electron.
$E_{kinetics}$	Kinetic energy of the electron.
F	Faraday's constant (F = 96,485 C /mol)
F_{i0}	Inlet molar flow rate of the component i, mol/min
ΔG	Gibbs free energy of the reaction.

ΔH	Enthalpy of reaction.
h	Planck's constant = 6.626068×10^{-34} m^2 kg / s
K	Equilibrium constant determined by equation (3-15)
k	Rate constant. This is determined by the Arrhenius law. $k = \left[A \exp\left(-\frac{E_a}{RT} \right) \right]$
M	The transition metal contained in the catalyst. This is assumed to be the active catalytic site.
P_a	Ambient pressure, mm Hg
P	Absolute pressure of N_2 (estimated by $\%N_2/100$ x P), mm Hg
P_0	Saturation pressure of N_2 (estimated by P_a + 15 mmHg), mm Hg
P_i	Partial pressure of component i
$\overline{P}_i$	Average partial pressure of component i in period C
R	The gas constant, 8.3143 J/mol·K

$(-r_{CH_4})$	The disappearance rate of methane, [mol CH_4/(min mol metal)]
SA	Surface area, m^2/g
SW	Sample weight, g
T	Temperature.
T_h	The temperature from which the system is supplying the heat,
T_l	The temperature to which the system is rejecting the heat.
T_a	Ambient temperature, °C
t_1	The starting time of period C.
t_2	The ending time of period C.
V	Volume.
V_a	Volume sorbed at ambient conditions, mL
V_{STP}	Volume sorbed at STP, mL/g of sample
V_m	Volume of the monolayer, mL
W_r	Reversible work output

X_{H2O}	Conversion of water vapor.
X_{CH4}	Conversion of methane
Y_{CO2}	Selectivity of CO_2 over CO.
Y_A	CO_2 selectivity in period A.
Y_E	CO_2 selectivity in period E.
Z	CO_2 selectivity change

Greek Letters

α	Thermal expansivity, K^{-1}
η_{carnot}	Carnot cycle efficiency
θ_i	Fraction of the vacant sites.
v_i	Stoichiometric coefficients of component i, negative for the reactants and positive for the products
ν	Frequency
ϕ	Work function

Appendix A

The conversion of methane for different temperatures and inlet compositions are listed.

The values were determined by equations (3-6) through (3-9).

The average conversion (methane to CO and CO_2) at Period A								
T (°C)	Ni/8YSZ	Cu/8YSZ	Co/8YSZ	Ag/8YSZ	Ni/CeO_2/8YSZ	Cu/CeO_2/8YSZ	Co/CeO_2/8YSZ	Ag/CeO_2/8YSZ
800	0.89	0.86	0.89	0.86	0.95	0.88	0.88	0.86
700	0.93	0.78	0.84	0.84	0.93	0.86	0.93	0.85
600	0.87	0.73	0.78	0.75	0.70	0.73	0.76	0.72
500	0.36	0.46	0.40	0.42	0.43	0.44	0.39	0.48
The average conversion (methane to CO and CO_2) at Period B								
T (°C)	Ni/8YSZ	Cu/8YSZ	Co/8YSZ	Ag/8YSZ	Ni/CeO_2/8YSZ	Cu/CeO_2/8YSZ	Co/CeO_2/8YSZ	Ag/CeO_2/8YSZ
800	0.91	0.52	0.90	0.54	0.97	0.51	0.93	0.51
700	0.78	0.32	0.54	0.48	0.94	0.54	0.86	0.49
600	0.84	0.39	0.51	0.39	0.36	0.38	0.37	0.39
500	0.23	0.32	0.26	0.27	0.27	0.31	0.26	0.29
The average conversion (methane to CO and CO_2) at Period C								
T (°C)	Ni/8YSZ	Cu/8YSZ	Co/8YSZ	Ag/8YSZ	Ni/CeO_2/8YSZ	Cu/CeO_2/8YSZ	Co/CeO_2/8YSZ	Ag/CeO_2/8YSZ
800	0.85	0.33	0.53	0.36	0.98	0.32	0.81	0.35
700	0.86	0.17	0.46	0.30	0.96	0.35	0.69	0.33
600	0.65	0.21	0.32	0.22	0.46	0.18	0.18	0.21
500	0.17	0.17	0.18	0.16	0.18	0.19	0.17	0.16
The average conversion (methane to CO and CO_2) at Period D								
T (°C)	Ni/8YSZ	Cu/8YSZ	Co/8YSZ	Ag/8YSZ	Ni/CeO_2/8YSZ	Cu/CeO_2/8YSZ	Co/CeO_2/8YSZ	Ag/CeO_2/8YSZ
800	0.85	0.48	0.86	0.51	0.98	0.49	0.98	0.53
700	0.93	0.30	0.73	0.45	0.98	0.51	0.94	0.52
600	0.92	0.30	0.47	0.32	0.80	0.29	0.29	0.31
500	0.23	0.27	0.24	0.23	0.24	0.28	0.25	0.26
The average conversion (methane to CO and CO_2) at Period E								
T (°C)	Ni/8YSZ	Cu/8YSZ	Co/8YSZ	Ag/8YSZ	Ni/CeO_2/8YSZ	Cu/CeO_2/8YSZ	Co/CeO_2/8YSZ	Ag/CeO_2/8YSZ
800	0.86	0.84	0.98	0.85	0.99	0.85	0.99	0.89
700	0.98	0.77	0.94	0.83	0.99	0.86	0.98	0.88
600	0.97	0.69	0.81	0.73	0.94	0.68	0.69	0.70
500	0.41	0.49	0.40	0.40	0.42	0.47	0.40	0.50

Table A-1. The average conversions of methane for all catalysts at all temperatures at all periods.

Period	Catalysts	$C_{CH4,in}$ (mol/m^3)	$C_{O2,in}$ (mol/m^3)	$C_{CH4,out}$ (mol/m^3)	$C_{O2,out}$ (mol/m^3)	Average C_{CH4} (mol/m^3)	Average C_{O2} (mol/m^3)	($-r_{CH4}$) (mol/min gmetal)
A	Ni/8YSZ	**1.70**	**3.41**	**0.18**	**0.51**	**0.94**	**1.96**	**3.67E-02**
B		5.11	2.04	0.44	0.86	2.77	1.45	1.13E-01
C		8.52	0.68	1.37	4.30	4.94	2.49	1.73E-01
A	Cu/8YSZ	**1.70**	**3.41**	**0.24**	**0.30**	0.97	1.85	**3.73E-02**
B		5.11	2.04	2.43	0.32	3.77	1.18	6.85E-02
C		8.52	0.68	5.68	0.39	7.10	0.54	7.26E-02
A	Co/8YSZ	**1.70**	**3.41**	**0.18**	**0.10**	0.94	1.75	**9.64E-02**
B		5.11	2.04	0.52	0.13	2.81	1.09	2.91E-01
C		8.52	0.68	4.03	0.22	6.27	0.45	2.84E-01
A	Ag/8YSZ	**1.70**	**3.41**	**0.25**	**0.22**	0.97	1.81	**5.56E-02**
B		5.11	2.04	2.36	0.42	3.73	1.23	1.05E-01
C		8.52	0.68	5.45	0.53	6.98	0.61	1.17E-01
A	Ni/CeO_2/8YSZ	**1.70**	**3.41**	**0.39**	**1.15**	1.05	2.28	**5.91E-02**
B		5.11	2.04	2.93	13.68	4.02	7.86	1.82E-01
C		8.52	0.68	4.37	30.14	6.45	15.41	3.04E-01
A	Cu/CeO_2/8YSZ	**1.70**	**3.41**	**0.21**	**0.28**	0.96	1.84	**4.31E-02**
B		5.11	2.04	2.49	0.35	3.80	1.20	7.58E-02
C		8.52	0.68	5.75	0.42	7.14	0.55	7.98E-02
A	Co/CeO_2/8YSZ	**1.70**	**3.41**	**0.21**	**0.19**	0.96	1.80	**8.62E-02**
B		5.11	2.04	0.37	0.37	2.74	1.21	2.73E-01
C		8.52	0.68	1.63	1.01	5.07	0.85	3.98E-01
A	Ag/CeO_2/8YSZ	**1.70**	**3.41**	**0.24**	**0.17**	0.97	1.79	**1.28E-01**
B		5.11	2.04	2.53	0.33	3.82	1.19	2.26E-01
C		8.52	0.68	5.53	0.41	7.03	0.55	2.61E-01

Table A-2. The data used for the rate of reaction analysis for **800 °C**. The outlet concentration is approximated by the following equation since the actual partial pressure outside of the mass spectrometer is unknown.

$$C_{CH_4,out} = C_{CH_4,in}\left(1 - X_{CH_4}\right) \tag{A-1}$$

$$C_{O_2,out} = C_{CH_4,out}\left(\frac{P_{O_2,MS}}{P_{CH_4,MS}}\right) \tag{A-2}$$

Period	Catalysts	$C_{CH4,in}$ (mol/m^3)	$C_{O2,in}$ (mol/m^3)	$C_{CH4,out}$ (mol/m^3)	$C_{O2,out}$ (mol/m^3)	Average C_{CH4}	Average C_{O2} (mol/m^3)	$(-r_{CH4})$ (mol/min gmetal)
A	Ni/8YSZ	**1.70**	**3.41**	**0.37**	**0.11**	1.04	1.76	**3.93E-02**
B		5.11	2.04	0.38	0.15	2.75	1.10	9.96E-02
C		8.52	0.68	1.23	0.42	4.87	0.55	1.65E-01
A	Cu/8YSZ	**1.70**	**3.41**	**0.37**	**1.47**	1.03	2.44	**3.82E-02**
B		5.11	2.04	3.46	0.18	4.28	1.11	4.72E-02
C		8.52	0.68	7.07	0.23	7.79	0.45	3.75E-02
A	Co/8YSZ	**1.70**	**3.41**	**0.27**	**0.22**	0.99	1.81	**1.13E-01**
B		5.11	2.04	2.35	0.43	3.73	1.23	2.17E-01
C		8.52	0.68	4.58	0.47	6.55	0.58	2.81E-01
A	Ag/8YSZ	**1.70**	**3.41**	**0.28**	**0.18**	0.99	1.79	**5.84E-02**
B		5.11	2.04	2.65	0.34	3.88	1.19	1.01E-01
C		8.52	0.68	5.95	0.44	7.24	0.56	9.50E-02
A	Ni/CeO_2/8YSZ	**1.70**	**3.41**	**0.12**	**0.17**	0.91	1.79	**6.88E-02**
B		5.11	2.04	0.30	0.37	2.71	1.21	2.10E-01
C		8.52	0.68	0.35	1.43	4.43	1.05	3.23E-01
A	Cu/CeO_2/8YSZ	**1.70**	**3.41**	**0.25**	**0.20**	0.97	1.81	**5.03E-02**
B		5.11	2.04	2.33	0.42	3.72	1.23	9.61E-02
C		8.52	0.68	5.52	0.54	7.02	0.61	9.39E-02
A	Co/CeO_2/8YSZ	**1.70**	**3.41**	**0.12**	**0.16**	0.91	1.78	**8.37E-02**
B		5.11	2.04	0.70	0.30	2.91	1.17	2.32E-01
C		8.52	0.68	2.68	0.85	5.60	0.76	2.79E-01
A	Ag/CeO_2/8YSZ	**1.70**	**3.41**	**0.26**	**0.18**	0.98	1.79	**1.38E-01**
B		5.11	2.04	2.62	0.37	3.86	1.21	2.38E-01
C		8.52	0.68	5.68	0.49	7.10	0.59	2.46E-01

Table A-3. The data used for the rate of reaction analysis for **700 °C**. The outlet concentration is approximated by equations (A-1) and (A-2).

Period	Catalysts	$C_{CH4,in}$ (mol/m^3)	$C_{O2,in}$ (mol/m^3)	$C_{CH4,out}$ (mol/m^3)	$C_{O2,out}$ (mol/m^3)	Average C_{CH4} (mol/m^3)	Average C_{O2} (mol/m^3)	$(-r_{CH4})$ (mol/min gmetal)
A	Ni/8YSZ	**1.70**	**3.41**	**0.23**	**0.20**	0.96	1.80	**4.64E-02**
B		5.11	2.04	0.83	0.27	2.97	1.16	1.34E-01
C		8.52	0.68	2.99	0.54	5.75	0.61	1.41E-01
A	Cu/8YSZ	**1.70**	**3.41**	**0.46**	**0.12**	1.08	1.76	**3.83E-02**
B		5.11	2.04	3.11	0.21	4.11	1.13	6.16E-02
C		8.52	0.68	6.77	0.28	7.64	0.48	4.38E-02
A	Co/8YSZ	**1.70**	**3.41**	**0.38**	**0.29**	1.04	1.85	**1.06E-01**
B		5.11	2.04	2.51	0.40	3.81	1.22	2.07E-01
C		8.52	0.68	5.76	0.48	7.14	0.58	1.79E-01
A	Ag/8YSZ	**1.70**	**3.41**	**0.42**	**0.29**	1.06	1.85	**5.81E-02**
B		5.11	2.04	3.12	0.28	4.12	1.16	9.00E-02
C		8.52	0.68	6.68	0.26	7.60	0.47	6.76E-02
A	Ni/CeO_2/8YSZ	**1.70**	**3.41**	**0.52**	**0.20**	1.11	1.80	**5.44E-02**
B		5.11	2.04	3.26	0.21	4.18	1.13	8.51E-02
C		8.52	0.68	4.63	0.27	6.57	0.48	1.45E-01
A	Cu/CeO_2/8YSZ	**1.70**	**3.41**	**0.46**	**0.29**	1.08	1.85	**4.27E-02**
B		5.11	2.04	3.19	0.20	4.15	1.12	6.61E-02
C		8.52	0.68	6.96	0.24	7.74	0.46	4.37E-02
A	Co/CeO_2/8YSZ	**1.70**	**3.41**	**0.42**	**0.37**	1.06	1.89	**8.55E-02**
B		5.11	2.04	3.22	0.17	4.17	1.11	1.25E-01
C		8.52	0.68	7.02	0.22	7.77	0.45	8.11E-02
A	Ag/CeO_2/8YSZ	**1.70**	**3.41**	**0.48**	**0.12**	1.09	1.77	**1.30E-01**
B		5.11	2.04	3.14	0.22	4.13	1.13	2.09E-01
C		8.52	0.68	6.77	0.28	7.64	0.48	1.51E-01

Table A-4. The data used for the rate of reaction analysis for **600 °C**. The outlet concentration is approximated by equations (A-1) and (A-2).

Period	Catalysts	$C_{CH4,in}$ (mol/m^3)	$C_{O2,in}$ (mol/m^3)	$C_{CH4,out}$ (mol/m^3)	$C_{O2,out}$ (mol/m^3)	Average C_{CH4} (mol/m^3)	Average C_{O2} (mol/m^3)	$(-r_{CH4})$ (mol/min gmetal)
A	Ni/8YSZ	**1.70**	**3.41**	**1.09**	**1.27**	1.40	2.34	**2.08E-02**
B		5.11	2.04	3.94	1.07	4.52	1.56	4.01E-02
C		8.52	0.68	7.08	0.50	7.80	0.59	3.55E-02
A	Cu/8YSZ	**1.70**	**3.41**	**0.93**	**0.91**	1.32	2.16	**2.83E-02**
B		5.11	2.04	3.50	0.50	4.30	1.27	5.88E-02
C		8.52	0.68	7.08	0.20	7.80	0.44	3.77E-02
A	Co/8YSZ	**1.70**	**3.41**	**1.02**	**1.08**	1.36	2.25	**6.29E-02**
B		5.11	2.04	3.78	1.05	4.45	1.55	1.22E-01
C		8.52	0.68	7.00	0.39	7.76	0.54	1.00E-01
A	Ag/8YSZ	**1.70**	**3.41**	**1.00**	**1.05**	1.35	2.23	**3.63E-02**
B		5.11	2.04	3.72	0.71	4.42	1.38	7.13E-02
C		8.52	0.68	7.18	0.25	7.85	0.47	4.97E-02
A	$Ni/CeO_2/8YSZ$	**1.70**	**3.41**	**0.97**	**1.07**	1.34	2.24	**3.81E-02**
B		5.11	2.04	3.72	1.04	4.42	1.54	7.24E-02
C		8.52	0.68	6.95	0.39	7.73	0.54	5.90E-02
A	$Cu/CeO_2/8YSZ$	**1.70**	**3.41**	**0.95**	**0.97**	1.33	2.19	**3.22E-02**
B		5.11	2.04	3.51	0.61	4.31	1.33	6.81E-02
C		8.52	0.68	6.88	0.26	7.70	0.47	5.03E-02
A	$Co/CeO_2/8YSZ$	**1.70**	**3.41**	**1.04**	**1.11**	1.37	2.26	**5.04E-02**
B		5.11	2.04	3.79	0.91	4.45	1.48	9.96E-02
C		8.52	0.68	7.10	0.29	7.81	0.49	7.72E-02
A	$Ag/CeO_2/8YSZ$	**1.70**	**3.41**	**0.89**	**0.86**	1.30	2.13	**1.00E-01**
B		5.11	2.04	3.64	0.57	4.38	1.31	1.81E-01
C		8.52	0.68	7.14	0.23	7.83	0.45	1.22E-01

Table A-5. The data used for the rate of reaction analysis for **500 °C**. The outlet concentration is approximated by equations (A-1) and (A-2).

Appendix B

The equilibrium constant K was calculated for the following 3 different reactions (reactions indicated on the figures). The figures are the plot of $\log_{10}K$ versus temperature in degrees centigrade.

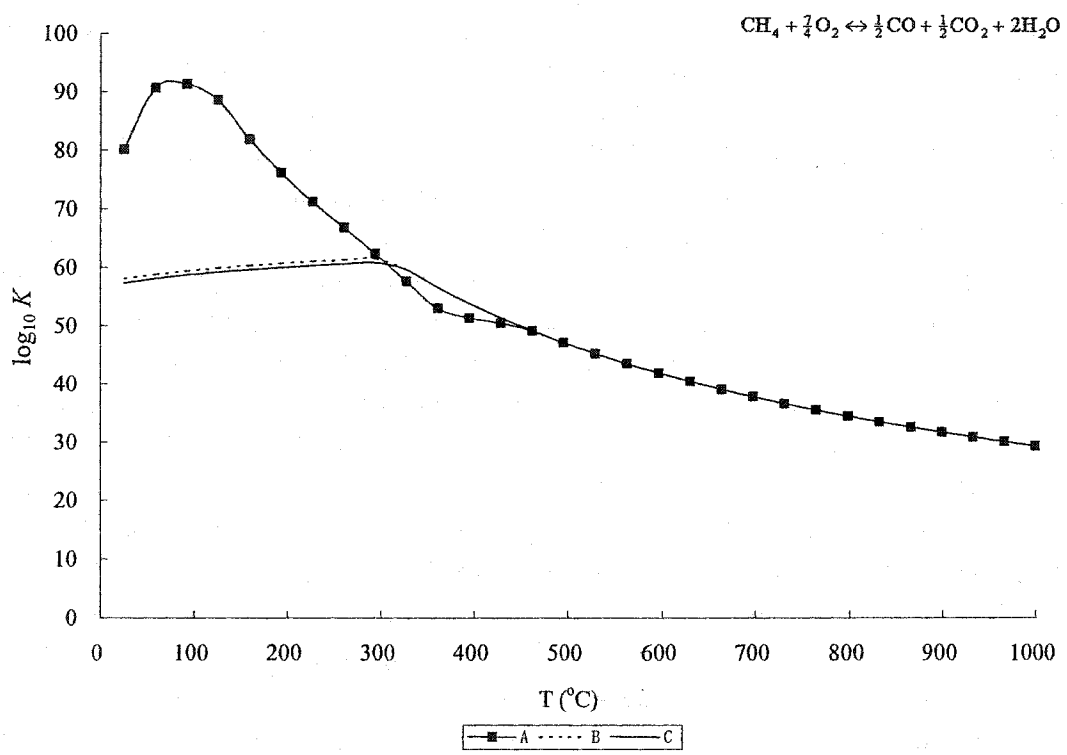

Figure B-1. The logarithm of equilibrium constant K vs. temperature for reaction (3-13).

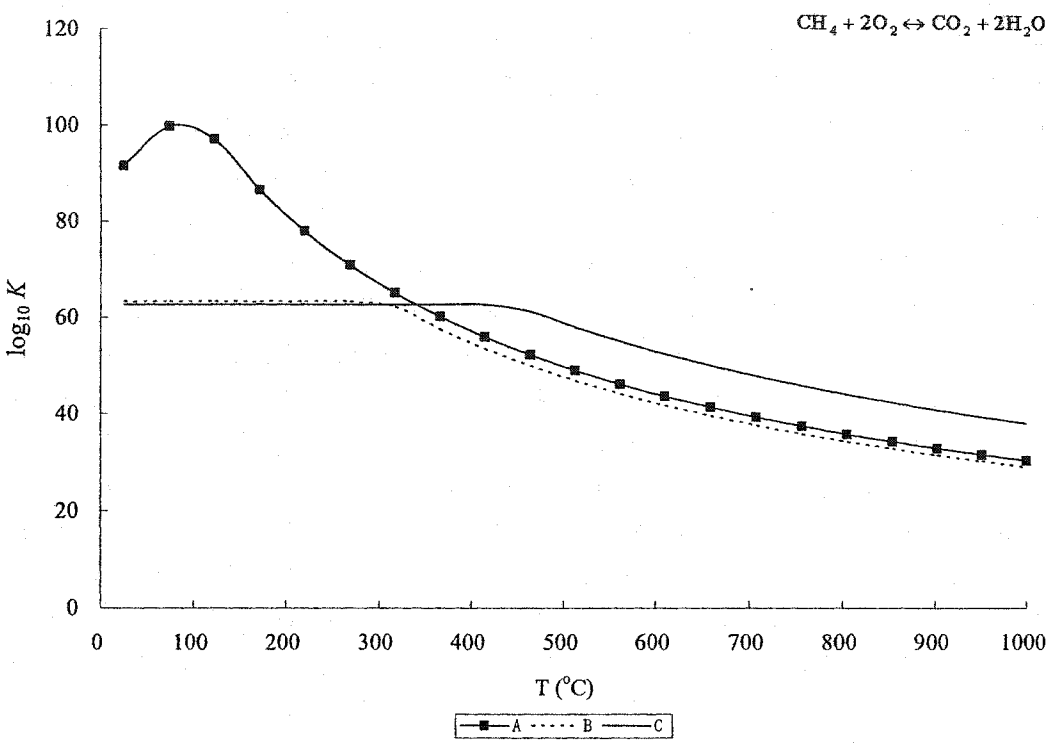

Figure B-2. The logarithm of equilibrium constant K vs. temperature for reaction (3-13).

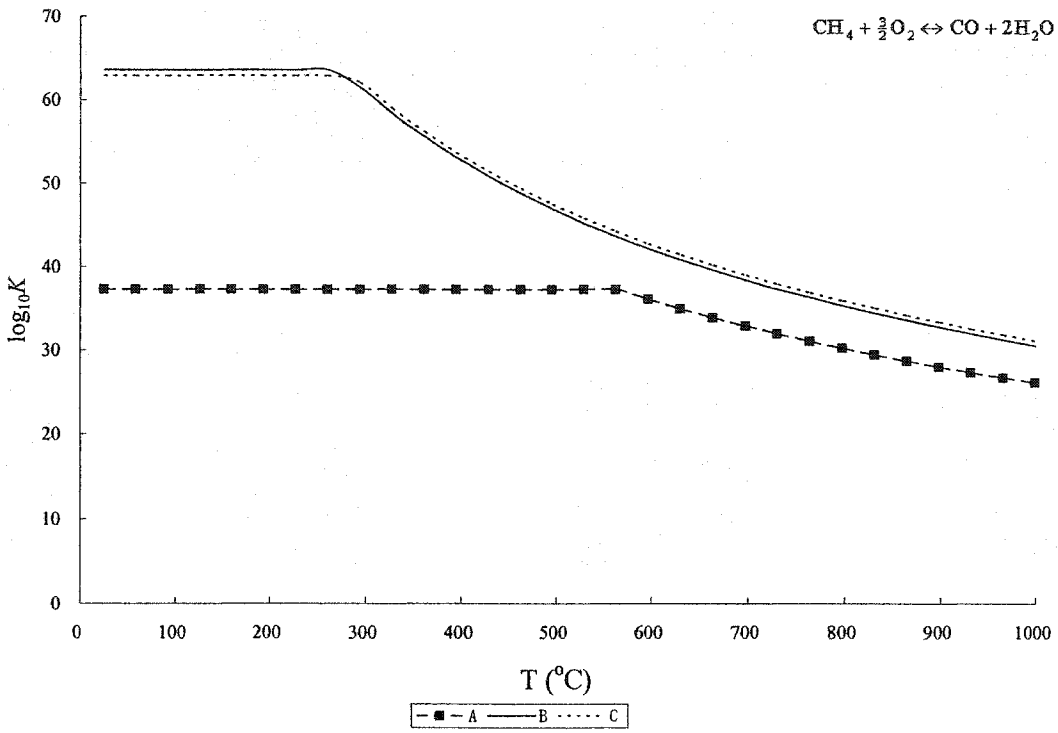

Figure B-3. The logarithm of equilibrium constant K vs. temperature for reaction (3-14).

Figures B-1 through B-8 represent the comparison of the calculated model and the experimental data for the methane disappearance rate. The data points 1 through 12 on the abscissa are listed in Table B-1.

Data points	Period	Temperature (°C)
1	A	800
2	B	800
3	C	800
4	A	700
5	B	700
6	C	700
7	A	600
8	B	600
9	C	600
10	A	500
11	B	500
12	C	500

Table B-1. Data points for Figures B-4 through B-11.

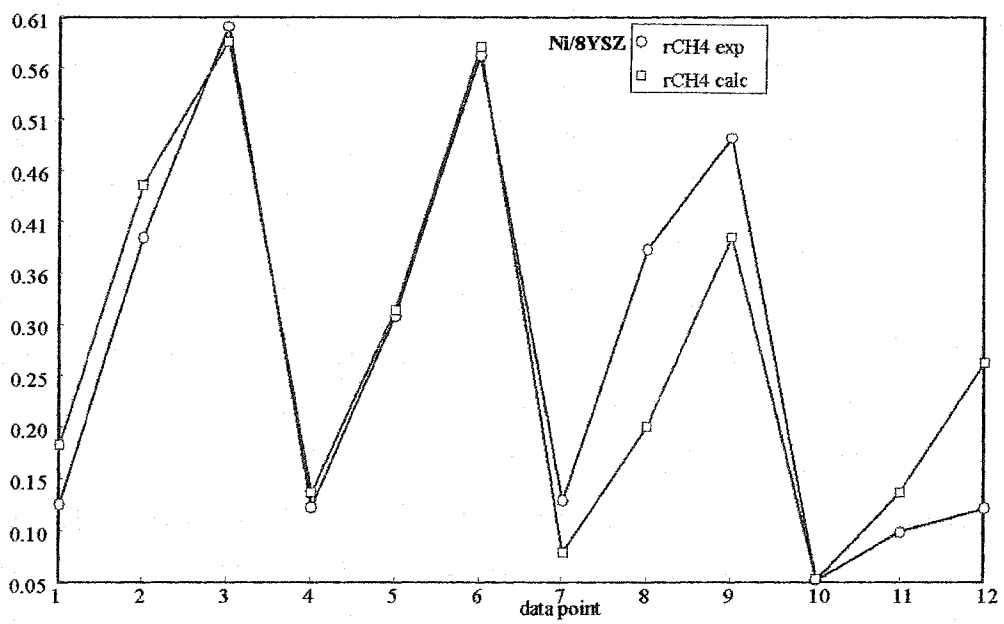

Figure B-4. The disappearance rate of methane plot for Ni/8YSZ. The vertical axis represents the disappearance rate of methane in "$\text{mol CH}_4/(\text{min} \cdot \text{mol metal})$". Refer to Table B-1 for the data points for the abscissa axis.

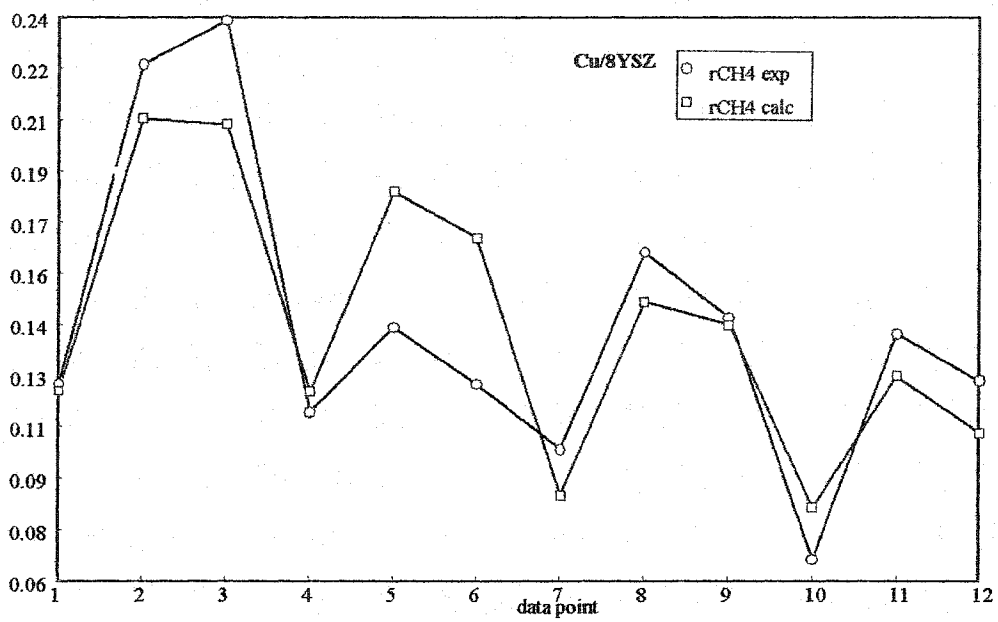

Figure B-5. The disappearance rate of methane plot for Cu/8YSZ. See Figure B-4 for the explanation of the axes.

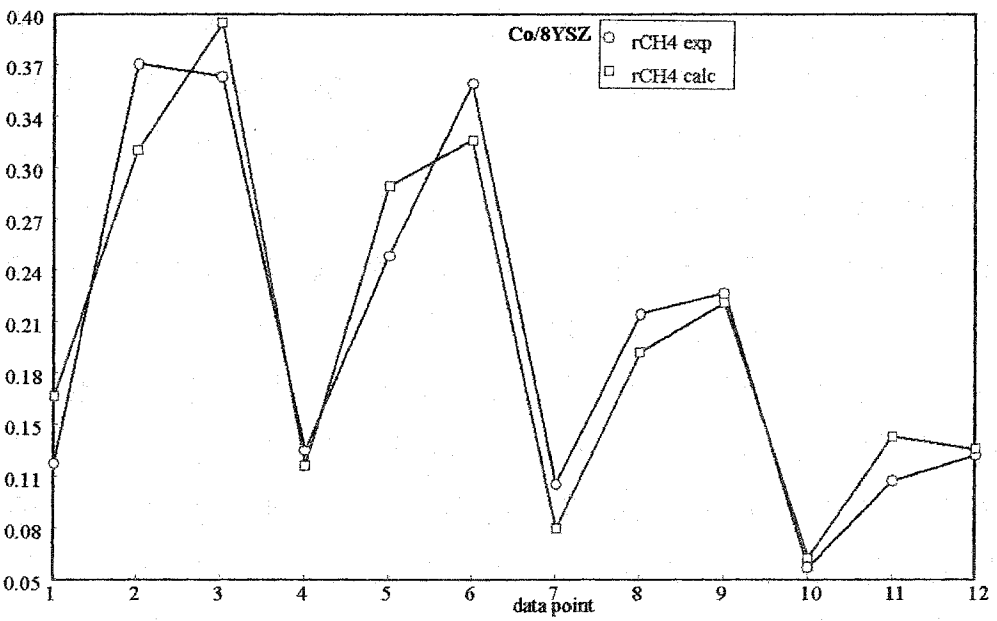

Figure B-6. The disappearance rate of methane plot for Co/8YSZ. See Figure B-4 for the explanation of the axes.

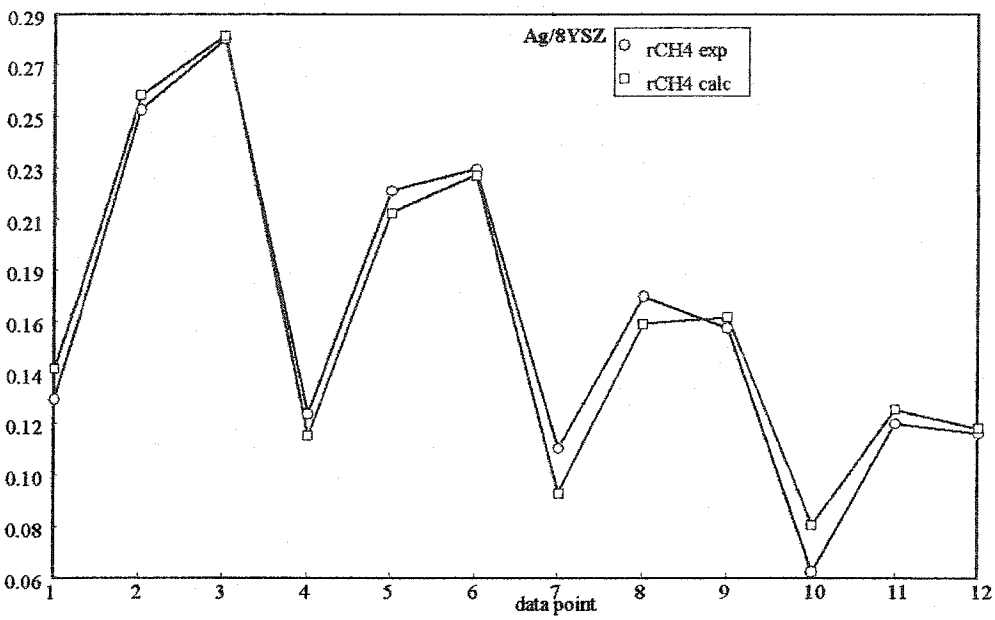

Figure B-7. The disappearance rate of methane plot for Ag/8YSZ. See Figure B-4 for the explanation of the axes.

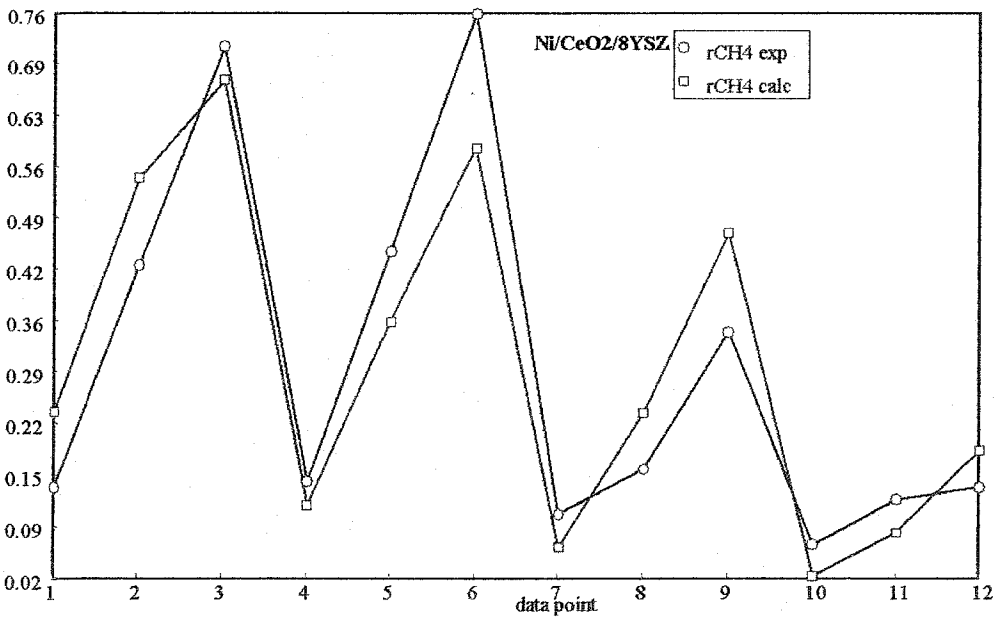

Figure B-8. The disappearance rate of methane plot for $Ni/CeO_2/8YSZ$. See Figure B-4 for the explanation of the axes.

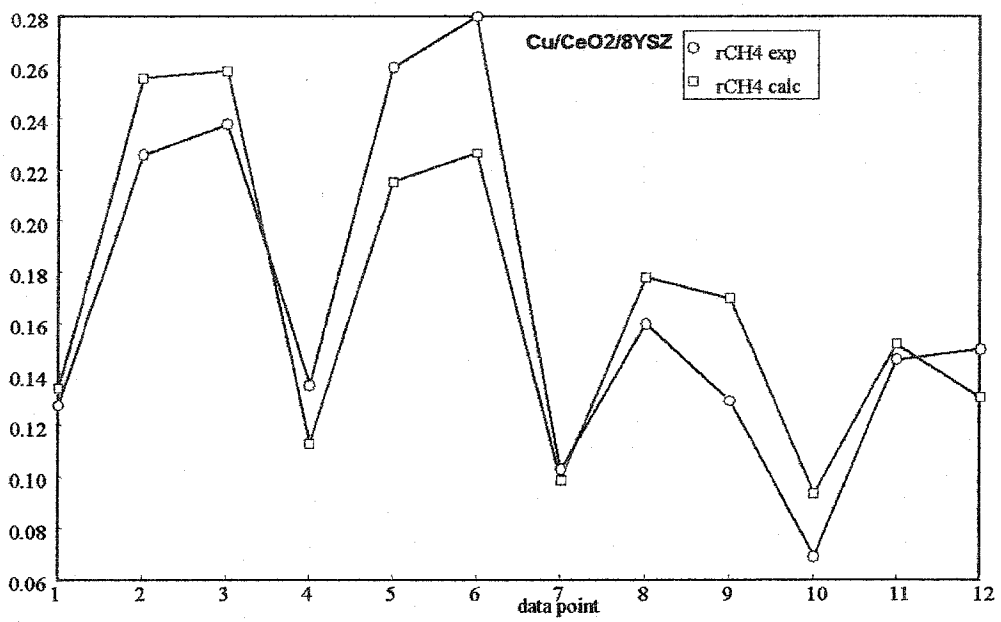

Figure B-9. The disappearance rate of methane plot for $Cu/CeO_2/8YSZ$. See Figure B-4 for the explanation of the axes.

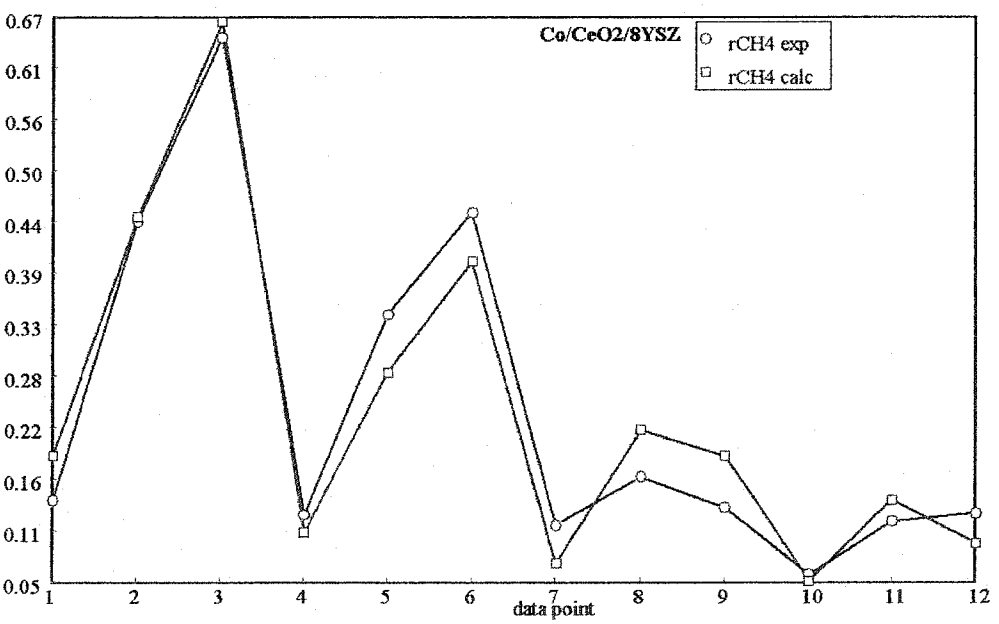

Figure B-10. The disappearance rate of methane plot for $Co/CeO_2/8YSZ$. See Figure B-4 for the explanation of the axes.

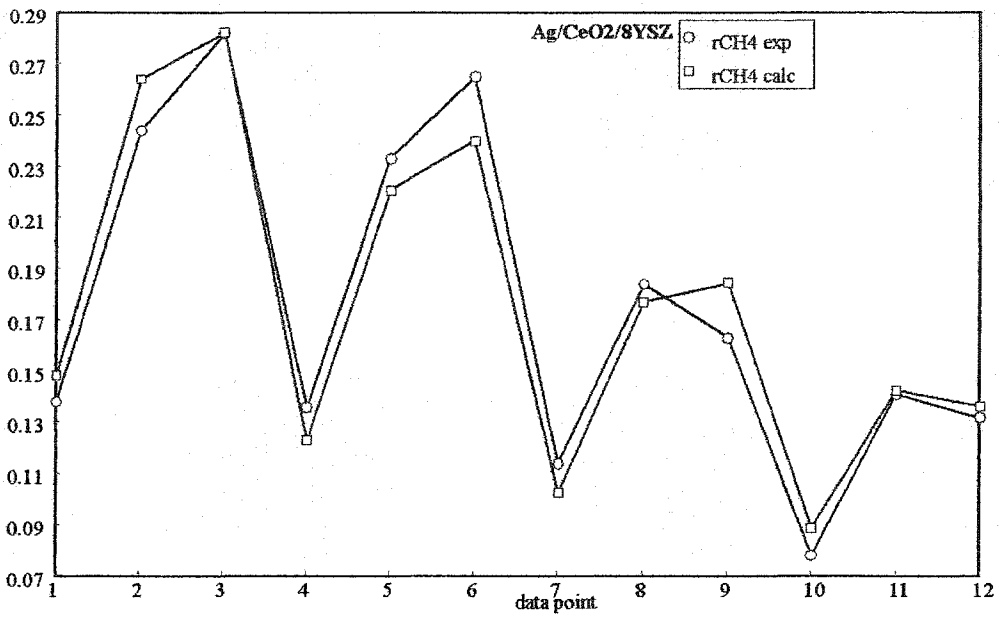

Figure B-11. The disappearance rate of methane plot for $Ag/CeO_2/8YSZ$. See Figure B-4 for the explanation of the axes.

Appendix C

The following reactions represented by (C-1) through (C-8) are expected in this experiment. Equations (C-9) through (C-16) represent the rate of reaction expression derived from the Langmuir model of adsorption.

$$CH_4 + M + 4R \underset{k_1'}{\overset{k_1}{\rightleftharpoons}} C-M + 4H-R \qquad \text{(C-1)}$$

$$O_2 + 2M \underset{k_2}{\overset{k_2}{\rightleftharpoons}} 2O-M \qquad \text{(C-2)}$$

$$C-M + O-M \underset{k_3'}{\overset{k_3}{\rightleftharpoons}} CO-M + M \qquad \text{(C-3)}$$

$$CO-M \underset{k_4}{\overset{k_4}{\rightleftharpoons}} CO + M \qquad \text{(C-4)}$$

$$CO-M + O-M \underset{k_5'}{\overset{k_5}{\rightleftharpoons}} CO_2-M + M \qquad \text{(C-5)}$$

$$CO_2-M \underset{k_6'}{\overset{k_6}{\rightleftharpoons}} CO_2 + M \qquad \text{(C-6)}$$

$$2H-M + O-M \underset{k_7'}{\overset{k_7}{\rightleftharpoons}} H_2O + 3M \qquad \text{(C-7)}$$

$$nC-M \underset{k_8'}{\overset{k_8}{\rightleftharpoons}} \underset{\mathrm{M}}{\{C\}_n} \qquad \text{(C-8)}$$

$$2CO-M + \underset{\mathrm{M}}{\{C\}_n} \underset{k_9'}{\overset{k_9}{\rightleftharpoons}} \underset{\mathrm{M}}{\{C\}_{n+2}} + O_2 \qquad \text{(C-9)}$$

$$(r_{ads})_{CH_4} = k_1 C_{CH_4} \theta_V^5 - k_1' \theta_C \theta_H^4 \quad \text{(C-10)}$$

$$(r_{ads})_{O_2} = k_2 C_{O_2} \theta_V^2 - k_2' \theta_O^2 \quad \text{(C-11)}$$

$$r_{s1} = k_3 \theta_C \theta_O - k_3' \theta_{CO} \theta_V^2 \quad \text{(C-12)}$$

$$(r_{dsp})_{CO} = k_4 \theta_{CO} - k_{4,a} C_{CO} \theta_V \quad \text{(C-13)}$$

$$r_{s2} = k_5 \theta_{CO} \theta_O - k_5' \theta_{CO_2} \theta_V \quad \text{(C-14)}$$

$$(r_{dsp})_{CO_2} = k_{6,d} \theta_{CO_2} - k_{6,a} C_{CO_2} \theta_V \quad \text{(C-15)}$$

$$r_{s3} = k_7 \theta_H^2 \theta_O - k_7' C_{H_2O} \theta_V^3 \quad \text{(C-16)}$$

$$r_{s4} = k_8 \theta_C^n - k_8' \theta_{C\text{-}M}^n \quad \text{(C-17)}$$

$$r_{s5} = k_9 \theta_{CO}^2 \theta_C^n - k_9' \theta_C^{n+2} C_{O_2} \quad \text{(C-18)}$$